Development of a Micro Gas Turbine for Central Receiver Concentrating Solar Power Systems

by
Brian Ssebabi

Dissertation presented for the degree of Doctor of Philosophy in the Faculty of Engineering at Stellenbosch University

Supervisor: Prof. Johan van der Spuy
Co-supervisor: Prof. Frank Dinter

March 2020

Declaration

By submitting this dissertation electronically, I declare that the entirety of the work contained therein is my own, original work, that I am the sole author thereof (save to the extent explicitly otherwise stated), that reproduction and publication thereof by Stellenbosch University will not infringe any third party rights and that I have not previously in its entirety or in part submitted it for obtaining any qualification.

Date: March 2020

Abstract

Development of a Micro Gas Turbine for Central Receiver Concentrating Solar Power Systems

B. Ssebabi

Department of Mechanical and Mechatronic Engineering,
University of Stellenbosch,
Private Bag X1, Matieland 7602, South Africa.

Dissertation: PhD (Eng)

March 2020

There is limited access to electricity in much of Southern Africa, yet this region receives some of the highest solar irradiation worldwide. Consequently, there is a huge potential for the deployment of concentrating solar power (CSP) distributed electricity generation systems. The application of gas turbines in central receiver CSP systems combines high concentration ratios of central receiver technology and the ability to scale in size, with inherent gas turbine advantages. This makes these systems ideal for distributed electricity generation applications. However, there are currently no commercial solar-hybrid gas turbine systems readily available off-the-shelf. Through both a theoretical and experimental approach, this study therefore aims to develop a micro gas turbine (MGT) system for central receiver CSP distributed electricity generation applications. The theoretical work involved modeling the performance of a MGT system under solar-hybrid operation, in order to predict the possible operating range and develop suitable operation and control strategies for the MGT system. The experimental work involved designing, building, testing and characterising the performance of an experimental MGT system and then using the obtained test data to validate the predicted performance, as well as assess the technical feasibility of adapting such a system to solar-hybrid operation. The component matching showed a shift of the equilibrium running point on the compressor characteristic, to counter the additional system pressure losses and ensure a useful work output, albeit with a reduced surge margin. Solar-hybrid operation was only possible for a solar share of at least 20 %, while the work output and cycle thermal efficiency drop below standard operation levels beyond certain solar share. In contrast to standard operation,

a higher nominal work output of 20 kW, at a lower specific fuel consumption of 0.0004 kg/kWh and a higher cycle thermal efficiency of 8 % was predicted, the latter potentially increasing to 20 % with recuperation. Based on the proposed control strategy of operating the MGT system at the determined solar-hybrid equilibrium running point, sudden changes in solar irradiation were corrected by altering the fuel flow. From the validation of the predicted performance, the predicted MGT system equilibrium running point matched the optimum experimental equilibrium running points, and a similar shift on the compressor characteristic was predicted for varying levels of system pressure losses. The use of turbocharger technology should allow for easy coupling of the individual MGT system components, some of which could be specially designed for solar-hybrid operation. The twin-shaft configuration allows for flexibility in operation, with the added advantage of ease of starting. The large swallowing capacity of the much bigger power turbine should further ensure that the MGT system is insensitive to load variation. The findings from this study should guide operation and control strategies for the proposed, and future solar-hybrid MGT systems, which should in turn contribute to their development and commercialization.

Uittreksel

Ontwikkeling van 'n Mikrogasturbine vir Sentrale Ontvanger Gekonsentreerde Sonkragstelsels

("Development of a Micro Gas Turbine for Central Receiver Concentrating Solar Power Systems")

B. Ssebabi

Departement Meganiese en Megatroniese Ingenieurswese,
Universiteit van Stellenbosch,
Privaatsak X1, Matieland 7602, Suid Afrika.

Proefskrif: PhD (Ing)

Maart 2020

Alhoewel Suider Afrika van die hoogste sonbestralingsvlakke ter wêreld het, is daar beperkte toegang tot elektrisiteit in die streek. Gevolglik is daar 'n beduidende potensiaal vir die ontplooiing van gekonsentreerde sonkrag (CSP) verspreide elektrisiteitsopwekking stelsels. Die gebruik van gasturbines in sentrale ontvanger CSP stelsels kombineer die hoë konsentrasievlakke van sentrale ontvanger tegnologie en die vermoë om te skaleer, met die inherente voordele van gasturbines. Dit maak hierdie stelsels ideaal vir verspreide elektrisiteitsopwekking toepassings. Daar is egter tans geen kommersiële van-die-rak son-hibriede gasturbine stelsels beskikbaar nie. Die studie poog om deur middel van beide 'n teoretiese en eksperimentele benadering 'n mikrogasturbine (MGT) stelsel vir sentrale ontvanger CSP verspreide elektrisiteitsopwekkings toepassings te ontwikkel. Die teoretiese werk het die modellering van 'n MGT stelsel onder son-hibriede werking behels, ten einde die moontlike bedryfsgebied te voorspel en om gepaste bedryfs- en beheer strategieë vir die MGT te ontwikkel. Die eksperimentele werk het die ontwerp, bou, toets en karakterisering van 'n eksperimentele MGT stelsel behels. Die toetsdata is gebruik om die voorspelde werksverrigting van die stelsel te valideer, sowel as om die tegniese haalbaarheid van die aanpassing van so 'n stelsel vir son-hibriede werking te bepaal. Die stelselbalansering vir son-hibriede toepassing het gewys dat die ekwilibrium werkspunt op die kompressor karakteristiek skuif, ten einde die addisionele stelsel verliese teen te werk, asook om steeds 'n bruikbare drywingsuitset te verseker, alhoewel teen 'n vermindering in staakwydte. Son-hibriede

werking was net moontlik vir 'n sonaandeel van ten minste 20 %, terwyl die werksuitset en siklus termiese benuttingsgraad geval het tot onder standaard bedryfsvlakke bokant 'n sekere sonaandeel. In vergelyking met standaard werking van die MGT, is 'n hoër nominale drywingsuitset van 20 kW, teen 'n laer spesifieke brandstofverbruik van 0.0004 kg/kWh en 'n hoër termiese benuttingsgraad van 8 % voorspel. Laasgenoemde kan potensieel tot 20 % verhoog word met tussenverhitting (recuperation). Gebaseer op die voorgestelde beheer strategie om die MGT stelsel by die spesifieke son-hibriede ekwilibrium werkspunt te bedryf, is daar vir skielike verandering in die sonbestraling gekorrigeer deur die brandstofvloei aan te pas. Uit die validasie van die voorspelde werksverrigting is gevind dat die voorspelde MGT werkspunt ooreenstem met die eksperimentele optimum eksperimentele ekwilibrium werkspunt en dat 'n soortgelyke skuif in die kompressor karakteristiek voorspel is vir wisselende vlakke van stelsel drukverlies. Die gebruik van bestaande turbo-aanjaer tegnologie behoort voorsiening te maak vir die vereenvoudigde koppeling van die MGT stelsel komponente, waarvan sommige doelontwerp kan word vir son-hibriede werking. Die dubbel-as konfigurasie lei tot buigbare stelselwerking, asook die bykomende voordeel dat die stelsel maklik in werking gestel kan word. Die groot vloeikapasiteit van die veel groter drywingsturbine behoort ook te verseker dat die MGT stelsel onsensitief is vir lasvariasies. Die bevindinge van hierdie studie sal as gids dien vir die opstel van bedryfs- en beheer strategieë vir die voorgestelde en toekomstige son-hibriede MGT stelsels, wat weer 'n bydrae sal maak tot die ontwikkeling en kommersialisering van hierdie stelsels.

Acknowledgements

First and foremost, I give thanks and praise to the Almighty God. He has blessed me beyond measure!

It has been a long and tough journey, and several people and organisations have contributed immensely along the way. My sincere gratitude goes to my supervisors, Prof. Johan van der Spuy and Prof. Frank Dinter, for their guidance, encouragement, generosity and unwavering support throughout this project. They always kept the faith, and were fully committed to the completion of the project. Prof. van der Spuy was always available to provide guidance and support, beyond our weekly meetings, and also ensured that we had the necessary funding to accomplish the building of the MGT system test bench. Despite being several miles away during the latter stages of the project, Prof. Dinter always kept abreast with the progress of the project, and was always unequivocal in his support for my continuous registration.

I would also like to thank Dr Paul Gauché, without whom this project would never have seen the light of day. In the same breath, I would like to thank the Solar Thermal Energy Research Group (STERG), for covering the project equipment costs, and the Centre for Renewable and Sustainable Energy Studies (CRSES), for providing a support bursary for my studies.

My sincere appreciation also goes to Mr Robert Dobson. He took a chance on me for my masters, and then continued to generously support and encourage me throughout my PhD. I am forever grateful!

I also wish to thank Dr Markus Schatz and Prof. Damian Vogt from the University of Stuttgart, Germany, for making my 6 month research visit to the Institute of Thermal Turbomachinery and Machinery Laboratory (ITSM) possible, and for supporting me throughout the duration of my visit and thereafter. Through this opportunity, I gained invaluable experience in the designing and testing of combustion chambers for turbocharger based MGT systems.

Many thanks go to the whole workshop team of the Department of Mechanical and Mechatronic Engineering, especially Mr Cobus Zietsman, Mr Ferdi Zietsman, Mrs Maurisha Galant, Mr Anton van den Berg, Mr Julian Stanfliet, Mr Cobus Samuels, Mr Graham Hamerse, Mr Calvin Hamerse, Mr Nathi Hlwempu and Mr Paul-John Robyn, who in one way or another contributed to the successful building and operation of the MGT system test bench. I am also grateful to Ms Sabrina Rudolph, Mr Lourens Ferreira, Mr Abiola Kehinde, Mr

Andani Siavhe and Mr Muaz Jan, for sacrificing their time, and kindly offering to sit in during the MGT system test runs.

Special thanks also go to all my office colleagues, both past and present, for generally providing a good working environment. To my good friend Dr Ngoy Mutonkole, thank you for paving the way, and for always being an inspiration.

I am forever indebted to my family, especially my late aunt Flo and her late husband uncle Isaac, for taking me into their home and loving me unconditionally. I am also forever grateful to my uncle David, for supporting my dream to come to South Africa, to pursue my postgraduate studies.

Last but certainly not least, my sincere love and appreciation goes to Melanie, and the whole Morris family. Thank you for accepting and loving me, and for being my family away from home!

Dedications

To everyone who has loved and supported me!

Contents

List of Figures

List of Tables

Nomenclature

Constants

g = $9.81\,\mathrm{m/s^2}$

Variables

A	Area [$\mathrm{m^2}$]
b	Bias uncertainty [%]
C	Coefficient of discharge [-]
$\overline{C}_f$	Carbon content of propane by mass [kgC/kgC_3H_4]
c_p	Ideal-gas specific heat at constant pressure [J/kgK] or [J/kmolK]
D, d	Diameter [mm]
d_s	Specific diameter [-]
$E.C.V_T$	Effective calorific value at a specified temperature [J/kg]
EOT	Equation of time [minutes]
f	Fuel/air ratio [-]
H	Head [m], lower heating value [J/kg]
$\overline{H}_f$	Hydrogen content of propane by mass [kgH/kgC_3H_4]
$\overline{h}$	Enthalpy [J/kg] or [J/kmol]
$\overline{h}^0$	Sensible enthalpy of a reactant or product at the standard reference state (25 °C and 1 atm) [J/kg]
$\overline{h}_f^0$	Enthalpy of formation of a reactant or product at the standard reference state (25 °C and 1 atm) [J/kg]
L	Length [mm], Longitude [°]
LC	Longitude correction [hours]
LCT	Local clock time [hours]
K	Concordance factor [-]
$\dot{m}$	Mass flow rate [kg/s]
M	Molar mass [kg/kmol]
N	Rotational speed [rpm], day number, number of sample measurements

n_s	Specific speed [-]
n_v	Number of swirler vanes
P	Pressure [Pa] or [bar]
p	Precision uncertainty [%]
$\dot{Q}$	Thermal energy transfer rate [W]
R	Molar gas constant [J/kgK]
r	Pressure ratio [-]
SFC	Specific fuel consumption [kg/kWh]
s	Entropy J/kgK, standard deviation
T	Temperature [°C] or [K]
t_s	Solar time [hours]
t_v	Swirler vane blade thickness [mm]
U, u	Uncertainty [%]
V	Velocity [m/s]
$\dot{V}$	Volume flow rate [m^3/s]
$\dot{W}$	Work transfer rate [W]
$\dot{x}$	Molar mass flow rate of propane [kmol/s]
$\dot{y}$	Molar mass flow rate of air [kmol/s]

Greek letters

α	Solar altitude angle [radians]
β	Diameter ratio, swirler vane angle [°]
γ	Specific heat ratio [-]
Δ	Change in
δ	Declination angle [radians]
ε	Effectiveness [%]
ϵ	Expansion factor [-]
η	Efficiency [%]
θ	Dome angle [°], sensitivity coefficient [-]
θ_C	Carbon theta function [-]
θ_H	Hydrogen theta function [-]
θ_z	Solar zenith angle [radians]
μ	Dynamic viscosity [kg/ms]
ρ	Density [kg/m^3]
ϕ	Equivalence ratio [-], latitude angle [radians]
ψ	Divergence angle [°]

ω	Hour angle [radians]

Subscripts

0	Stagnation condition, reference value
1	Gas-generator compressor inlet
2	Gas-generator compressor outlet
3	Gas-generator turbine inlet
4	Gas-generator turbine outlet/power turbine inlet
5	Power turbine outlet
6	Solar receiver outlet
7	Low-pressure compressor inlet
8	Low-pressure compressor outlet
a	Air
ad	Adiabatic
amb	Ambient
an	Annulus
bm	Bellmouth
C_3H_8	Propane
CO_2	Carbon dioxide
c	Compressor
$corr$	Corrected
dif	Diffuser
f	Fuel
$field$	Heliostat field
ft	Flame tube
g	Gases
H_2O	Water vapor
h	Hole
id	Ideal
loc	Location
max	Maximum
$meas$	Measured
$mech$	Mechanical
N_2	Nitrogen
O_2	Oxygen
opt	Optical
p	Product

pt	Power turbine
pz	Primary zone
R	Recuperated, calculated parameter
r	Reactant
ref	Reference
rz	Recirculation zone
s	Isentropic, snout
sol	Solar
st	Standard time
sw	Swirler
sz	Secondary zone
T	Specified state
TC	Turbocharger
t	Turbine
th	Thermal
$t-t$	Total-to-total
X	Measured parameter

Dimensionless numbers

Re	Reynolds number [-]

Abbreviations

AI/O	Analog input/output
ASME	American Society of Mechanical Engineers
abs	Absolute
CAD	Computer aided design
CFD	Computational fluid dynamics
CSP	Concentrating solar power
DAQ	Data acquisition
DNI	Direct normal irradiation
diff	Differential
E+H	Endress+Hauser
GUI	Graphical user interface
HTF	Heat transfer fluid
ID	Inner diameter
I/O	Input/output
ISO	International Organization for Standardization

LHV Lower heating value
LPG Liquefied petroleum gas
MGT Micro gas turbine
MTT Micro Turbine Technology
OEM Original equipment manufacturer
OD Outer diameter
SHMGT Solar-hybrid micro gas turbine
STERG Solar Thermal Energy Research Group
SUNSPOT Stellenbosch UNiversity Solar POwer Thermodynamic
TIT Turbine inlet temperature
VI Virtual instrument

Chapter 1

Introduction

1.1 Background

Southern Africa is blessed with one of the best solar energy resources worldwide (IEA, 2010); with many parts of the region receiving long term averaged annual direct normal irradiation (DNI) in excess of 2000 kWh/m^2 (see Figure 1.1). However, much of Southern Africa has limited access to electricity, especially dispersed and sparsely populated communities in remote rural areas (Merven *et al.*, 2010; SADC, 2010). There is a strong dependence on biomass resources – mainly in the form of wood fuel – for cooking and heating purposes and small diesel generator sets for electricity generation (IRENA, 2013*a*,*b*; SADC, 2010).

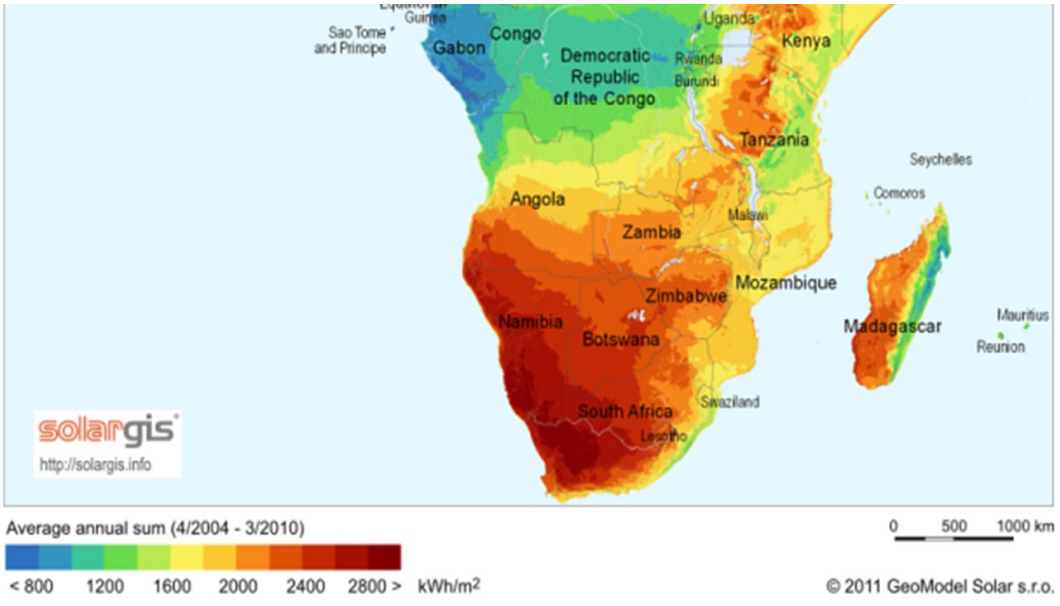

Figure 1.1: Southern Africa long term averaged annual DNI (adapted from GeoModel Solar, 2017)

The excellent solar resource, coupled with the need to increase access to electricity, makes the deployment of concentrating solar power (CSP) distributed electricity generation systems in Southern Africa an attractive proposition (Gauché *et al.*, 2014). CSP power generation technology, such as the central receiver system, uses tracking solar collectors (mirrors) to concentrate solar irradiation onto a single focal point. The solar irradiation heats a heat transfer fluid (HTF), such as molten salt, which in today's state-of-the-art CSP plants is stored in tanks and used to generate steam. Similar to conventional power plants, the steam drives a turbine-generator set, which in turn generates electricity.

The ability to scale in size makes central receiver CSP generation systems suitable for distributed electricity generation in remote rural areas (Grobbelaar *et al.*, 2014). In addition, central receiver systems offer the highest degree of localisation and cost reduction potential, given accelerated deployment (Gauché *et al.*, 2014; IRENA, 2013*a*, 2012; Kolb *et al.*, 2011).

The variable nature of the solar resource necessitates the implementation of either hybridisation or thermal energy storage, to ensure power production whenever demand occurs. Hybridisation can be achieved through either combusting backup fuel or combining CSP plants with conventional power plants. The backup fuel can include either renewable resources, such as biofuels and biogas or fossil resources, such as natural gas and diesel. Adopting the solar-hybrid concept offers a viable option for both a reduction in the over reliance on fossil fuel energy resources and an avenue for the exploitation of the available renewable solar energy resource.

Kröger (2012) proposed the Stellenbosch University Solar POwer Thermodynamic (SUNSPOT) combined cycle plant concept (see Figure 1.2) – with a topping solar-hybrid Brayton cycle and a bottoming steam Rankine cycle – as an appropriate and efficient cycle for utility-scale electricity generation in excellent solar resource regions of Southern Africa. The SUNSPOT cycle is a key focus technology of the Solar Thermal Energy Research Group (STERG), in the Department of Mechanical and Mechatronic Engineering at Stellenbosch University. The main target of the research group is to develop technology that contributes towards the commercialisation of this cycle.

Research previously conducted on this cycle focused on the design, test and validation of novel receiver concepts (Heller, 2017; Lubkoll, 2017), thermal energy storage (Allen, 2014; Kotze, 2014), heliostat module development and validation (Landman, 2017), system thermal and thermodynamic modeling and performance evaluation and enhancement of hybrid (wet/dry) cooling systems (Louw, 2015; Owen, 2013). A few studies have also been conducted on the *solarization* of an in-house Rover 1S/60 micro gas turbine (MGT) system (Rover Gas Turbines Limited, 1967), with the focus on, firstly, converting the MGT system from liquid to gaseous fuel operation (Marsh, 2019; Zhang, 2016), with the aim of switching to biogas operation in the future, and then, investigating the potential for improving the performance of the MGT system,

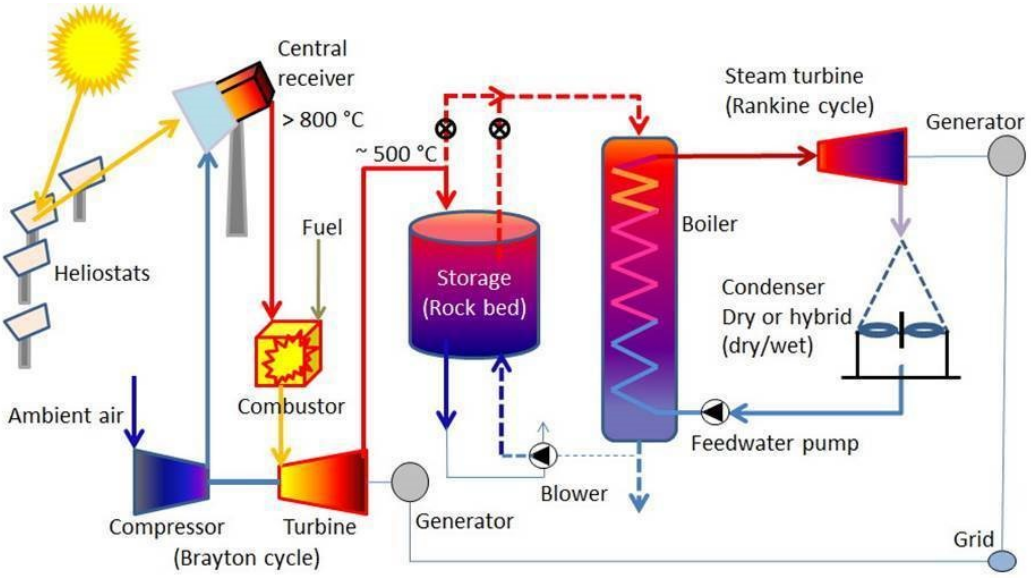

Figure 1.2: The SUNSPOT cycle (Kröger, 2012)

through redesigning system components (Schommarz, 2019; Luiten, 2015).

1.2 Research objective

The aim of this study is to develop a MGT system for central receiver CSP distributed electricity generation applications in Southern Africa.

The research objective will be achieved through:

- Theoretically modeling the performance of a MGT system under solar-hybrid operation, in order to predict the possible operating range, and develop suitable operation and control strategies for the MGT system.
- Designing, building, testing and characterising the performance of the MGT system, in order to validate its predicted performance.
- Assessing the technical feasibility of adapting such a system to solar-hybrid operation.

1.3 Significance of the project

Currently, there are no commercial solar-hybrid gas turbine systems readily available off-the-shelf. Several operational and control challenges still exist and significant development effort is still required to provide technically proven units. Gas turbine manufacturers are reluctant to develop these systems, given the significant effort and time required, and the high costs involved.

Through both a theoretical and experimental approach, this study will develop a MGT system based on two commercially available turbocharger units and a combustion chamber designed for turbocharger based MGT systems. The use of turbocharger technology allows for easy coupling of the individual MGT system components, which should ensure low turbomachinery cost and a simple and modular design. The simple and modular design should allow for easy scaling in size, which should make the MGT system suitable for solar-hybrid distributed electricity generation applications in Southern Africa.

1.4 Dissertation layout

This study mainly consisted of two parts; the theoretical modeling work and the design and experimental work. The dissertation is structured accordingly.

The available literature on the demonstrated solar-hybrid gas turbine systems is discussed in Chapter 2. In addition, a case study of a MGT system successfully developed from off-the-shelf turbocharger components is given.

The theoretical modeling work is covered in Chapter 3. The modeling approach taken is discussed, including how the solar resource was modeled, and how the matching of the individual MGT system components was performed, using individual MGT system component models and performance characteristics found in literature. Discussions of how the fuel mass flow rate required for solar-hybrid operation was determined, and how the variation in the working fluid properties throughout the cycle was modeled are also given. In addition, the potential for improving the cycle thermal efficiency through adding recuperation, and the approach taken in modeling the transient response of the MGT system to sudden changes in solar irradiation are covered. The chapter concludes with a summary of the findings from the modeling work.

The project design and experimental work is discussed in Chapter 4. The set up of the experimental MGT system test bench is described, including the specifications of the instrumentation used on the test bench. The project design work included the design and manufacture of a tubular type combustion chamber. The design process for the combustion chamber, and the obtained design parameters are also presented. The experimental procedure followed, the measured parameters, and the performance parameters calculated from these measurements, as well as the uncertainty associated with both the measured and the calculated parameters are all discussed. The performance of the experimental MGT system is presented, in addition to the validation of the predicted performance. The chapter concludes with a discussion on the technical feasibility of adapting the developed experimental MGT system to solar-hybrid operation.

The key findings from both the theoretical and the experimental work are summarised in Chapter 5. A brief discussion of how far the developed experimental MGT system is from being ready for solar-hybrid operation is also

given, and recommendations for future work, to bring the system to commercial operation are suggested.

The calibration procedures for the instrumentation used on the experimental MGT system test bench are presented in Appendix A, while the developed data acquisition system GUI is added in Appendix B. Finally, the tabulated data obtained from both the modeling and the experimental work, the estimation of the uncertainty bounds in the measured and calculated parameters, and a sample calculation of the MGT system performance parameters are presented in Appendix C.

Chapter 2

Literature Review

This chapter reviews the available literature on the adaptation of gas turbine systems to solar-hybrid operation, with the focus on demonstrated plants. Brief discussions of studies that investigated turbocharger based solar MGT systems, and the transient behaviour of solar-hybrid gas turbine systems are given. A case study of a MGT system successfully developed from off-the-shelf turbocharger components is also provided. The chapter concludes with the identified research gaps that this study aims to address.

2.1 Solar-hybrid gas turbine systems

Current state-of-the-art central receiver CSP plants are based on steam turbine (Rankine cycle) technology (NREL, 2017), and only a few gas turbine (Brayton cycle) technology based plants have been demonstrated (European Commission, 2011, 2005; Korzynietz *et al.*, 2012). Gas turbine based central receiver CSP plants combine high concentration ratios of central receiver technology – and the resultant high receiver outlet temperatures – with typical gas turbine characteristics, such as quick start-ups, high power-to-weight ratio and multiple fuel applications (Boyce, 2012), to ensure both highly flexible and highly efficient power generation. In addition, a gas turbine is a low-water-usage technology – since there is no requirement for cooling water (Saravanamuttoo *et al.*, 2009) – and this makes it suitable for application in the arid and water scarce excellent solar resource region in Southern Africa. The use of gas turbine technology also allows implementation of hybridisation, in the form of combusting backup fuel, which ensures power production whenever demand occurs.

Several studies have been performed on solar-hybrid gas turbine systems. Most of these studies mainly focused on the solar components, with little or no focus on the gas turbine systems (Korzynietz *et al.*, 2012, 2016; Spelling *et al.*, 2012). Consequently, only a few solar-hybrid gas turbine systems have been demonstrated, with the usual approach involving selecting a gas turbine in

the desired power range and (physically) adapting it to solar operation (Aichmayer *et al.*, 2013; Spelling *et al.*, 2012). Challenges encountered in adapting gas turbines to solar operation included integrating the solar receiver and the externally heated air into the gas turbine systems, implementing a control system to switch gas turbine operation modes and also control any additional safety functions and devices and, modifying the combustion chamber to allow continuous operation at elevated inlet air temperatures and over a wide range of fuel/air ratios (Buck *et al.*, 2016; Fisher *et al.*, 2004; Ring *et al.*, 2004; Roberts, 1979; Sinai *et al.*, 2005).

Some of the earliest gas turbine focused solar-hybrid gas turbine system research work involved a study performed by Solar Turbines International (STI), and funded by the Electric Power Research Institute (EPRI) (Roberts, 1979). The aim of this study was to investigate the modifications required to adapt a commercially available STI Centaur recuperative gas turbine-generator set to solar-hybrid operation, with the two identified key technology gaps being in the fields of combustion and engine control. The standard STI Centaur recuperative gas turbine is a twin-shaft engine that operates on natural gas.

The study assessed the characteristics of both a parallel and series arrangement for the combustion chamber with the solar receiver. The parallel arrangement would necessitate the use of a modulating control valve upstream of both the solar receiver and the combustion chamber, either to isolate the solar receiver during the starting of the engine, and ensure that all the air flow passes through the combustion chamber or to isolate the combustion chamber during solar-only operation, and ensure that all the air flow passes through the solar receiver. This would in turn ensure that the combustion chamber does not impose a parasitic pressure loss on the cycle, when it is not in use. The control valves would also have to be programmed to maintain the desired maximum receiver outlet temperature, during solar-hybrid operation. A parallel arrangement would also result in the control valves and the combustion chamber being exposed to the normally encountered pressure and temperature conditions, implying that a combustion chamber similar to the standard production unit could be employed, with the only difference being that the new combustion chamber unit would employ both fuel staging – a strategy commonly used to tackle combustion instabilities in gas turbine engines, through varying the fuel mass flow rate to the different nozzles of a multiple nozzle combustion chamber – and some form of variable geometry in order to widen its fuel/air ratio operating range.

On the other hand, a simple series arrangement would avoid the complexity of using several control valves, but would impose a combustion chamber parasitic pressure loss on the cycle during solar-only operation. However, if the combustion chamber were to be isolated using control valves during solar-only operation, the employed control valves would then be exposed to the elevated receiver outlet temperature. This would therefore necessitate using low pressure drop and high temperature valves. The combustion chamber would also

be exposed to significantly higher inlet temperatures than normally encountered. Elevated inlet temperatures improve combustion chamber performance in terms of combustion efficiency, lean limit and smoke but may also result in ineffective liner wall cooling and fuel injector gumming.

After comparing the characteristics of either solar receiver-combustion chamber arrangement, a liquid fuel combustion system in parallel with the solar receiver was selected, mainly because it was considered to require the least development effort, given a combustion chamber similar to the standard unit could be employed. The study further recommended installing a flow dump valve between the solar receiver-combustion chamber and the turbine inlet for emergency engine over speed protection, in case of a sudden loss of electrical load and further proposed making use of a microprocessor-based electronic control system for start-up and shut-down scheduling, load control and emergency protection.

The European Commission (EC) previously funded three solar-hybrid gas turbine demonstration projects; SOLar hybrid GAs Turbine Electric (SOLGATE) power system, SOLar-HYbrid power and COgeneration (SOLHYCO) plants and SOLar Up-scale GAs turbine System (SOLUGAS). The overall objective of these projects was to demonstrate the technical feasibility and cost reduction potential of solar-hybrid gas turbine systems, with the focus on improvement in receiver design and performance (European Commission, 2011, 2005; Korzynietz *et al.*, 2012).

The SOLGATE project was the first EC funded solar-hybrid gas turbine demonstration project, and its main goal was to prove the technical feasibility of a solar-hybrid gas turbine power system and verify the electricity cost reduction potential of such a system (European Commission, 2005). The system was installed in the CESA-1 tower facility at the Plataforma Solar de Almería (PSA) in Spain, and consisted of a cluster of three receiver modules – low temperature (LT), medium temperature (MT) and high temperature (HT) – connected in series and a micro gas turbine based on a modified Allison Model 250 helicopter turboshaft engine. This engine has a twin-spool, twin-shaft configuration, and has a rated maximum continuous power output of 270 hp, at an output shaft rotational speed of 6016 rpm.

The modifications to the helicopter engine were performed by ORMAT, with the developed gas turbine then aptly named ORMAT Solar Turbine 3 (OST3). Similar to the work of Roberts, the modification focused on the engine's combustion and control systems. Modifications to the engine's combustion system included addition of an external combustion chamber, manufactured from a nickel based super alloy and capable of operating at elevated inlet air temperatures of up to 800 °C. The elevated combustion chamber inlet air temperature necessitated making additional provision for supplying cooling air to the gas turbine bearings. To accomplish this, two pipes bypassing the solar receivers were added to supply cooling air directly from the compressor, and a special air seal was added, to prevent hot air from the receivers from

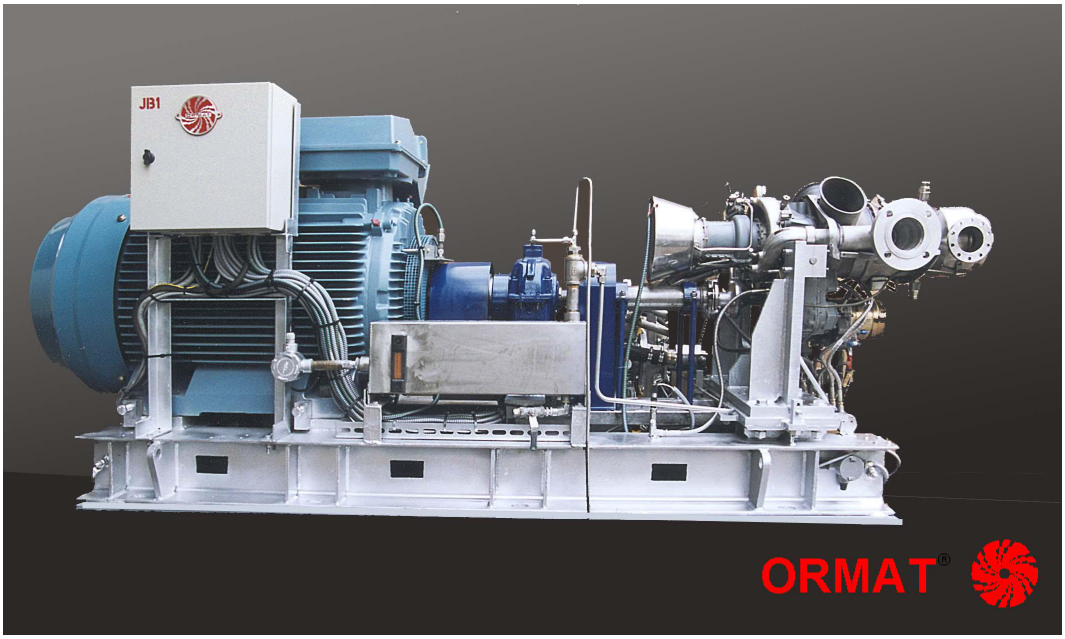

Figure 2.1: OST3 micro-gas turbine (European Commission, 2005)

entering the gas turbine bearings. A new fuel injector and a new ignition system were also installed, to allow continuous operation at elevated temperatures and over a wide range of fuel/air ratios. An electronic fuel shut off valve and a digital fuel metering valve - the latter with a provision for returning most of the fuel back to the fuel pump during periods of high solar shares - were also added. The modifications to the control system included implementation of new control logic and coefficients, with the capability to switch gas turbine operation modes and also control any additional safety functions and devices. The modified engine was further coupled to a 250 kW_e electric generator through a gearbox, and a more powerful starter unit was also installed (see Figure 2.1).

Experimental tests were performed in two phases; phase 1 tests were to demonstrate the operational capability of the gas turbine together with the three receiver modules to reach the design point receiver cluster outlet temperature of 800 °C, while the main objective of the phase 2 tests was to increase the receiver cluster outlet temperature to 1000 °C.

Phase 1 tests achieved the design operation conditions of 800 °C for three test days and test data obtained for one of the days showed that for a DNI value of 900 W/m^2 and a solar field consisting of 55 focused heliostats, air temperatures in the receiver modules increased from about 300 °C at the LT-module inlet, to about 800 °C at the HT-module outlet, at an absolute air pressure of 6.5 bar and a pressure drop of 120 mbar across the receiver cluster. The solar share was about 60 %, corresponding to 650 kW_t solar thermal energy output from the receivers. A total of 73 hours of gas turbine operation

time were accumulated throughout the phase 1 tests – 51 of them under solar operation – and a net electricity output of 227 kW_e, at a net simple cycle efficiency of 18.2 % was realised.

Phase 2 tests achieved a HT-module receiver outlet air temperature of about 960 °C, and not the required 1000 °C. Obtained test data showed that for a DNI value of 770 W/m^2 and a solar field consisting of 45 focused heliostats, air temperatures in the receiver modules increased from about 300 °C at the LT-module inlet, to about 960 °C at the HT-module outlet, at an absolute air pressure of 5.5 bar and a pressure drop of 120 mbar across the receiver cluster. The solar share was about 70 %, corresponding to a 700 kW_t solar thermal energy output from the receivers.

An unsuccessful emergency shutdown resulted in damage to the turbine, and this cut short the phase 2 tests. A total of 61½ hours of gas turbine operation time were accumulated during the phase 2 tests – 45½ of them under solar operation – and an electricity output of 170 kW_e, at a simple cycle efficiency of 18 % was realized (European Commission, 2005; Fisher *et al.*, 2004; Ring *et al.*, 2004; Sinai *et al.*, 2005; Heller *et al.*, 2006).

The SOLHYCO project followed the SOLGATE project and the main objective of this project was to develop and test a highly efficient, reliable and economic solar-hybrid co-generation system based on a 100 kW_e MGT system, with a capacity to operate in parallel on varying contributions of solar power input and fuel. The main project objective was to be achieved through first illustrating the use of bio-diesel for co-firing purposes, thus ensuring 100 % renewable operation, and then modifying a commercially available Turbec T100 Microturbine for solar-hybrid co-generation application. This MGT system normally operates on natural gas, in combined heat and power (CHP) applications. The bio-diesel solar-hybrid tests employed the SOLGATE project test set up, with the MGT system that originally used kerosene as backup fuel now adapted to bio-diesel operation, and only using kerosene for start-up.

The adaptation of the MGT system to bio-diesel operation was reported to entail only slight modifications, such as adapting the control system to the slightly increased fuel flow – as a result of the lower calorific value of the bio-diesel – and replacing the valve and filter seals with those suitable for bio-diesel operation.

Unidentified technical problems with the MGT system during the initial bio-diesel operation cut short the tests, and a total of 100 hours of gas turbine operation – 57 under solar operation – were accumulated, and a maximum electricity output of 160 kW_e was realised.

The solar-hybrid MGT system co-generation operation employed the Turbec T100 Microturbine because it made provision for attaching both an external combustion chamber and an external flow path connecting the receiver to the combustion chamber. Other modifications to the standard MGT system included adapting it to diesel operation, increasing the turbine inlet temperature from 600 °C to 800 °C and fitting a second parallel combustion chamber

to make provision for two parallel heat sources. New control logic was also implemented, to control the two parallel heat sources.

Several challenges were faced during the tests with the modified Turbec T100 Microturbine, including difficulty controlling the heat supplied by the two parallel heat sources (solar plant and the combustion chamber), an inability to handle the high turbine inlet air temperatures, receiver cavity defects and unsatisfactory combustion during the micro gas turbine start-up. A maximum electrical power output of 70 kW_e, at a solarised turbine efficiency of about 24.9 % was realised during the co-generation tests, and a total of 165 hours of gas turbine operation were accumulated – 100 under solar operation, including 2 hours of the first ever solar-only micro-gas turbine operation (European Commission, 2011).

The SOLUGAS project was started in November, 2008 and commissioned in May, 2012 at the Abengoa Solar Solúcar Platform in Seville, Spain. Through the coordination of Abengoa Solar, and with the support of an international consortium comprising of the German Aerospace Center (Deutsches Zentrum für Luft-und Raumfahrt, DLR), Turbomach (a subsidiary company of Solar Turbines Incorporated), Kelvion Sp. z o.o. (former GEA Technika Cieplna Sp. z o.o.) and New Energy for Algeria (NEAL), the project's main objective was to demonstrate the performance and cost reduction potential of a solar-hybrid gas turbine system on a pre-commercial scale, through building on the research experience in receiver design and development gained through the preceding SOLGATE and SOLHYCO projects (Korzynietz *et al.*, 2012).

SOLUGAS was the first demonstration project at megawatt scale, and the project adapted Solar Turbines Incorporated's *Mercury*^{TM}50 recuperated gas turbine, which has a nominal electrical power rating of 4.6 MW_e, at an engine efficiency of 38.5 %. Modifications to the standard gas turbine unit were performed by Turbomach and focused on the engine air flow path and investigating combustion chamber operation at higher temperatures.

The gas turbine modifications included replacing the recuperator with the solar receiver, with the connection between the receiver outlet and combustion chamber inlet achieved using internally insulated piping, so as to reduce thermal expansion. Piping bypassing the solar receiver, complete with controllable valves was also fitted, firstly, to regulate the air mass flow and temperature upstream of the combustion chamber, and secondly, to allow pressurised air flow direct from the compressor to the combustion chamber, so the gas turbine could be operated in the conventional mode with one heat source, during periods of low or no solar insolation. The adapted gas turbine was reported to show stable operation and a good ramp up behaviour during solar operation and an electrical output of 4 MW_e was realized. Over 1000 gas turbine operation hours were accumulated over a period of 18 months (Korzynietz *et al.*, 2016, 2012; Quero *et al.*, 2013).

Despite the reported successful solar operation of the *Mercury*^{TM}50 gas turbine system during the SOLUGAS project, there are no reported follow

up solar-hybrid gas turbine systems developed, drawing upon this project's success.

More recently, the EC funded the Optimised Micro turbine Solar Power (OMSoP) CSP demonstration project. The MGT system was intended to be of a modular design, with the capability of producing 3 to 10 kW of electricity. This demonstration project began in 2013, with a consortium of 8 partner organisations from 5 European countries, and a total budget of €5.8 million. The solar power system was based on parabolic dish concentrator technology, but with the Stirling engine replaced with a MGT system designed by the City University of London. The project concluded in 2017. Experimental tests showed overheating of the MGT system bearings, which limited the turbine inlet temperature (TIT) to a maximum of 270 °C, well below the design point value of 800 °C. Consequently, a useful work output of only 0.9 kW was realised from the experimental tests (City University of London, 2018).

The latest solar-hybrid gas turbine system referenced in literature is AORA Solar's Tulip^{TM} co-generation system (Aichmayer *et al.*, 2013; Spelling *et al.*, 2012; Buck *et al.*, 2016), with a rated electrical and thermal power output of 100 kW_e and 170 kW_t, respectively. This system is installed at two research and development sites; Kibbutz Samar, in Israel and Plataforma Solar de Almería, in Spain, with the former commissioned in 2009, while the latter was commissioned in 2012 (AORA Solar, 2015). However, there is no published literature readily available on the performance of these two demonstration plants.

At Stellenbosch University, research on the *solarization* of MGT systems is conducted in the context of the SUNSPOT cycle, as part of a concerted effort to develop technology that can lead to the commercialisation of this cycle. Previous studies all focused on the *solarization* of an in-house Rover 1S/60 MGT system (see Figure 2.2). The Rover engine was developed in the 1950's, and is a single-shaft industrial gas turbine system, with a rated maximum continuous power output of 45 kW, at a rotational speed of 46 000 rpm (Rover Gas Turbines Limited, 1967).

Luiten (2015) evaluated the performance of the original centrifugal compressor, using both computational fluid dynamics (CFD) and experimental approaches. To counter the pressure losses expected to be introduced by the addition of a solar receiver, Luiten designed a new centrifugal compressor for maximum total-to-static pressure ratio. The new design was predicted to increase the compressor total-to-static pressure ratio from 2.5 to 3.3, corresponding to an increase in total-to-static isentropic efficiency of 21.8 %.

Homann (2015) investigated the effect of solar-hybridization on the performance of the Rover MGT system, with the solar thermal energy input modeled as an incremental 0 to 200 kW thermal energy input. Homann further modeled the effect of the new compressor designed by Luiten on the performance of the MGT system under both standard and solar-hybrid operation, and predicted an improvement in the performance of the MGT system in both operation

(a) Front right view **(b)** Rear left view

Figure 2.2: Rover 1S/60 MGT system test bench (Luiten, 2015)

modes. Homann also investigated a new air flow path for the Rover MGT system under solar-hybrid operation, as well as the potential to commercialize solar-hybrid gas turbine systems.

Zhang (2016) aimed to convert the MGT system from kerosene to liquefied petroleum gas (LPG) operation. Zhang replaced the original fuel system, and successfully ran the MGT system on LPG, albeit at a lower rotational speed than that observed when running on kerosene.

As a continuation of Zhang's work, Marsh (2019) sought to improve on the performance of the MGT system, and possibly match that observed for kerosene. Marsh improved the fuel control system, and successfully ran the MGT system on propane at full speed and 77 % of rated power, closely matching the performance observed for kerosene. Marsh further proposed a general method for converting a gas turbine from liquid to gaseous fuel operation.

More recently, Schommarz (2019) performed both CFD and finite element analyses on the centrifugal compressor designed by Luiten. After verifying the predicted increase in total-to-static pressure ratio, as well as proving its structural integrity under expected gas turbine operating conditions, Schommarz manufactured the new compressor. However, this compressor is yet to be fitted into the Rover gas turbine and tested.

Turbocharger based solar MGT systems

The development of turbocharger based solar MGT systems has in the past been proposed by studies such as Gallup and Kesseli (1994) and Kesseli and Wells (1989), and more recently, le Roux *et al.* (2011*a*,*b*, 2012) and le Roux and Meyer (2016), mainly for solar-only parabolic dish Brayton cycle applications. Gallup and Kesseli and Kesseli and Wells proposed a 30 kW_e twin shaft parabolic dish/Brayton solar MGT system based on the then commercially

available Schwitzer Inc. turbocharger units, as an alternative to parabolic dish/Stirling engine solar systems. The use of turbocharger technology was to ensure low cost and high reliability of the turbomachinery. However, the proposed parabolic dish/Brayton solar MGT system was never commissioned.

le Roux *et al.* (2011*a*,*b*, 2012) and le Roux and Meyer (2016) modeled the micro-turbine of their small-scale dish-mounted solar thermal Brayton cycle system based on off-the-shelf Garrett turbochargers. Their work focused on the use of the method of total entropy generation minimisation to optimise system components, such as the solar receiver and the recuperator, for maximum net work output. The goal is to eventually develop an experimental test set up at the University of Pretoria.

Transient behaviour of solar-hybrid gas turbine systems

In contrast to the few demonstrated plants, several thermodynamic studies have been performed on solar-hybrid gas turbine systems. The majority of these studies investigated the steady-state operation of the gas turbine systems, and only a few considered the transient behaviour of the systems.

Some of the most recent studies performed on the transient behaviour of solar-hybrid gas turbine systems include Felsmann *et al.* (2014, 2015) and Kathirgamanathan and Axelsson (2018). Felsmann *et al.* (2014) investigated the effect of both rapid and slow increase/decrease in solar thermal energy input on the dynamic behaviour of the 12 MW THM 1304-12 MAN Diesel & Turbo SE gas turbine, with the variable solar energy resource simulated by both a fast and a gradual increase/decrease of a 0 to 29 MW thermal energy input. As a continuation of the initial study, Felsmann *et al.* (2015) investigated the effect of fast load changes in the network and generator load rejection on the transient behaviour of the same gas turbine system.

Kathirgamanathan and Axelsson focused on the effect of thermal inertia and additional pressurised air volume on the rotor over-speed of the 1.85 MW OP16 gas turbine system integrated in a hybrid solar thermal power plant, during load shedding and emergency shut downs. As possible safety measures, these studies all proposed a combination of fast acting flow control valves – air flow control valves, to re-direct the air flow, and allow the switch from solar to non-solar gas turbine operation mode, and fuel control valves, to either regulate or cut-off the fuel supply – and a blow-off valve – to vent the solar heated air. Other safety measures proposed in literature include the use of mechanical brakes and shunt resistors loading the generator (Buck *et al.*, 2016).

2.2 Application of a turbocharger as a MGT system

According to Visser *et al.* (2011), the emergence of MGT system applications for both power and thrust generation, especially for levels below 100 kW, has led to various futile attempts at developing MGT systems with efficiency and reliability levels as high as those of larger gas turbines. Challenges to the development of these MGT systems include technical limitations arising from their small size, and the costs involved in the development of highly efficient MGT systems optimized for a particular cycle.

In terms of cost, off-the-shelf turbochargers offer a viable option for application as MGT systems, as they are a mass product of the automotive industry. Also, the performance and efficiency of modern small turbochargers have greatly improved, making them suitable for Brayton cycle applications. In addition, efficient high-speed electric generators are now more accessible, at relatively affordable prices.

To reduce costs, Visser *et al* developed a 3 kW recuperated MGT system for CHP applications in large households and truck auxiliary power unit (APU) heating systems, based on off-the shelf turbocharger technology. Development work started in 2008, and their first prototype, also referred to as 'Mk4', was developed as a proof of concept. It combined off-the-shelf turbocharger components with components built in-house at Micro Turbine Technology MTT b.v. The off-the-shelf turbocharger components included the compressor, turbine and bearings, while the in-house built components included the radial permanent-magnet type generator, turbine shaft coupling, recuperator and combustion chamber.

Through the assessment of component performance maps found in literature, and performing component matching, a suitable turbocharger turbine and compressor were selected. To ensure minimal modification work, the chosen turbine and compressor were fitted to the same shaft and bearing unit. Using a special coupling, an electric generator was fitted to the same shaft, with the generator speed controller then used to control the shaft speed. A combustion chamber was designed based on a single-can layout, and had to cover both recuperated cycle and simple cycle thermal conditions, at a maximum operation pressure of 3 bar and a maximum permissible pressure loss of 2%. The recuperator selection was guided by the requirement to meet thermal efficiency targets and low permissible pressure losses. The other factor considered was material constraints, owing to the expected high recuperator gas-side inlet temperature of up to 750 °C. A primary-surface stainless steel recuperator, with 100 hours of projected test life, was selected and fitted onto the Mk4 MGT system.

The tests to prove the operational capability of the MTT MGT system were performed in three phases, with the final objective being to obtain elec-

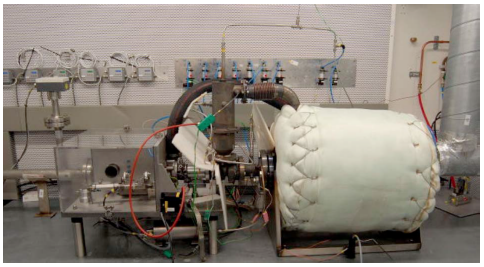

Figure 2.3: MTT MGT system test rig (Visser *et al.*, 2011)

Figure 2.4: Mk5 MGT system (Visser *et al.*, 2012)

trical power output of 3 kW_e, at a cycle efficiency of 16 %. The three phases of tests were: gas generator tests, simple cycle turboshaft tests and recuperated turboshaft tests. A test rig that could measure different parameters like pressure, temperature, air and fuel mass flow rate, rotational speed, exhaust gas composition and power output was developed (see Figure 2.3). The performance of the MTT MGT system was then determined through analysing the obtained test data. In addition, an energy balance was performed, in order to determine the system losses.

The gas generator tests were performed as a proof of concept, and included a validation of the predicted model performance, as well as component matching. The simple cycle turboshaft tests were used to develop an optimal turbine-generator configuration. The recuperated turboshaft tests were performed in order to validate the recuperated cycle model predictions and recuperator design, with the objective being to obtain a cycle efficiency of at least 12 %.

From the gas generator tests, the equivalent power at almost international standard ambient (ISA) conditions of 1011 mbar and 294 K was 3.25 kW, at a thermal efficiency of 6.34 %. This was measured at a nominal rotational speed of 240 000 rpm, and a calculated adiabatic turbine inlet temperature of 1369 K. These results corresponded with the model predictions obtained from the gas turbine simulation program (GSP). In the simple cycle tests, the turbine was coupled to the electric generator using different coupling techniques, and the optimal coupling configuration was obtained. At a rotational speed of 218 000 rpm, an electrical power output of about 2.8 kW_e (ISA corrected) was measured, at an electric efficiency of 6.28 %.

Finally, in the recuperated cycle turboshaft tests, a 2.7 kW_e , at a 12.2 % (ISA corrected) cycle efficiency, for a rotational speed of 240 000 rpm, was obtained, using a custom designed recuperator with an 85 % effectiveness and less than 4 % pressure loss. The test analysis with GSP showed a compressor isentropic efficiency of 73.8 % and a turbine efficiency of 67 %.

The obtained results proved the technical feasibility of using a turbocharger as a recuperated MGT system, for micro CHP applications. Future development work would aim to improve the cycle efficiency levels to almost 20 %,

through improving individual component efficiencies.

Following the proof of concept, Visser *et al.* (2012) embarked on optimizing the performance of individual components of the developed MGT system, with the focus on achieving 3 kW_e electrical power output, at a cycle efficiency of 16.5 %. An experimental MGT system with a different rotor configuration, and components with improved performance was developed. This MGT system was referred to as 'Mk5' (see Figure 2.4).

Using information from original equipment manufacturers (OEM)s, component models and engineering judgement, the potential for improving the performance of the individual components was investigated. Some of the individual components considered included: the compressor, turbine, combustor, recuperator and fuel compressor. The effect of heat losses from the hot parts of the gas turbine on the overall cycle efficiency was also assessed.

For the compressor, the pressure ratio – at the nominal rotational speed of 240 000 rpm and turbine inlet temperature of about 1300 K – needed to be increased to the optimal value of 3, and if possible up to a value of 3.4, in order to maximise the power output. The pressure ratio was increased through increasing the impeller blade tip diameter, with both experimental and CFD analysis used to assess the effect of increase in tip diameter on the performance.

For the Mk5 MGT system, a more advanced turbine was fitted (with isentropic efficiency of up to 70 %) compared to that which was available to the Mk4 MGT system. The high efficiency was obtained through optimising the scroll design and doing away with the waste gate.

The Mk5 combustor was developed based on the 'classic' combustor concept, following design guidelines given by Lefebvre and Ballal (2010) and Mellor (1990). This design ensured combustion completeness greater than 0.995 and pressure loss of less than 1.5 %. Operation issues with this design included high NO_x emission, insufficient flame stability and overheating. Therefore, work on improving the performance of the combustor was considered incomplete.

The Mk5 recuperator was based on an all-625 cube shaped plate-pin design. This replaced the all-primary surface stainless steel Mk4 recuperator. The Mk5 recuperator had a lower installed hydraulic resistance, a cycle reference point combined relative pressure loss of (2.05 + 2.50 %) and a high effectiveness, ranging from 88 to 91 %, in comparison to the Mk4 recuperator. The recuperator insulation was also improved by using inorganic silicate insulation boards, with low thermal conductivity.

The fuel compressor was the final component worked on. It was an off-the-shelf wobble piston type, that satisfied performance and low cost requirements. Adaptation included modification of the bearing seals, to reduce friction.

Analysis of the test results showed that the improvement in the performance of individual components led to an increase in the cycle efficiency, from 12.2 % to 17.2 %, at an electrical power output of 3.4 kW_e. Further improvement in the cycle efficiency could be achieved through improving the turbine efficiency and reducing losses in the auxiliary components.

2.3 Conclusion

Despite the several studies performed on solar-hybrid gas turbine systems, only a handful of projects have been demonstrated. Currently, there are no commercial solar-hybrid gas turbine systems readily available off-the-shelf. Several operational and control challenges still exist and significant development effort is still required to provide technically proven units. However, there is a reluctance from gas turbine manufacturers to develop these systems, given the significant effort and time required, and the high costs involved (Augusto, 2018).

Notably, the available literature does not consider the effect of variable solar thermal energy input on the complete operating range of speed and power output of the adapted gas turbine systems. In addition, the available literature does not specify at what levels of solar share is solar-hybrid operation not possible or suitable, to dictate when to switch from solar to non-solar (standard) gas turbine operation mode. Furthermore, very little attention is paid to the transient behaviour of MGT systems under solar-hybrid operation. The work presented in this study therefore aims to contribute to addressing these gaps in knowledge.

Studies such as Visser *et al.* (2011) and Visser *et al.* (2012) demonstrate the technical feasibility of developing MGT systems based on off-the-shelf turbocharger technology. Turbochargers are readily available, given they are a mass product of the automotive industry. The performance and efficiency of modern turbochargers have greatly improved, making them suitable for Brayton cycle MGT system applications. The use of turbocharger technology allows for easy coupling of the individual MGT system components, some of which could be specially designed for solar-hybrid operation. Therefore, the integration of the solar receiver and the externally heated air into the gas turbine systems should be achievable with minimal complications. In contrast, most conventional gas turbine systems are highly compact, and may require significant modifications to successfully adapt them to solar-hybrid operation.

Chapter 3

Theoretical Modeling Work

A mathematical model to predict both the steady-state and the transient performance of the MGT system under solar-hybrid operation was created in MATLAB R2017a. The modeling of the steady-state performance of the MGT system was done to, firstly, predict the possible operating range and determine an equilibrium running point for the MGT system under solar-hybrid operation, secondly, predict the nominal rating for the proposed solar-hybrid MGT system, when operating at the determined equilibrium running point, and lastly, predict the effect of the variable solar energy resource and ambient conditions on typical gas turbine performance parameters. The transient modeling was performed in order to predict the transient response of the MGT system to sudden changes in solar irradiation/solar thermal energy input.

3.1 Modeling procedure

The modeling used meteorological data for four arbitrarily selected solar days, one for each of the four climatic seasons experienced in Southern Africa. Modeling of the steady-state performance of the MGT system under solar-hybrid operation used hourly averaged meteorological data for a winter day (04 August, 2016) and a summer day (04 January, 2017). On the other hand, modeling of the transient behaviour of the MGT system under solar-hybrid operation used minute averaged meteorological data. The minute averaged data corresponded to the shortest time step data available. In addition to the two solar days considered for the steady-state performance, modeling of the transient behaviour of the MGT system also considered an autumn day (01 April, 2017), and a spring day (01 October, 2017). The two additional days' data allowed investigating the transient behaviour of the MGT system at intermediate solar thermal energy levels.

Firstly, the solar resource was modeled, in order to estimate the available solar thermal energy, and then, using component models and actual performance characteristics of the individual MGT system components, the matching

of the individual MGT system components was performed, over the complete operating range of speed and power output of the MGT system. From the matching of the individual MGT system components, the equilibrium running (operating) points for the MGT system under both standard and solar-hybrid operation were obtained.

Solar-hybrid operation requires the combustion of backup fuel, in order to raise the temperature of the pressurised air stream to the desired equilibrium running gas-generator TIT. To determine the required fuel mass flow rate, an analysis of the chemical reaction that takes place in the combustion chamber during solar-hybrid operation was performed. The variation in the working fluid properties, due to changing conditions throughout the cycle, was also modeled.

It is desirable for hybrid CSP systems to operate at the maximum solar share possible, in order to minimise fuel consumption. High solar resource regions generally experience high ambient temperatures, and may also be located at altitude, thus experiencing low ambient pressures. The steady-state performance of the MGT system under solar-hybrid operation was therefore analysed through studying the effect of increasing solar share and changing ambient conditions on typical gas turbine performance parameters, such as the gas-generator TIT, specific fuel consumption, useful work output and cycle thermal efficiency, when operating at the determined solar-hybrid equilibrium running point, during hours of sufficient solar irradiation.

The potential for improving the cycle thermal efficiency of the solar-hybrid MGT system, through adding recuperation, was also considered. The modeling of the recuperation followed a simplified approach that required no knowledge of the geometry of the recuperator.

The transient performance of the MGT system under solar-hybrid operation was analysed through studying the effect of sudden changes in the solar thermal energy input on transient gas turbine performance parameters, such as the gas-generator rotational speed and TIT. The fuel mass flow rate needed to either accelerate or decelerate the solar-hybrid MGT system, in order to maintain it operating at the determined solar-hybrid equilibrium running point, and the resultant MGT system useful work output were also determined.

The predicted performance of the MGT system was theoretically validated through analysing the effects of high and low ambient temperatures and pressures on the performance of the MGT system under standard operation, over the course of a cold (winter) and a warm (summer) day. The predicted behaviour of the MGT system was compared to that expected of a conventional gas turbine operating under similar conditions.

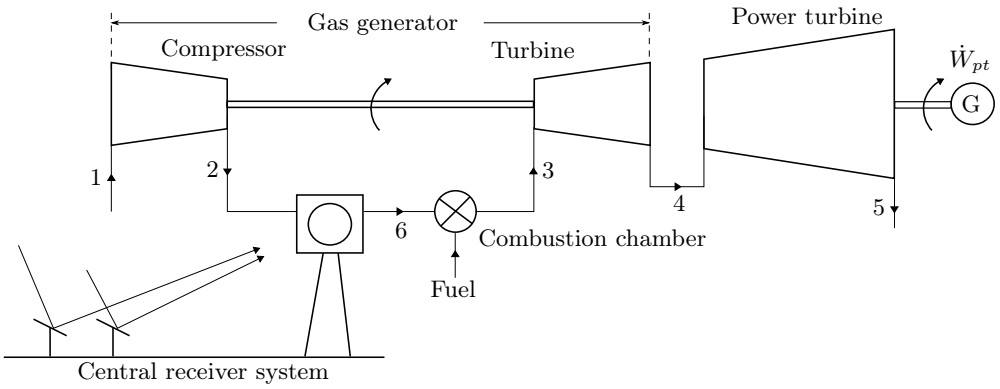

Figure 3.1: Schematic layout of a central receiver solar-hybrid twin-shaft MGT system

3.2 System configuration and components

The solar-hybrid MGT system was modeled based on an open-cycle twin-shaft engine (see Figure 3.1); where a high-pressure turbine drives a high-pressure compressor, and the two act as a gas-generator for a low-pressure and mechanically independent (free) power turbine. The power turbine in turn drives an electrical generator, which converts mechanical work into electrical power.

The twin-shaft arrangement allows for flexibility in operation, which is advantageous given the variable nature of the solar energy resource. The twin-shaft arrangement also has the added advantage of ease of starting, as only the gas-generator needs to be turned (Saravanamuttoo *et al.*, 2009).

The numbers 1 and 2 in the schematic layout denote the gas-generator compressor inlet and outlet stations, 3 and 4 denote the gas-generator turbine inlet and outlet stations, 4 and 5 denote the power turbine inlet and outlet stations and 6 denotes the combustion chamber inlet station. Similarly, 2 and 6 denote the solar receiver inlet and outlet stations and 3 denotes the combustion chamber outlet station.

The operation of the solar-hybrid MGT system is based on the Brayton cycle, which can be represented on a temperature-entropy (T-s) diagram, as shown in Figure 3.2. In this cycle, ambient air is first compressed in the compressor from state 01 to state 02. During periods of sufficient solar irradiation, the temperature of the pressurised air leaving the compressor T_{02} is raised to the desired gas-generator TIT T_{03}, through direct solar heating in the solar receiver. For periods of insufficient solar irradiation, the temperature of the pressurised air leaving the solar receiver T_{06} is raised to the desired gas-generator TIT, through combusting backup fuel – assumed to be propane – in the combustion chamber. The hot gases are then expanded; first in the gas-generator turbine (state 03 to state 04), to meet the gas-generator compressor work requirement, and thereafter in the power turbine (state 04 to state 05),

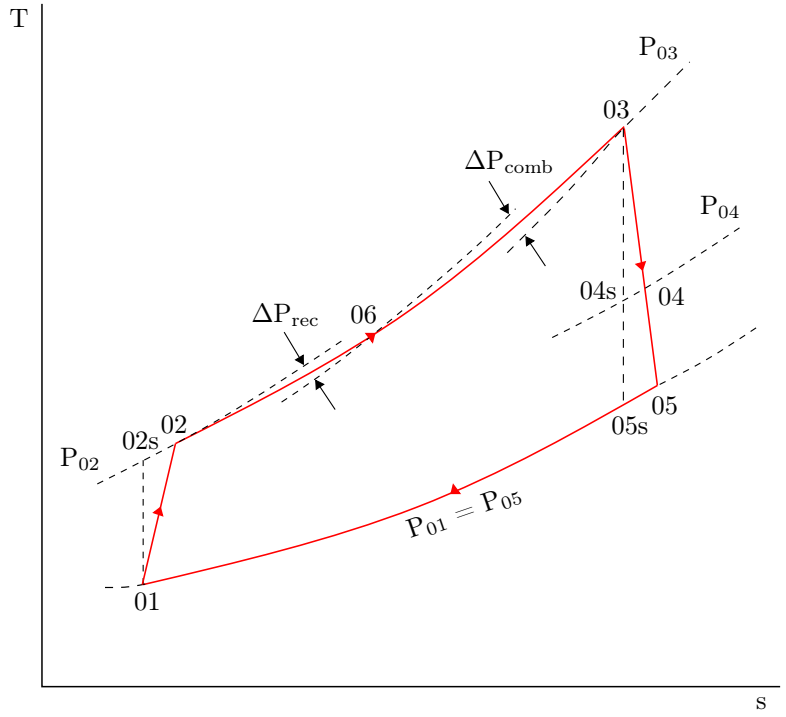

Figure 3.2: T-s diagram for the solar-hybrid twin-shaft MGT Brayton cycle

to generate useful shaft work. The power turbine exhaust gases are finally exhausted to the atmosphere. The state 02s corresponds to the final state of the isentropic compression process, while 04s and 05s correspond to the final states of the isentropic expansion processes. All these processes are assumed to be adiabatic.

Pressure losses occur in the solar receiver and in the combustion chamber, due to fluid friction and the momentum changes resulting from the addition of heat to the moving fluid. These pressure losses are denoted by the terms ΔP_{rec} and ΔP_{comb} on the T-s diagram. Additionally, pressure losses occur in the ducts connecting the individual components of the MGT system. These duct losses were included in the associated component losses. This study also assumed short intake and exhaust ducts, to ensure negligible intake and exhaust pressure losses. The net effect of all these pressure losses is a reduction in the pressure ratio available to the power turbine, which results in a reduction in the useful MGT system work output.

The performance of the solar-hybrid MGT system was predicted using the actual performance characteristics of the individual components of the solar-hybrid MGT system. These components, and their actual performance characteristics are discussed in turn, as follows:

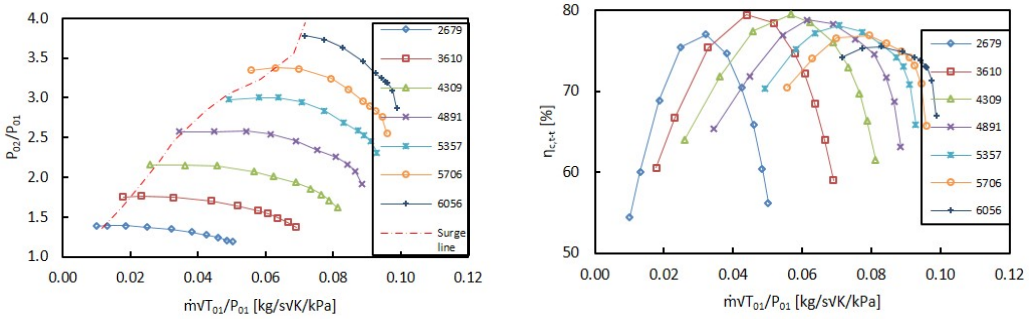

(a) **(b)**

Figure 3.3: Gas-generator compressor performance characteristics (Heuer, 2016); non-dimensional mass flow rate vs (a) total-to-total pressure ratio and (b) total-to-total isentropic efficiency

3.2.1 Gas-generator

The gas-generator of the MGT system was modeled based on a commercially available BorgWarner Turbo Systems turbocharger (Model: K31 Part no. 53319880025), and the operating range of the gas-generator was restricted by that of the K31 turbocharger. This turbocharger has a compressor impeller exducer diameter of 94.9 mm and a turbine rotor inducer diameter of 86 mm.

BorgWarner Turbo Systems provided performance test data for the K31 turbocharger (Heuer, 2016). This test data was used to generate the gas-generator compressor and turbine performance characteristics. These performance characteristics were described by two sets of curves; compressor total-to-total pressure ratio P_{02}/P_{01} and isentropic efficiency $\eta_{(c,t-t)}$ plotted against the non-dimensional mass flow rate $\dot{m}\sqrt{T_{01}}/P_{01}$, along each constant non-dimensional rotational speed line $N/\sqrt{T_{01}}$ (see Figure 3.3), and turbine non-dimensional mass flow rate $\dot{m}\sqrt{T_{03}}/P_{03}$ and overall turbocharger efficiency η_{TC} plotted against the total-to-static pressure ratio P_{03}/P_4, along each constant non-dimensional rotational speed line $N/\sqrt{T_{03}}$ (see Figure 3.4).

3.2.2 Combustion chamber

The combustion chamber of the MGT system was modeled based on a tubular type combustion chamber designed and manufactured by Hummel (2014). This combustion chamber was designed for application on a MGT system similarly based on the K31 turbocharger. The design process was mainly based on the work of Conrado *et al.* (2004), Lefebvre and Ballal (2010) and Lilley (1977).

The combustion chamber was designed for a total pressure loss of 5 % of the compressor delivery pressure, at a design point combustion chamber inlet volume flow rate of 0.173 m^3/s. Cold flow tests were performed for the

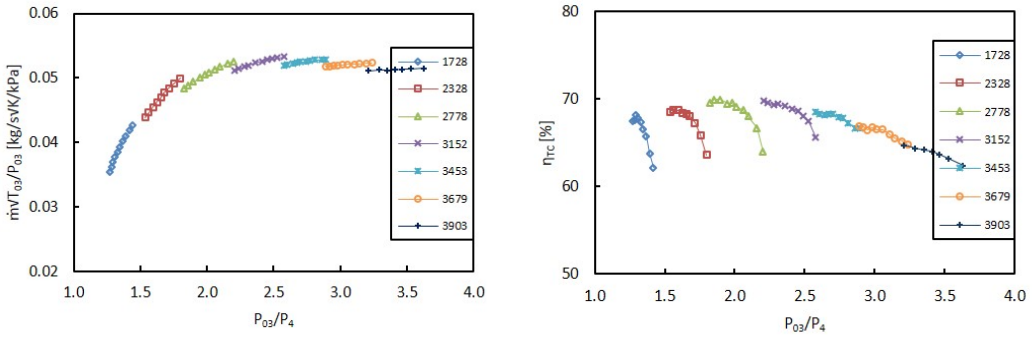

(a) (b)

Figure 3.4: Gas-generator turbine performance characteristics (Heuer, 2016); total-to-static pressure ratio vs (a) non-dimensional mass flow rate and (b) overall turbocharger efficiency

combustion chamber on a test rig at the Institute of Thermal Turbomachinery and Machinery Laboratory (ITSM), University of Stuttgart. A second-order polynomial curve was fitted through a plot of the measured cold flow pressure loss $\Delta P_{comb,cold}$ (in Pa) against the calculated combustion chamber inlet volume flow rate $\dot{V}$, with the following function obtained for the curve-fit

$$\Delta P_{comb,cold} = 393096\dot{V}^2 - 343.07\dot{V} + 262.19 \tag{3.1}$$

Equation 3.1 was used to model the pressure loss in the combustion chamber. Only the cold flow or frictional pressure loss was considered, with the typically much smaller fundamental pressure loss resulting from the exothermic reaction neglected. According to Lefebvre and Ballal, only the cold flow pressure loss is normally considered, because it can be measured with reasonable accuracy.

However, if required, the hot flow pressure loss can be estimated from Raleigh line gas dynamics, for a given temperature rise in the combustion chamber. Typical values for the cold flow pressure loss range from 4 to 8 %, while those for the fundamental pressure loss range from 0.5 to 1.0 %, for combustion chambers of moderate temperature rise.

The combustion chamber was modeled in a series arrangement with the solar receiver, with the former downstream of the latter (see Figure 3.1). A series arrangement avoids the complexity of multiple usage of flow control valves, which is inherent to a parallel arrangement, but results in a higher pressure loss, since the total pressure loss is a sum of the pressure losses in each of the components connected in series (Buck *et al.*, 2016) – as is the case with ordinary pipe flow.

Coogan *et al.* (2013) compared the two solar receiver-combustion chamber configurations based on solar energy utilisation and emissions, as a function

of the average combustion chamber equivalence ratio – which is defined as the actual fuel/air ratio divided by the stoichiometric fuel/air ratio. Coogan *et al.* found that a parallel arrangement would necessitate operating with a very high flame temperature, to ensure maximum utilisation of the solar energy.

For their study, Coogan *et al.* set the turbine inlet temperature (1150 °C) higher than the receiver outlet temperature (1000 °C). A parallel arrangement necessitated raising the temperature of the compressed air to at least the set receiver outlet temperature, in both the combustion chamber and the solar receiver, with the remaining temperature rise achieved through additional combustion. To minimise the additional combustion – and ensure maximum solar share – the air mass flow through the combustion chamber had to be reduced, which would then result into a very high flame temperature. Nevertheless, the achieved solar share for a parallel arrangement would still be lower than that for a series arrangement.

Since it's desirable for hybrid CSP plants to utilise the maximum solar energy possible, a series solar receiver-combustion chamber arrangement was preferred over a parallel arrangement. To tackle challenges such as auto-ignition and flashback, which occur due to the elevated combustion chamber inlet air temperatures experienced in a series arrangement, Coogan *et al.* proposed a multibank micromix injector design.

3.2.3 Power turbine

The power turbine of the MGT system was modeled based on the turbine of a commercially available BorgWarner Turbo Systems turbocharger (Model: K44 Part no. 53449886900), and the operating range of the power turbine was restricted by that of the K44 turbocharger. The turbine of this turbocharger has rotor inducer and exducer diameters of 140 mm and 124.85 mm, respectively.

The power turbine was sized using a Cordier diagram for single stage turbines and expanders operating with compresible fluids, found in Balje (1981). From the Cordier diagram, for a maximum turbine total-to-static isentropic efficiency of 90 %, optimum values of 3.5 and 0.5 were obtained for the turbine specific diameter d_s and speed n_s, as similarly suggested by Whitfield and Baines (1990). The power turbine rotor tip diameter D_{pt} and rotational speed N_{pt} were estimated from the selected values of specific diameter and speed, using (Balje, 1981)

$$D_{pt} = \frac{d_s \sqrt{\dot{V}_5}}{(\mathrm{g}H_{ad})^{1/4}} \tag{3.2}$$

and

$$N_{pt} = \frac{60 n_s \, (\mathrm{g}H_{ad})^{3/4}}{2\pi \sqrt{\dot{V}_5}} \tag{3.3}$$

respectively, where $\dot{V}_5$ is the volume flow rate at the power turbine rotor outlet and $\mathrm{g} = 9.81$ m/s^2 is the standard acceleration of gravity. H_{ad} is the adiabatic

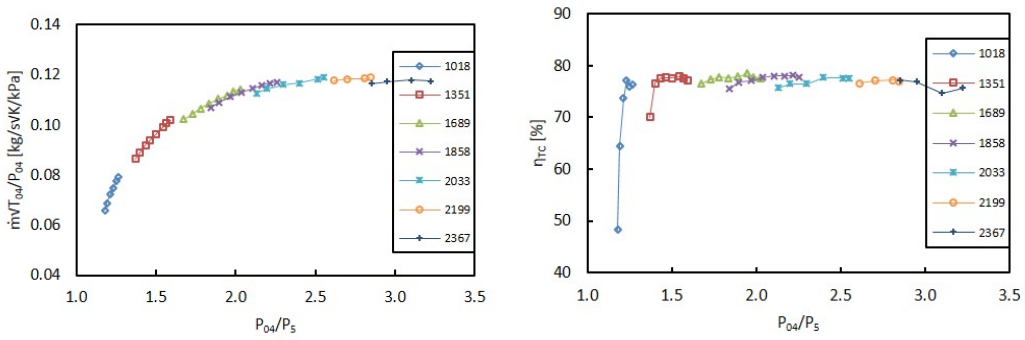

(a) **(b)**

Figure 3.5: Power turbine performance characteristics (Heuer, 2016); total-to-static pressure ratio vs (a) non-dimensional mass flow rate and (b) overall turbocharger efficiency

head, and was calculated from

$$H_{ad} = \frac{\gamma_g}{(\gamma_g - 1)\,\mathrm{g}} R \Delta T_{ad} \tag{3.4}$$

where $c_{p,g}$ and R are the mean specific heat at constant pressure and the molar gas constant of the expansion gases, respectively. The former was calculated using Equation 3.45. ΔT_{ad} is the isentropic temperature drop in the power turbine, and was calculated from

$$\Delta T_{ad} = T_{04}\left[1 - \left(\frac{1}{P_{04}/P_5}\right)^{(\gamma_g - 1)/\gamma_g}\right] \tag{3.5}$$

BorgWarner Turbo Systems similarly provided performance test data for the K44 turbocharger, and this test data was used to generate the power turbine performance characteristics. Similar to the gas-generator turbine, the performance characteristics plot the power turbine non-dimensional mass flow rate $\dot{m}\sqrt{T_{04}}/P_{04}$ and overall turbocharger efficiency η_{TC} against the total-to-static pressure ratio P_{04}/P_5, along each constant non-dimensional rotational speed line $N/\sqrt{T_{04}}$ (see Figure 3.5).

3.2.4 Solar field and receiver

The solar power plant was modeled based on a central receiver system, with the heliostat field based on Stellenbosch University's Helio100 test facility at Mariendahl. Helio100 has 102 modular and low cost heliostats, each with an aperture area of 2.2 m^2, corresponding to a total heliostat field aperture area A_{field} of 224.4 m^2. This test facility also has a tower with a height of 14 m (Helio100, 2017).

The Helio100 test facility currently has no pressurised air solar receiver. Similar to an approach taken by Heller *et al.* (2017), the pressurised air solar receiver in this study was based on the cluster of pressurised air solar receivers tested during the SOLGATE project. A linear correlation between the solar receiver thermal efficiency η_{rec} and the temperature of the pressurised air leaving the solar receiver T_{06} was obtained for the solar receiver cluster test data found in the SOLGATE Report (European Commission, 2005), as given below

$$\eta_{rec} = 1.19 - 0.0004T_{06} \tag{3.6}$$

This linear correlation (Equation 3.6) was used in combination with the estimated solar thermal energy collected from the solar field to estimate the temperature of the pressurised air leaving the solar receiver.

A pressure loss of 2 % of the compressor delivery pressure of 5.5 bar, at an estimated air mass flow rate of 0.7 kg/s and a solar receiver inlet air temperature of 300 °C, was also measured across the solar receiver cluster in the SOLGATE project (European Commission, 2005). These values were used as reference values in estimating the pressure loss across the solar receiver.

3.3 Solar resource

Direct normal irradiation (DNI) and ambient pressure and temperature data for the four selected solar days was downloaded from the Sonbesie weather station website (Sonbesie Weather Station, 2017). This weather station is installed at Stellenbosch University, and is in close proximity to the Helio100 test facility. The weather station uses a Kipp and Zonen (K&Z) CHP1 pyrheliometer to directly measure the DNI.

To estimate the solar thermal energy collected by the heliostat field $\dot{Q}_{sol}$, the optical efficiency of the heliostat field η_{opt} had to first be determined. Gauché *et al.* (2012) modeled the optical performance of a central receiver plant, but considered a surrounding heliostat field layout, since the optical performance for such a field layout simplifies to a function of only the solar zenith angle θ_z. A surrounding heliostat field layout would necessitate arranging the receiver modules around the center of the tower, to form a cylindrical aperture area (Heller *et al.*, 2017). Taking into consideration losses associated with heliostat reflectivity, soiling and availability, Gauché *et al.* derived the following sixth-order polynomial for the plant optical efficiency

$$\begin{aligned}\eta_{opt} = {} & 0.4245\theta_z^6 - 1.148\theta_z^5 + 0.3507\theta_z^4 + 0.755\theta_z^3 - 0.5918\theta_2^2 \\ & + 0.0816\theta_z + 0.832\end{aligned} \tag{3.7}$$

The solar zenith angle is the angle of the sun relative to vertical, and is a complement of the solar altitude angle α

$$\theta_z = 90 - \alpha \tag{3.8}$$

with the solar altitude angle defined as the angle between the central ray from the sun and a horizontal plane containing the observer, and it is calculated from the hour angle ω, declination angle δ and the latitude angle ϕ. Brief definitions of these angles, and the equations used to calculate them are provided below. More illustrative descriptions of these angles, and the derivation of the equations used to calculate them can be found in Stine and Geyer (2001).

The hour angle is the angle between the meridian parallel to the sun rays and the meridian containing the observer, and was given by

$$\omega = 15\,(t_s - 12) \tag{3.9}$$

where t_s is the solar time in hours, and was obtained using

$$t_s = LCT + \frac{EOT}{60} - LC - D \tag{3.10}$$

LCT is the local clock time, while EOT is the equation of time in minutes, and is the difference between mean solar time and true solar time for any given day. EOT was estimated using

$$EOT = 0.258\cos x - 7.416\sin x - 3.648\cos 2x - 9.228\sin 2x \tag{3.11}$$

where the angle x is a function of the day number N

$$x = \frac{360\,(N-1)}{365.242} \tag{3.12}$$

LC (in Equation 3.10) is a longitude correction in hours, and was given by

$$LC = \frac{L_{loc} - L_{st}}{15} \tag{3.13}$$

where L_{loc} is the longitude of the location of the heliostat field and L_{st} is the longitude on which the local standard time is based.

The parameter D in Equation 3.10 only applies to regions where daylight savings time is currently in effect, and is equal to 1 (hour), or zero otherwise.

The declination angle is the angle between the earth's equatorial plane and a line drawn between the center of the earth and the sun. It was calculated from the expression

$$\sin\delta = 0.39795\cos\left[0.98563\,(N-173)\right] \tag{3.14}$$

The latitude angle ϕ is the angle between a line drawn from a point on the earth's surface to the center of the earth, and the earth's equatorial plane. From the known hour angle, declination angle and latitude angle, the solar altitude angle was calculated, using the following expression

$$\sin\alpha = \sin\delta\sin\phi + \cos\delta\cos\omega\cos\phi \tag{3.15}$$

From the calculated solar altitude angle, the solar zenith angle was calculated (using Equation 3.8), and thereafter, the optical plant efficiency was calculated (using Equation 3.7). The solar thermal energy collected by the heliostat field was then calculated from the optical efficiency, the heliostat field aperture area A_{field} and the averaged DNI, using

$$\dot{Q}_{sol} = \eta_{opt} A_{field} DNI \tag{3.16}$$

A fraction of the solar thermal energy that is collected by the heliostat field and reflected onto the solar receiver is absorbed into the pressurised air passing through the solar receiver. The absorbed solar thermal energy raises the temperature of the pressurised air. To determine the temperature of the pressurised air leaving the solar receiver, the solar receiver efficiency was first alternatively defined as the ratio of the solar thermal energy absorbed into the pressurised air flowing through the solar receiver $\dot{Q}_{rec}$ to that collected by the heliostat field

$$\eta_{rec} = \frac{\dot{Q}_{rec}}{\dot{Q}_{sol}} \tag{3.17}$$

where

$$\dot{Q}_{rec} = \dot{m}_a c_{p,a} \left(T_{06} - T_{02}\right) \tag{3.18}$$

Equating Equations 3.6 and 3.17, and substituting for $\dot{Q}_{rec}$ (using Equation 3.18), T_{06} was then determined from the following resulting expression

$$T_{06} = \frac{1.19\dot{Q}_{sol} + \dot{m}_a c_{p,a} T_{02}}{0.0004\dot{Q}_{sol} + \dot{m}_a c_{p,a}} \tag{3.19}$$

where $c_{p,a}$ is the mean ideal-gas specific heat at constant pressure of the air stream passing through the solar receiver. $c_{p,a}$ was calculated (in kJ/kmolK) using the following third-order polynomial approximation suggested by Cengel and Boles (2011)

$$c_{p,a} = -1.966 \times 10^{-9} T^3 + 0.4802 \times 10^{-5} T^2 + 0.1967 \times 10^{-2} T + 28.11 \tag{3.20}$$

where T is the mean stagnation temperature of the pressurised air stream passing through the solar receiver, and was calculated as the mean of the compressor outlet/receiver inlet air stagnation temperature and the receiver outlet air stagnation temperature. The calculation of $c_{p,a}$ followed an iterative process that required guessing an initial value of $c_{p,a}$, calculating T_{06}, then taking the new T_{06} and calculating a more accurate mean value of $c_{p,a}$.

The modeling of the solar resource implemented a temperature control loop that ensured that the receiver outlet temperature never exceeded the desired equilibrium running gas-generator TIT, as would be the case in a practical solar-hybrid MGT system.

3.4 MGT system component matching

The MGT system component matching used component models or actual performance characteristics of the individual MGT components to predict the possible operating range of the MGT system under both standard and solar-hybrid operation. According to Saravanamuttoo *et al.* (2009), the range of possible operating conditions for each individual gas turbine component reduces significantly, when the components are linked together in an engine. The challenge therefore, is to find corresponding operating points on the performance characteristics of each component when the engine is running at a steady speed, or in equilibrium. The obtained equilibrium running points for a series of speeds can then be plotted on the compressor characteristic, and joined, to generate an equilibrium running line. Thereafter, MGT system performance parameters such as the TIT, useful work output, specific fuel consumption and cycle thermal efficiency, corresponding to the obtained equilibrium running points can easily be obtained.

The MGT system component matching procedure followed an interactive nested loop approach adapted from Saravanamuttoo *et al.* (2009). In this approach, equilibrium running/matching calculations manipulate component performance characteristics – in the form of non-dimensional identities – to achieve compatibility of mass flow, work and rotational speed between the individual MGT components linked together in an engine. The nested loop approach was chosen, because firstly, it gives a clear insight into the overall matching procedure, and secondly, it is relatively easy to implement in a computer program for simple engines such as the twin-shaft MGT (Saravanamuttoo *et al.*, 2009; Walsh and Fletcher, 2004).

The MGT system component matching equations are described as follows: since the gas-generator compressor and turbine are directly coupled together, compatibility of rotational speed between corresponding compressor and turbine operating points required that

$$\frac{N}{\sqrt{T_{03}}} = \frac{N}{\sqrt{T_{01}}} \times \sqrt{\frac{T_{01}}{T_{03}}} \tag{3.21}$$

The mass flow through the gas-generator turbine is the sum of that through the coupled compressor, and the added fuel. Because the fuel mass flow was not known at this stage of the component matching, it was assumed that the mass flow through the gas-generator compressor was equal to that through the coupled turbine. In practice, the fuel mass flow is only 1 to 2 % of the air mass flow, and can therefore be ignored at this stage, without much loss of accuracy. Compatibility of mass flow between corresponding gas-generator compressor and turbine operating points required that

$$\frac{\dot{m}\sqrt{T_{03}}}{P_{03}} = \frac{\dot{m}\sqrt{T_{01}}}{P_{01}} \times \frac{P_{01}}{P_{02}} \times \frac{P_{02}}{P_{03}} \times \sqrt{\frac{T_{03}}{T_{01}}} \tag{3.22}$$

where the pressure ratio P_{02}/P_{03} was determined directly from the non-dimensional pressure loss across the combustion chamber $\Delta P_{comb}/P_{02}$ (calculated using Equation 3.1, and non-dimensionalised by the compressor delivery pressure P_{02}). For the standard MGT system with no solar thermal energy input

$$\frac{P_{03}}{P_{02}} = 1 - \frac{\Delta P_{comb}}{P_{02}} \tag{3.23}$$

while for the solar-hybrid MGT system, the additional non-dimensional pressure loss across the solar receiver $\Delta P_{rec}/P_{02}$ had to also be considered, and P_{02}/P_{03} was determined from

$$\frac{P_{03}}{P_{02}} = 1 - \frac{\Delta P_{rec}}{P_{02}} - \frac{\Delta P_{comb}}{P_{02}} \tag{3.24}$$

The variation in the non-dimensional pressure loss across the solar receiver with changing operating conditions was estimated using

$$\frac{\Delta P_{rec}}{P_{02}} = \left(\frac{\Delta P_0}{P_0}\right)\left[\left(\frac{\dot{m}_a\sqrt{T_{02}}}{P_{02}}\right)\Big/\left(\frac{\dot{m}_0\sqrt{T_0}}{P_0}\right)\right]^2 \tag{3.25}$$

where the terms $(\Delta P_0/P_0)$ and $\left(\dot{m}_0\sqrt{T_0}/P_0\right)$ were calculated based on the reference values measured during the SOLGATE project.

The modeling implemented a bypass of the solar receiver during periods of no solar insolation, to ensure that the receiver did not impose a parasitic pressure loss on the cycle when it was not in use. The bypass of the solar receiver was achieved through setting the stagnation pressure at the combustion chamber inlet equal to that at the compressor outlet, for periods of no solar thermal energy input.

The gas-generator turbine has to meet the work requirement of the coupled compressor. The compressor work requirement is expressed as

$$\dot{W}_c = \dot{m}c_{p,a}\Delta T_{012} \tag{3.26}$$

while the work output of the coupled gas-generator turbine is expressed as

$$\dot{W}_t = \eta_{mech}\dot{m}c_{p,g}\Delta T_{034} \tag{3.27}$$

Matching of the work requirement of the gas-generator compressor, to the work output of the coupled gas-generator turbine, for corresponding gas-generator compressor and turbine operating points required that

$$\dot{m}c_{p,a}\Delta T_{012} = \eta_{mech}\dot{m}c_{p,g}\Delta T_{034}$$

and rewriting in non-dimensional terms

$$\frac{\Delta T_{034}}{T_{03}} = \frac{c_{p,a}}{\eta_{mech}c_{p,g}} \times \frac{\Delta T_{012}}{T_{01}} \times \frac{T_{01}}{T_{03}} \tag{3.28}$$

where ΔT_{012} is the temperature rise in the compressor, and was calculated from

$$\Delta T_{012} = \frac{T_{01}}{\eta_{c,t-t}} \left[\left(\frac{P_{02}}{P_{01}} \right)^{(\gamma_a - 1)/\gamma_a} - 1 \right] \tag{3.29}$$

and γ_a is the specific heat ratio of air. The heat ratio was calculated through an iterative process that entailed guessing an initial value of γ_a, calculating ΔT_{012} and $c_{p,a}$, then taking the new $c_{p,a}$ and calculating a more accurate mean value of γ_a. The new value of γ_a was then used to calculate new and more accurate values of ΔT_{012} and $c_{p,a}$. ΔT_{034} is the temperature drop in the gas-generator turbine, and is the difference between the gas-generator turbine's inlet and outlet stagnation temperatures – the latter calculated from the static temperature at the gas-generator turbine outlet (power turbine inlet) T_4. The static isentropic temperature at the gas-generator turbine outlet T_{4s} was calculated from the known gas-generator turbine pressure ratio and inlet temperature values, using the ideal-gas isentropic relation between pressure and temperature ratios

$$T_{4s} = T_{03} \left(\frac{1}{P_{03}/P_4} \right)^{(\gamma_g - 1)/\gamma_g} \tag{3.30}$$

where γ_g is the specific heat ratio of the expansion gases, and was similarly calculated through an iterative process that entailed guessing an initial value of γ_g, calculating T_{4s}, then taking the new T_{4s} and calculating a more accurate mean value of γ_g. The new γ_g was used to calculate a new value of T_{4s} which was then substituted into Equation 3.31, including the known values of $\eta_{t,t-s}$ and T_{03}, to obtain T_4

$$T_4 = T_{03} - \eta_{t,t-s} \left(T_{03} - T_{4s} \right) \tag{3.31}$$

The stagnation temperature at the outlet of the gas-generator turbine T_{04} was then calculated from

$$T_{04} = T_4 + \frac{V_4^2}{2c_{p,g}} \tag{3.32}$$

where V_4 is the gas stream velocity at the outlet of the gas-generator turbine, and was calculated using

$$V_4 = \frac{\dot{m} R T_4}{P_4 \pi d_4^2 / 4} \tag{3.33}$$

R is the molar gas constant and d_4 is the pipe diameter at the gas-generator turbine's outlet.

The gas generator was matched to the power turbine based on the fact that the mass flow leaving the gas generator must equal that at the entry of the power turbine, and that the pressure ratio available to the power turbine is fixed by the gas-generator compressor and turbine pressure ratios.

Compatibility of mass flow between the gas generator and the power turbine required that

$$\frac{\dot{m}\sqrt{T_{04}}}{P_{04}} = \frac{\dot{m}\sqrt{T_{03}}}{P_{03}} \times \frac{P_{03}}{P_{04}} \times \sqrt{\frac{T_{04}}{T_{03}}} \tag{3.34}$$

while the corresponding pressure ratio across the power turbine was given by

$$\frac{P_{04}}{P_a} = \frac{P_{02}}{P_{01}} \times \frac{P_{03}}{P_{02}} \times \frac{P_{04}}{P_{03}} \tag{3.35}$$

where the stagnation pressure at the gas-generator turbine outlet P_{04} was determined from the calculated values of T_4 and T_{04}, using the ideal-gas isentropic relation between pressure and temperature ratios

$$P_{04} = P_4 \left(\frac{T_{04}}{T_4}\right)^{\gamma_g/(\gamma_g - 1)} \tag{3.36}$$

Through inspection of the main matching Equations (3.21, 3.22 and 3.28), it is observed that the temperature ratio T_{03}/T_{01} is a common parameter in all three equations. This ratio was therefore used as the convergence parameter in the matching procedure.

The component matching procedure entailed guessing a value of T_{03}/T_{01} and for each constant compressor non-dimensional speed line, selecting a compressor operating point, and determining the corresponding gas-generator turbine operating point. From the obtained gas-generator turbine operating point, a new value of T_{03}/T_{01} was then calculated (using Equation 3.28), and compared to the guessed value, with agreement signifying that matching of the obtained gas-generator turbine operating point with the selected compressor operating point had been achieved, for the guessed value of T_{03}/T_{01}. The gas-generator TIT was then determined from the product of the matching T_{03}/T_{01} and the known ambient temperature T_{01}.

A final temperature ratio range of 2.5 to 4.2, in increments of 0.001, was used for the temperature ratio iteration. This temperature ratio range was obtained from an analysis of the initial results from the component matching. The upper limit corresponded to a gas-generator TIT of 930 °C. BorgWarner Turbo Systems specify a maximum continuous TIT of 950 °C for most of their turbochargers (BorgWarner, 2017).

To terminate the matching for each constant compressor non-dimensional speed line, the difference between the guessed and the iterated value of T_{03}/T_{01} had to be less than 0.001.

3.5 Combustion analysis

During periods of insufficient or no solar irradiation, fuel has to be combusted to raise the temperature of the pressurised air stream to the desired equilibrium

running gas-generator TIT. The MGT system was assumed to run on propane, which has a lower heating value (LHV) of 46.34 MJ/kg. Propane was chosen because of its relatively high boiling point (which makes it easy to handle), its good thermal stability and its clean combustion.

The mass flow rate of propane was determined through performing an analysis of the chemical reaction that takes place in the combustion chamber. Assuming complete combustion of propane with excess air, and applying the first-law analysis, the chemical equation of the combustion reaction was rewritten as

$$\dot{x}\overline{h}_{C_3H_8} + \dot{y}\left[\overline{h}_{O_2} + 3.76\overline{h}_{N_2}\right]_r = 3\dot{x}\overline{h}_{CO_2} + 4\dot{x}\overline{h}_{H_2O} + (\dot{y} - 5\dot{x})\left[\overline{h}_{O_2}\right]_p + \dot{y}\left[3.76\overline{h}_{N_2}\right]_p \tag{3.37}$$

where $\dot{x}$ and $\dot{y}$ are the molar mass flow rates of propane and air, respectively. $\dot{y}$ was calculated from the air mass flow rate corresponding to the selected compressor operating point, the number of moles of air taking part in the chemical reaction (1 kmol of oxygen + 3.76 kmol of nitrogen = 4.76 kmol of air) and the molar mass M of air, using the expression

$$\dot{y} = \frac{\dot{m}_a}{4.76M} \tag{3.38}$$

while $\dot{x}$ was calculated from the following expression, derived through rearranging Equation 3.37, and substituting for $\dot{y}$ (using Equation 3.38)

$$\dot{x} = \frac{\dot{m}_a}{4.76M}\left[\frac{\left[\overline{h}_{O_2}\right]_p - \left[\overline{h}_{O_2}\right]_r - \left[3.76\overline{h}_{N_2}\right]_r + \left[3.76\overline{h}_{N_2}\right]_p}{\overline{h}_{C_3H_8} - 3\overline{h}_{CO_2} - 4\overline{h}_{H_2O} + 5\left[\overline{h}_{O_2}\right]_p}\right] \tag{3.39}$$

$\overline{h}$ denotes the enthalpy of a reactant r or a product p, and was given by

$$\overline{h} = \overline{h}^0_f + \left(\overline{h}_T - \overline{h}^0\right) \tag{3.40}$$

where $\overline{h}^0_f$ is the enthalpy of formation of a reactant or product at the standard reference state (25 °C and 1 atm) and the term in the parentheses is the sensible enthalpy of the reactant or product relative to the standard reference state, and was given by the difference between the sensible enthalpy of the reactant or product at the specified state $\overline{h}_T$, and the sensible enthalpy of the reactant or product at the standard reference state $\overline{h}^0$.

Assuming the reactants and combustion products are ideal gases, the values of enthalpy at the specified states for the reactants and products were then interpolated from ideal-gas property tables provided by Cengel and Boles (2011). For the reactants, propane was assumed to be at the standard reference state, while the air was either at the compressor outlet temperature, for standard MGT operation or at the solar receiver outlet temperature, during solar-hybrid operation. The combustion products were assumed to be at the desired gas-generator TIT.

It has to be noted that the enthalpies of formation of the reactants and the combustion products at the specified states are slightly lower than those at the standard reference state.

The ideal mass flow rate of propane $\dot{m}_{f,id}$ was thereafter determined from the product of the determined molar mass flow rate of propane and the molar mass of propane, using

$$\dot{m}_{f,id} = \dot{x}M \tag{3.41}$$

with the actual mass flow rate of propane m_f then determined from the calculated ideal mass flow rate of propane and an assumed combustion efficiency η_{comb} of 95 %, using

$$\dot{m}_f = \frac{\dot{m}_{f,id}}{\eta_{comb}} \tag{3.42}$$

The fuel/air ratio f was then given by

$$f = \frac{\dot{m}_f}{\dot{m}_a} \tag{3.43}$$

3.6 Working fluid properties

The values of the properties c_p and γ of the working fluid vary throughout the cycle, due to changes of temperature and, with internal combustion, due to changes in chemical composition. These properties are useful in the estimation of the cycle performance, and it is necessary to take account of variations in the values of the properties, due to changing conditions throughout the cycle (Saravanamuttoo *et al.*, 2009).

Normally, c_p is a function of temperature alone, for ideal gases over the typical working ranges of pressure and temperature (Cengel and Boles, 2011). The same applies to γ, given it is related to c_p by the expression

$$\gamma = \frac{c_p}{c_p - R} \tag{3.44}$$

The working fluid during the MGT system compression process is air, and the mean ideal-gas values of c_p, corresponding to the selected compressor operating points were calculated using Equation 3.20, where T is the mean stagnation temperature of the pressurised air, and was calculated as the mean of the compressor inlet and outlet air stagnation temperatures.

On the other hand, the working fluid during the solar-hybrid MGT system expansion processes in the gas-generator and the power turbine is a mixture of combustion gases. Given the composition of the fuel, and the fuel/air ratio used, a method for estimating the properties of the products of complete combustion of a general fuel in a general medium can be found in Fielding and Topps (1959), as suggested by Saravanamuttoo *et al.* (2009). The proposed method develops equations for the difference between a property of a gas mixture and the corresponding property of air.

According to Fielding and Topps, the composition of products of complete combustion of a general fuel in a general medium are dependent only on the fuel and medium composition and fuel/medium ratio. The chemical structure and physical state of the fuel and medium have no effect on product composition since differing chemical combinations of the same basic components give identical products on complete combustion. For instance, all hydrocarbons may be considered simply as hydrogen and carbon irrespective of the chemical or physical form of the hydrocarbon. This technique considerably simplifies the determination of general combustion product properties.

Assuming complete combustion of propane in dry air, and knowing the composition of propane and its combustion products, the specific heat for the mixture of combustion gases $c_{p,g}$ was calculated using

$$c_{p,g} = c_{p,a} + \frac{f}{1+f}\left(\overline{C}_f\theta_C + \overline{H}_f\theta_H\right) \tag{3.45}$$

where $c_{p,a}$ is the mean ideal-gas specific heat of dry air (calculated using Equation 3.20), f is the fuel/air ratio, $\overline{C}_f$ and $\overline{H}_f$ are the carbon and hydrogen content of propane by mass and θ_C and θ_H are the carbon and hydrogen theta functions for mean specific heat at a specified temperature, and were calculated using

$$\theta_C = 3.6645c_{p,CO_2} - 2.6645c_{p,O_2} - c_{p,a} \tag{3.46}$$

and

$$\theta_H = 8.9365c_{p,H_2O} - 7.9365c_{p,O_2} - c_{p,a} \tag{3.47}$$

where c_{p,CO_2}, c_{p,O_2} and c_{p,H_2O} are the mean ideal-gas specific heats at constant pressure of carbon dioxide, oxygen and water vapor, and were calculated (in kJ/kmolK) using the following third-order polynomial approximations suggested by Cengel and Boles (2011)

$$c_{p,CO_2} = 7.469 \times 10^{-9}T^3 - 3.501 \times 10^{-5}T^2 + 5.981 \times 10^{-2}T + 22.26 \tag{3.48}$$

$$c_{p,O_2} = 1.312 \times 10^{-9}T^3 - 0.7155 \times 10^{-5}T^2 + 1.520 \times 10^{-2}T + 25.48 \tag{3.49}$$

$$c_{p,H_2O} = -3.595 \times 10^{-9}T^3 + 1.055 \times 10^{-5}T^2 + 0.1923 \times 10^{-2}T + 32.24 \tag{3.50}$$

where T is the desired gas-generator TIT.

During periods of solar-only operation, there is no requirement for additional combustion of fuel, and the working fluid for the MGT expansion process is hot air. For this case and similar to the compression process, the mean values of c_p were calculated using Equation 3.20.

The amount of heat released when a fuel is burned completely in a steady-flow process and the products are returned to the standard temperature (25 °C) of the reactants is referred to as the enthalpy of combustion or heating (calorific) value of a fuel. For gas turbine performance calculations, the most desirable calorific value of fuel is the lower heating value (LHV) or net calorific value at constant pressure (ASME PTC 22, 2014; Fielding and Topps, 1959).

However, the enthalpy of combustion for any given fuel is different at different temperatures and pressures (Cengel and Boles, 2011). According to Fielding and Topps, the calorific value of a fuel at any given temperature, also known as the effective calorific value at a specified temperature $E.C.V_T$, depends on both the constant-pressure net calorific value of the fuel at the standard temperature and the fuel composition. For a steady-flow complete combustion process of propane in dry air, the effective calorific value of propane at the desired gas-generator TIT T_{03} was calculated using (Fielding and Topps, 1959)

$$E.C.V_T = H - \left[\overline{h}_a\right]_{298.15\ \mathrm{K}}^{T_{03}} - \overline{C}_f\theta_C - \overline{H}_f\theta_H \tag{3.51}$$

where H is the constant-pressure net calorific value of propane at 25 °C, and $\left[\overline{h}_a\right]_{298.15\ \mathrm{K}}^{T_{03}}$ is the change in enthalpy of dry air due to a change of temperature from 298.15 K (25 °C) to the desired gas-generator TIT, and was given by

$$\left[\overline{h}_a\right]_{298.15\ \mathrm{K}}^{T_{03}} = \overline{h}_{a(T_{03})} - \overline{h}_{a(298.15\ \mathrm{K})} \tag{3.52}$$

The terms $\overline{C}_f$ and $\overline{H}_f$ are as previously described, while θ_C and θ_H are the carbon and hydrogen theta functions for effective calorific value at the desired gas-generator TIT, and were given by

$$\theta_C = 3.6645\overline{h}_{CO_2} - 2.6645\overline{h}_{O_2} - \overline{h}_a \tag{3.53}$$

and

$$\theta_H = 8.9365\overline{h}_{H_2O} - 7.9365\overline{h}_{O_2} - \overline{h}_a \tag{3.54}$$

The enthalpy values (in kJ/kmol) for air $\overline{h}_a$, carbon dioxide $\overline{h}_{CO_2}$, oxygen $\overline{h}_{O_2}$ and water vapor $\overline{h}_{H_2O}$ were interpolated from ideal-gas property tables provided by Cengel and Boles (2011).

The total cycle thermal energy input $\dot{Q}_{th}$ for the MGT under standard operation was then calculated using

$$\dot{Q}_{th} = \dot{m}_f E.C.V_T \tag{3.55}$$

while that for the MGT under solar-hybrid operation was given by

$$\dot{Q}_{th} = \dot{m}_f E.C.V_T + \dot{Q}_{rec} \tag{3.56}$$

with the solar share – defined as the ratio of the solar thermal energy absorbed into the pressurised air to the total cycle thermal energy input – then given by

$$solarshare = \frac{\dot{Q}_{rec}}{\dot{Q}_{th}} \tag{3.57}$$

The useful work output from the power turbine $\dot{W}_{pt}$ was then estimated from the temperature drop in the power turbine ΔT_{045} and an assumed turbine-output mechanical efficiency η_{mech} of 99 %, using

$$\dot{W}_{pt} = \eta_{mech}\dot{m}c_{p,g}\Delta T_{045} \tag{3.58}$$

The MGT system specific fuel consumption SFC in kg/kWh was calculated using

$$SFC = \frac{3600\dot{m}_f}{\dot{W}_{pt}} \tag{3.59}$$

The cycle thermal efficiency η_{th} was determined from the ratio of the power turbine useful work output to the total cycle thermal energy input

$$\eta_{th} = \frac{\dot{W}_{pt}}{\dot{Q}_{th}} \tag{3.60}$$

The modeling approach for the MGT system under solar-hybrid operation is summarised in the flow chart shown in Figure 3.6.

3.7 Recuperation

MGT systems in the power output range of 5 to 20 kW are typically characterised by low pressure ratios in the range of 2 to 3, and consequently low cycle thermal efficiencies in the range of 7 to 13 % (Córdova *et al.*, 2015). To improve the low cycle thermal efficiencies, these systems normally incorporate recuperation.

As shown on the T-s diagram (Figure 3.2), the temperature of the exhaust gases leaving the power turbine T_{05} is higher than that of the pressurised air leaving the compressor T_{02}. A heat exchanger can therefore be fitted between the compressor and the solar receiver, to recover the thermal energy contained in the exhaust gases leaving the power turbine, and reduce the requirement for combustion. Reduction in the combustion requirement consequently increases the cycle thermal efficiency.

Similar to the approach taken by Córdova *et al.*, the cycle thermal efficiency that could be achieved through adding recuperation to the MGT system under solar-hybrid operation was estimated using

$$\eta_{th,R} = \frac{\dot{W}_{pt}}{\dot{Q}_{th} - \dot{Q}_R} \tag{3.61}$$

where $\dot{Q}_R$ is the actual thermal energy recovered in the recuperator, and was calculated from the expression

$$\varepsilon_R = \frac{\dot{Q}_R}{\dot{Q}_{R,max}} \tag{3.62}$$

The term ε_R in Equation 3.62 is the recuperator effectiveness while $\dot{Q}_{R,max}$ is the maximum theoretical thermal energy that could be recovered in the recuperator. A recuperator effectiveness of 92 % was assumed for this study, as experimentally determined by Córdova *et al.*. The maximum theoretical

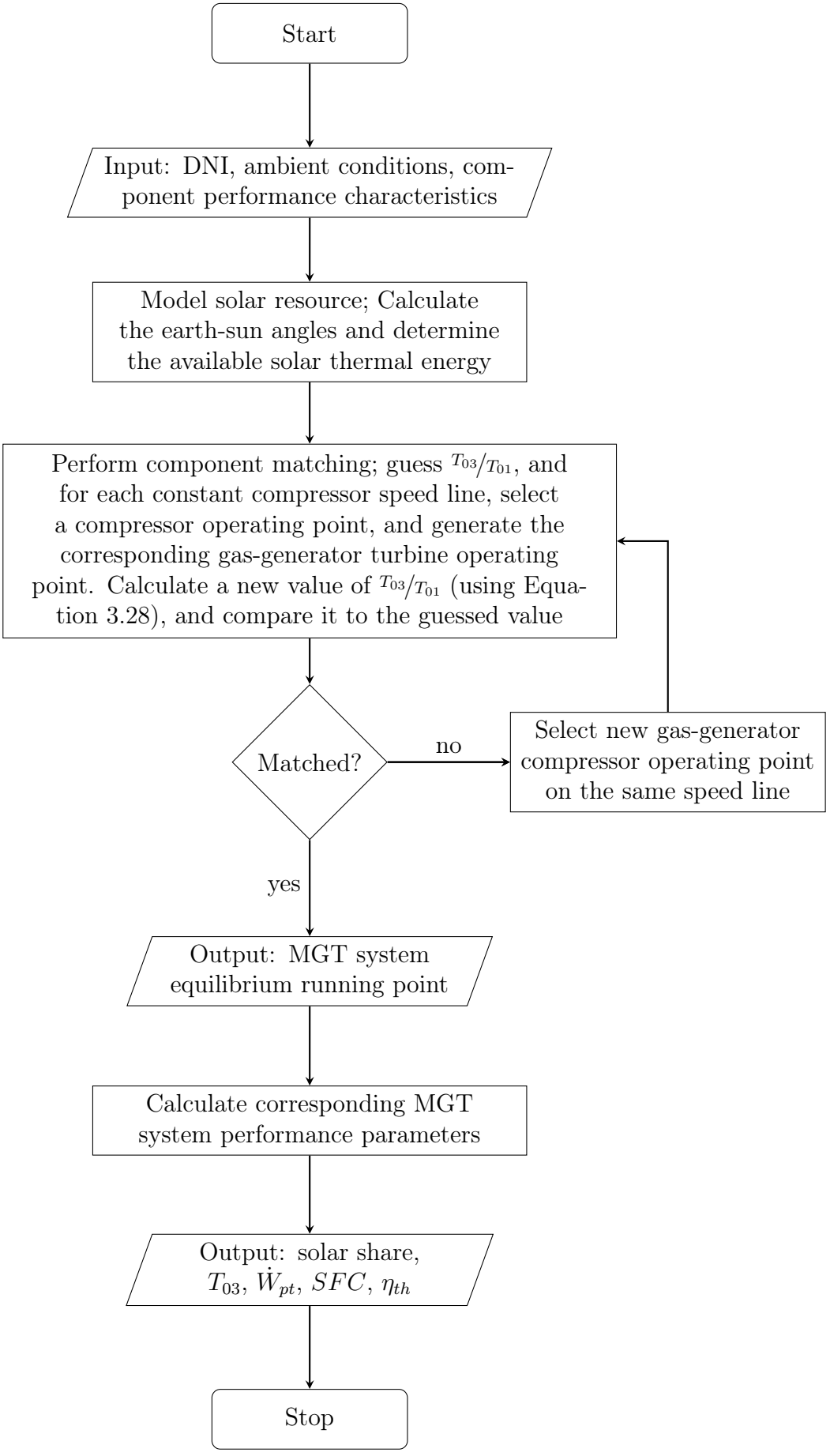

Figure 3.6: Summary of the modeling approach

thermal energy that could be recovered through recuperation was calculated from

$$\dot{Q}_{R,max} = \dot{m}_a c_{p,a} \left(T_{05} - T_{02}\right) \tag{3.63}$$

This simplified approach showed the potential for increasing the cycle thermal efficiency, when recuperation is considered, without taking into account the geometry of the recuperator. This approach though ignores the additional pressure losses that result from incorporating an additional component in the flow path between the gas-generator compressor and turbine, and the adverse effect that these pressure losses have on the useful MGT system work output.

3.8 Transient modeling

A thorough understanding of the dynamic behaviour of the MGT system is essential for the development and implementation of suitable control systems/strategies for solar-hybrid MGT systems. During transient operation, the gas turbine control system must ensure that the critical operating limits of rotor speed and TIT are never exceeded, and that compressor surge is avoided (Saravanamuttoo *et al.*, 2009).

The transient response of the solar-hybrid MGT system following a sudden change in the solar irradiation/solar thermal energy input and load can be critical to its safe operation. A sudden increase or decrease in the solar thermal energy input can lead to a sudden acceleration or deceleration of the solar-hybrid MGT system, the former potentially leading to compressor surge. The solar receiver and its ducting system also increase the thermal inertia and the pressurised air volume in a MGT system under solar-hybrid operation. Critical situations, such as abrupt load shedding and emergency shutdowns, while the MGT system is operating at maximum solar thermal energy input and load, can result in a high amount of solar thermal energy entering the MGT system and accelerating it, potentially beyond the maximum acceptable rotor over-speed limit.

The acceleration or deceleration of the MGT system, due to the sudden change in the solar thermal energy input is typically corrected by altering the fuel mass flow rate, using a suitable fast acting fuel flow control valve. On the other hand, safety measures, such as the use of fast acting air flow control and blow-off valves, mechanical brakes and shunt resistors loading the generator, have been suggested in literature, as suitable control measures against the rotor over-speed that results from the high thermal inertia and additional volume existing in the MGT system during load shedding or emergency shutdowns.

Studies such as Felsmann *et al.* (2014, 2015) and Kathirgamanathan and Axelsson (2018) modeled in detail the effect of flow control and blow-off valve response rates on rotor over speed, and further suggest the maximum acceptable response time to safely mitigate against rotor over-speed during load-shedding and emergency shut down. This study rather focused on modeling

the transient response of the MGT system to sudden changes in solar irradiation/solar thermal energy input during the four selected solar days, for the proposed MGT system control strategy of operating at the determined solar-hybrid equilibrium running point.

Similar to Kathirgamanathan and Axelsson, the transient modeling followed a quasi-steady-state approach.

The fuel mass flow rate necessary to accelerate or decelerate the solar-hybrid MGT system, in order to maintain it operating at the determined solar-hybrid equilibrium running point, the resultant gas-generator TIT and rotational speed and the useful work output were calculated for each minute of MGT system solar-hybrid operation, during hours of sufficient solar irradiation.

The critical TIT limit was the OEM specified maximum continuous turbocharger TIT of 950 °C. The temperature ratio range used for the component matching ensured this temperature limit was never exceeded. Therefore, the only critical transient operating parameter that needed to be monitored was the gas-generator rotational speed.

The simplified approach adopted for the transient modeling cannot capture the full transient effects of the additional thermal inertia and pressurised air volume in solar-hybrid MGT system components, such as the solar receiver, recuperator, and their connecting ducts, during critical situations, such as abrupt load shedding and emergency shutdowns. But as a first iteration, it should be able to illustrate the main control system corrective action of altering the fuel flow, in response to sudden (minute averaged) changes in solar irradiation, without requiring knowledge of the geometry of the physical solar-hybrid MGT system – given this information was not available during this (theoretical modeling) stage of the study. In addition, the turbo-lag in small gas turbine systems based on turbochargers sized for truck engines should be much shorter than the one-minute time steps of the solar thermal energy input, further justifying the quasi-steady-state approach.

A thorough transient analysis of the MGT system under solar-hybrid operation has to take into account the geometry of the physical solar-hybrid MGT system. Knowledge of the response rates of control system components, such as flow control and blow-off valves, is also required.

3.9 Modeling results and analysis

3.9.1 MGT system equilibrium running points

From the matching of the individual MGT system components, equilibrium running (operating) points for both standard and solar-hybrid MGT system operation – denoted by MGT and SHMGT, respectively – were obtained, and plotted on the compressor performance characteristic (see Figure 3.7).

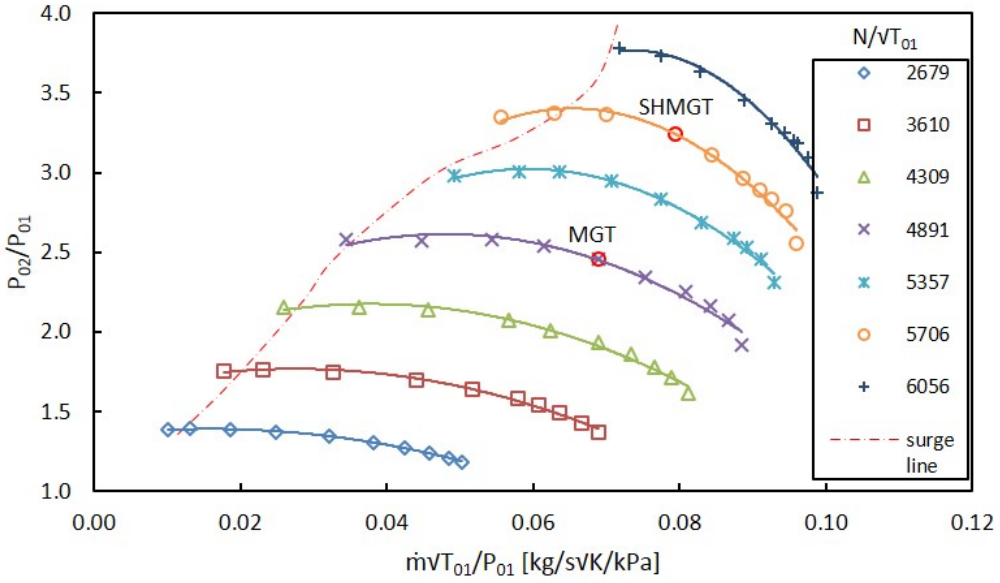

Figure 3.7: MGT system equilibrium running points

Table 3.1: MGT system equilibrium running point characteristics

Parameter	Value	
	MGT	SHMGT
P_{02}/P_{01}	2.5	3.2
$\dot{m}\sqrt{T_{01}}/P_{01}$ [kg/s$\sqrt{\text{K}}$/kPa]	0.0690	0.0795
$\eta_{c,t-t}$ [%]	78	77
$N/\sqrt{T_{01}}$ [rpm/$\sqrt{K}$]	4891	5706

The equilibrium running point for the MGT system under standard operation lies on the 4891 non-dimensional compressor speed line, while that for the MGT system under solar-hybrid operation lies on the 5706 non-dimensional compressor speed line. Addition of solar thermal energy to the MGT system shifted the operating point of the MGT system to a region of higher compressor pressure ratio, non-dimensional speed and non-dimensional mass flow rate (see Table 3.1). The shift of the solar-hybrid MGT system equilibrium running point was to counter the additional system pressure losses introduced by the solar receiver and the solar thermal energy input into the pressurised air, and ensure the compressor work requirement is met by the coupled gas-generator turbine, while also maintaining a useful work output from the power turbine.

Figure 3.7 shows a reduced surge margin – defined as the difference between a mass flow rate on the operating line at a certain non-dimensional speed and the corresponding mass flow rate on the surge line at the same speed, expressed as a percentage of the mass flow rate on the operating line (Brun and

Nored, 2009) – for the MGT system operating at the determined solar-hybrid equilibrium point, in comparison to that of the MGT system under standard operation. A surge margin of 21 % was calculated for solar-hybrid operation, in contrast to the 50 % calculated for standard MGT system operation.

The minimum acceptable compressor surge margin is dependent on the system configuration and application requirements, since the worst operating conditions and transient requirements vary with each application (Walsh and Fletcher, 2004). Nevertheless, for power and propulsion applications, a surge margin of 15 to 20 % is typically expected (Dixon and Hall, 2010; Walsh and Fletcher, 2004).

It is noted though that, the stable operating region for the K31 turbocharger is narrower at high compressor speeds, given the shift of the surge line to the right (see Figure 3.7).

3.9.2 Standard MGT system performance

The performance of the MGT system under standard operation was analysed through studying the effect of changing ambient temperature and pressure conditions – over the course of the two selected solar days – on the performance of the MGT system, for the obtained MGT system equilibrium running point.

As expected, the gas-generator TIT increased linearly with ambient temperature (see Figure 3.8). The temperature ratio T_{03}/T_{01} decreases with increasing ambient temperature. Since the gas-generator TIT is given by $(T_{03}/T_{01})\,T_{01}$, the decrease in T_{03}/T_{01} is more than offset by the increase in T_{01}, which results in an increase in the gas-generator TIT.

Notably though, the linear relation between the gas-generator TIT and ambient temperature, during standard operation is in contrast to that observed for solar-hybrid operation, as will later be shown (see Figure 3.15).

The predicted air mass flow rate through the MGT system decreased with increasing ambient temperature, since the air mass flow rate was determined from the compressor non-dimensional mass flow rate for the obtained equilibrium running point, using $\left(\dot{m}\sqrt{T_{01}}/P_{01}\right)/\left(\sqrt{T_{01}}/P_{01}\right)$. Consequently, operating at higher ambient temperature resulted in lower work output, since the work output is proportional to the air mass flow rate through the MGT system. On the other hand, operating at higher ambient pressure resulted in an increase in the predicted air mass flow through the MGT system, consequently resulting in higher work output.

The predicted MGT system work output during the course of the two selected days is shown in Figure 3.9. A higher work output was predicted for the cooler (winter) solar day, since lower ambient temperature and higher ambient pressure values were measured for this day, in comparison to the warmer (summer) solar day. The nearly linear trend for the predicted work output during standard operation was also in contrast to that predicted for solar-hybrid operation, as will later be shown (see Figure 3.14).

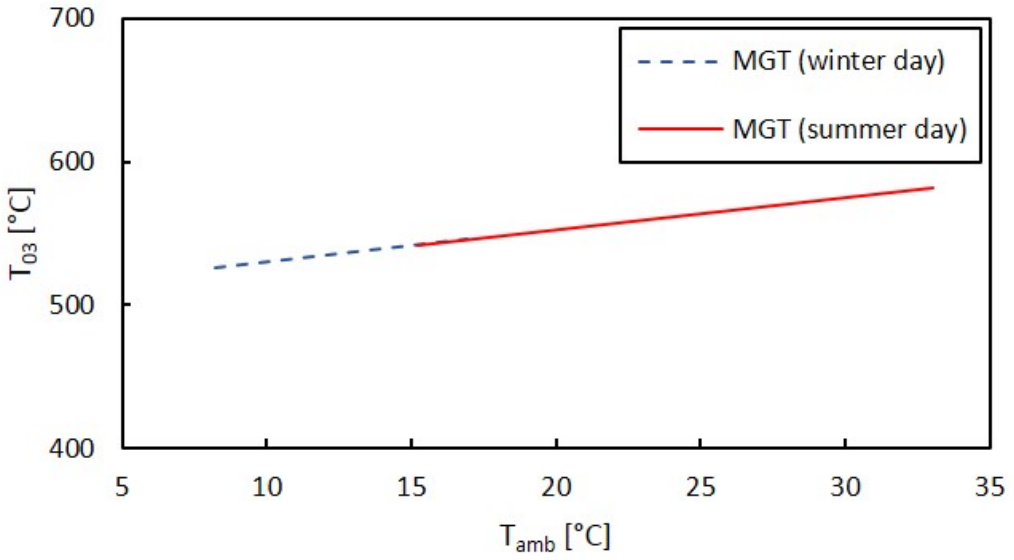

Figure 3.8: Effect of ambient temperature on the gas-generator TIT under standard operation

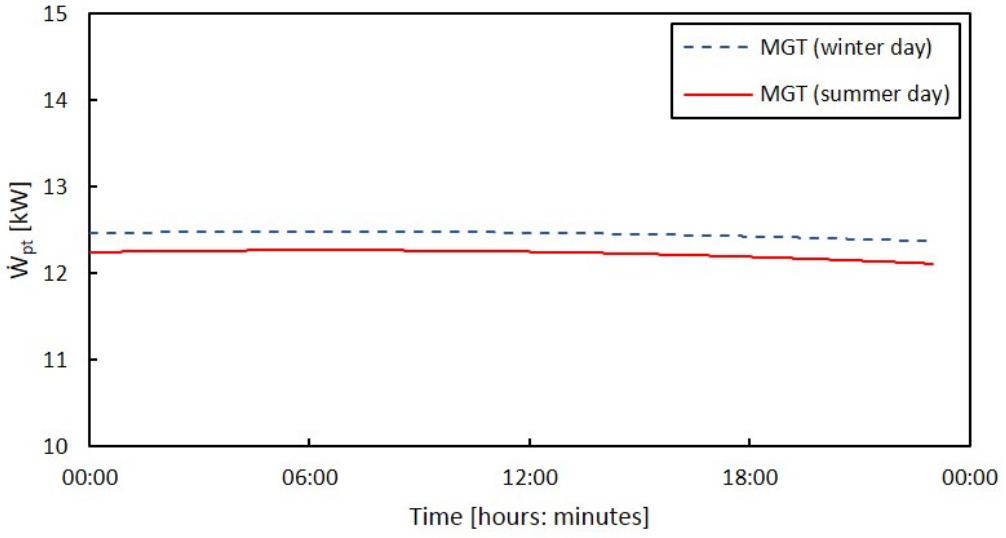

Figure 3.9: Useful work output of the MGT system under standard operation

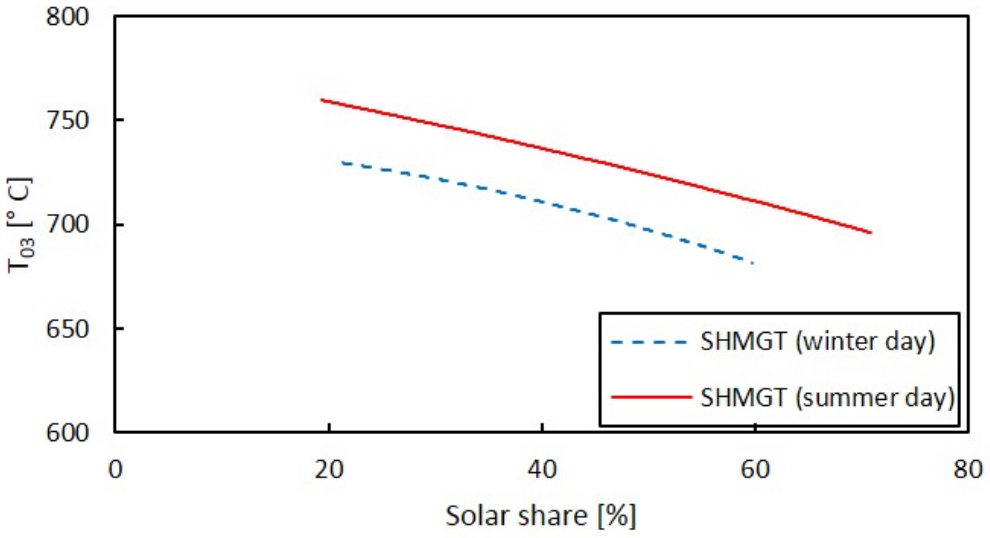

Figure 3.10: Effect of solar share on the gas-generator TIT

Overall, the predicted performance of MGT system under standard operation was consistent with the expected behaviour of a conventional gas turbine operating under low and high ambient temperature and pressure conditions. This in turn validated the predicted performance of the MGT system.

3.9.3 Solar-hybrid MGT system performance

Steady-state performance

The gas-generator TIT decreased with increasing solar share, but with higher gas-generator TIT predicted for the warmer solar day (see Figure 3.10). An increase in solar share typically results in a reduction in the fuel mass flow rate (as shown in Tables C.1 and C.2), due to a reduction in the combustion requirement. The reduction in the fuel mass flow rate further results in a reduction in the gas-generator TIT. Higher gas-generator TIT was predicted for the warmer solar day, due to the higher ambient temperature measured for that day. As was shown for the MGT system under standard operation (Figure 3.8), and as will later be shown for the MGT system under solar-hybrid operation (Figure 3.15), operating at higher ambient temperature typically results in higher gas-generator TIT.

An increase in solar share resulted in a reduction in the useful work output, with lower work output predicted for the warmer solar day (see Figure 3.11). An increase in solar share results in an increase in the system pressure losses (mainly across the combustion chamber, since the pressure loss across the solar receiver remained constant (see Tables C.1 and C.2)), which further results in a reduction in the useful work output. The lower work output predicted for the

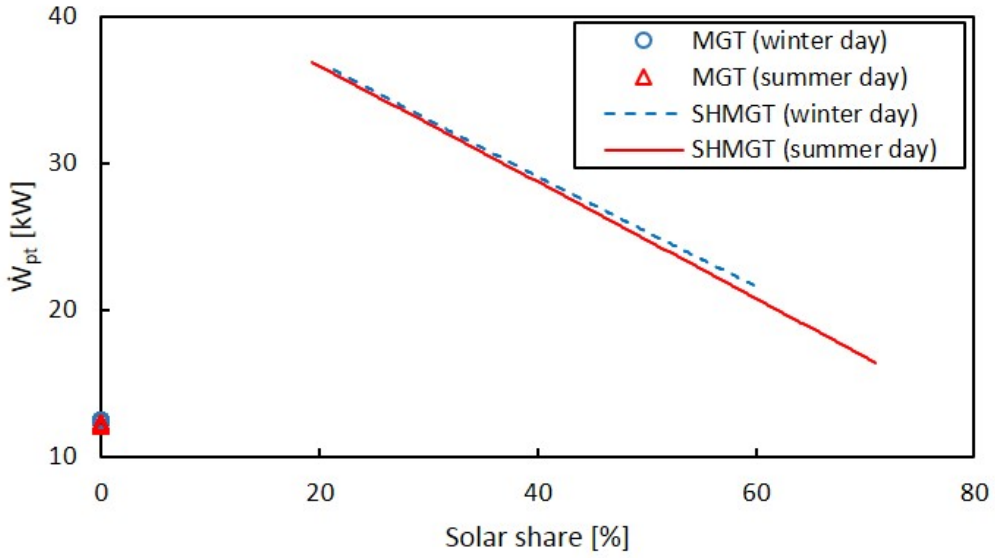

Figure 3.11: Effect of solar share on the useful work output

warmer solar day was a result of the higher system pressure losses predicted for that day.

The predicted work output of the MGT system under standard operation was additionally plotted on Figure 3.11. At solar share beyond 81 %, for the summer day, and 86 %, for the winter day, the work output of the MGT system under solar-hybrid operation drops below that predicted for the MGT system under standard operation.

The specific fuel consumption SFC decreased with increasing solar share, but with slightly higher SFC predicted for the warmer solar day, when operating at higher solar share (see Figure 3.12). SFC is directly proportional to the fuel mass flow rate and inversely proportional to the useful work output. As previously noted, the fuel mass flow rate decreases with increasing solar share, and lower fuel mass flow rates were predicted for the warmer solar day. Similarly, the useful work output decreased with increasing solar share, due to an increase in the MGT system pressure losses, when operating at higher solar share. Therefore, the SFC decreased with increasing solar share, due to the decrease in the fuel mass flow rate. For the warmer solar day, the decrease in the fuel mass flow rate was more than offset by the decrease in the work output, which resulted in the higher SFC.

The predicted SFC for the MGT system under standard operation was additionally plotted on Figure 3.12. As expected, the SFC for the MGT system under standard operation is higher than that under solar-hybrid operation, owing to the higher combustion requirement during standard operation.

The cycle thermal efficiency decreased with increasing solar share (see Figure 3.13), but with slightly higher cycle thermal efficiency predicted for the

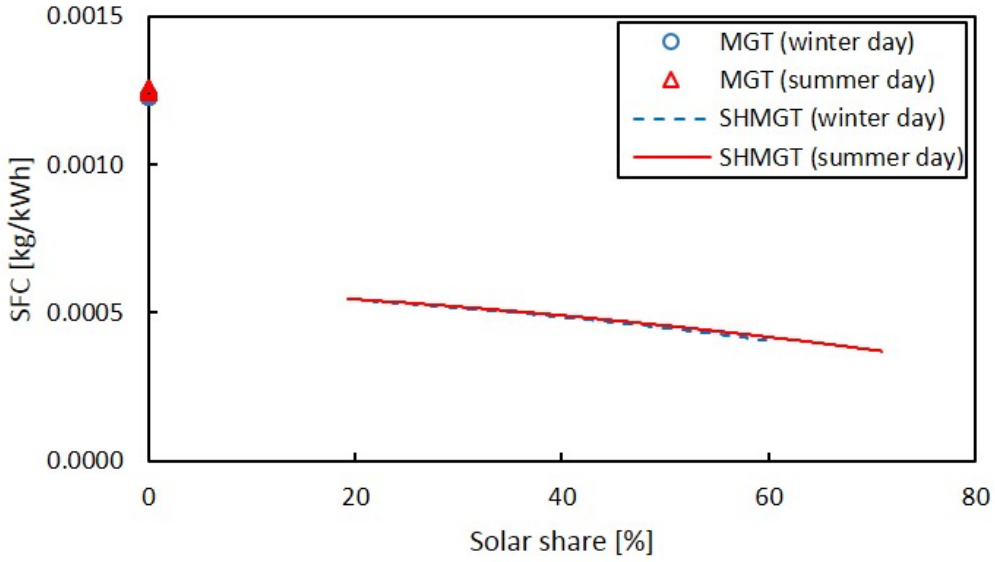

Figure 3.12: Effect of solar share on the SFC

cooler solar day, when operating at higher solar share. The cycle thermal efficiency is a function of both the useful work output and the total cycle thermal energy input. An increase in the solar share resulted in a decrease in both the useful work output and the total cycle thermal energy input, the latter due to a decrease in the combustion requirement. The cycle thermal efficiency decreased with increasing solar share because the decrease in the total cycle thermal energy input was more than offset by the decrease in the useful work output.

The predicted cycle thermal efficiency of the MGT system under standard operation was additionally plotted on Figure 3.13. At solar share beyond 69 %, for the winter day, and 74 %, for the summer day, the MGT system operates at a cycle thermal efficiency below that predicted for the MGT system under standard operation. This further limits the solar share operating range beyond that predicted for the work output.

The disparity in the predicted SFC, work output and cycle thermal efficiency, for both solar days was more pronounced at higher solar share (see Figures 3.11 to 3.13).

Overall, higher useful work output was predicted for the cooler solar day, but with the lowest work output predicted for noon of either selected solar day (see Figure 3.14). This period corresponded to that, for which the highest solar thermal energy input or highest solar share, and consequently highest system pressure losses were predicted (see Tables C.1 and C.2).

A parabolic trend was predicted for the work output during hours of solar irradiation, in contrast to the nearly linear trend predicted for the standard operation (see Figure 3.9). The parabolic trend is similar, but opposite in

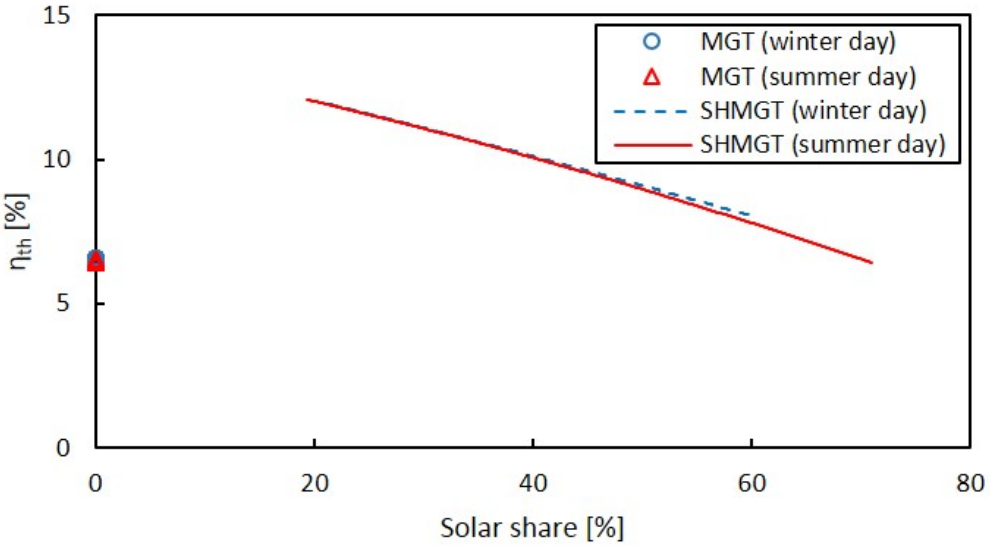

Figure 3.13: Effect of solar share on the cycle thermal efficiency

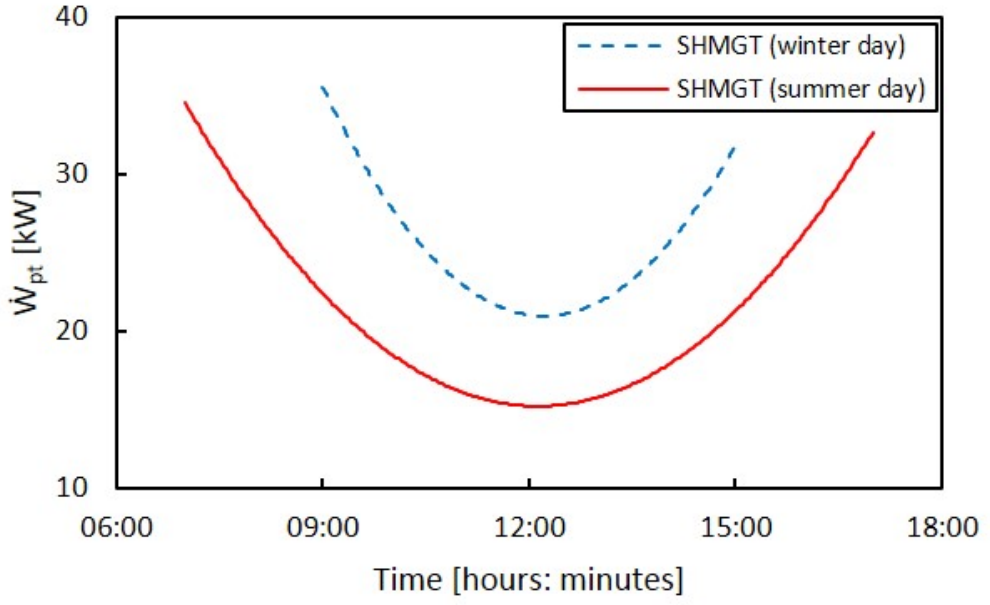

Figure 3.14: Useful work output for the MGT system under solar-hybrid operation

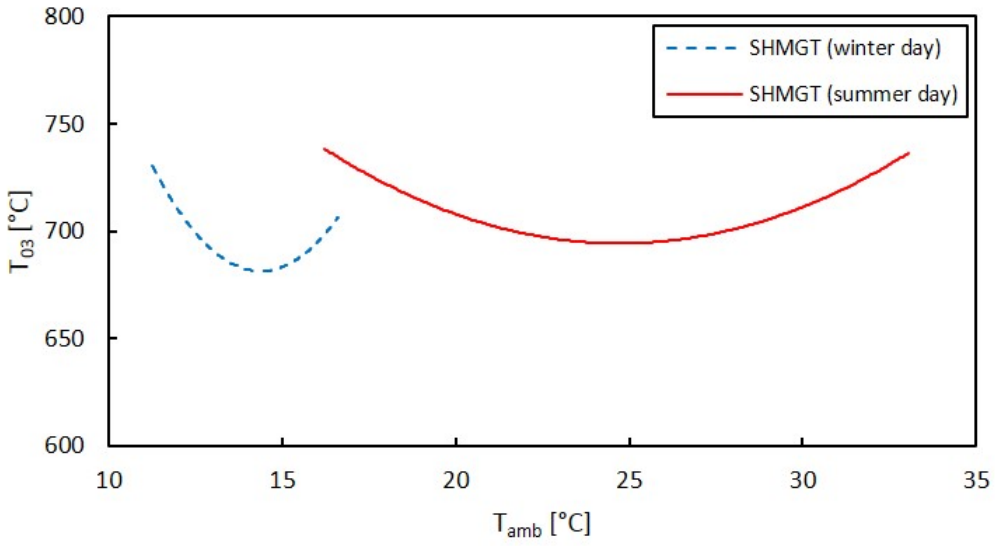

Figure 3.15: Effect of ambient temperature on the gas-generator TIT during solar-hybrid operation

nature to that shown by the DNI for the same period (see Figures 3.16a to 3.16d), and consequently that for the solar thermal energy input – given the latter was calculated from the former.

Similar to the MGT system under standard operation, the performance of the MGT system under solar-hybrid operation was also analysed by studying the effect of high and low ambient temperature and pressure conditions – during periods of solar irradiation for the two selected solar days – on MGT system performance parameters such as the gas-generator TIT, air mass flow rate and useful work output, for the obtained MGT system equilibrium running point.

For operation at higher ambient temperatures, higher gas-generator TIT was predicted for the MGT system under solar-hybrid operation, as seen for the warmer solar day (see Figure 3.15). In contrast to the linear relation observed for the standard operation (see Figure 3.8), the relation between the gas-generator TIT and ambient temperature for the MGT system under solar-hybrid operation was parabolic. This trend reflects the parabolic nature of the available solar energy resource/the solar thermal energy input during periods of solar irradiation for the two selected solar days.

Similar to the MGT system under standard operation, lower air mass flow rates were predicted for the MGT system under solar-hybrid operation, when operating at higher ambient temperatures. Similarly, lower air mass flow rates were predicted for the MGT system under solar-hybrid operation, when operating at lower ambient pressures. The overall result of all these effects was a lower work output predicted for the warmer solar day.

The main steady-state performance parameters for the MGT system under solar-hybrid operation are further summarised in Tables C.1 and C.2, while those for the MGT system under standard operation are summarised in Tables C.3 and C.4, for a winter day (04 August, 2016), and a summer day (04 January, 2017), respectively.

For the MGT system under solar-hybrid operation, a nominal useful work output of 20 kW, at a SFC of 0.0004 kg/kWh and a cycle thermal efficiency of 8 % was predicted. With the addition of recuperation, the cycle thermal efficiency could potentially be increased to 20 %. In contrast, a lower nominal work output of 12.5 kW, at a higher SFC of 0.0012 kg/kWh and a lower cycle thermal efficiency of 7 %, was predicted for the MGT system under standard operation, with the cycle thermal efficiency potentially increasing to only 17 %, with the addition of recuperation.

Transient performance

The predicted transient behaviour of the MGT system under solar-hybrid operation, throughout each of the four selected days is shown in Figures 3.16 and 3.17. In Figure 3.16, the DNI, gas-generator TIT and rotational speed and the useful work output were plotted for each minute of the four selected solar days. Because of its significantly lower order of magnitude, the fuel mass flow rate was plotted separately, with the DNI included for clarity (see Figure 3.17).

Similar to the predicted steady-state performance, the gas-generator TIT and useful work output decreased with increasing DNI, while the opposite was true for the gas-generator rotational speed. The nearly constant segments at both ends of the plotted graphs correspond to standard MGT system operation, during periods of zero or insufficient solar irradiation.

A sudden increase in DNI normally resulted in a sudden reduction in the fuel mass flow rate, to maintain the MGT system operating at the determined solar-hybrid MGT system equilibrium running point, throughout the four selected solar days. On the other hand, a sudden drop in the DNI – which similarly corresponded to a sudden drop in the solar thermal energy input and solar share – resulted in a sudden increase in the fuel mass flow rate, either to maintain the MGT system operating at the determined solar-hybrid MGT system equilibrium running point, or to completely switch to standard MGT system operation mode.

The switch to standard MGT system operation mode generally corresponded to higher fuel mass flow rates, due to the zero solar thermal energy input. Standard MGT system operation also corresponded to lower gas-generator TIT, rotational speed, and power turbine power output, owing to the lower gas-generator compressor power requirement at the determined standard MGT system equilibrium running point.

Generally stable MGT system solar-hybrid operation was achieved for typical winter, spring and summer days. On the contrary, solar-hybrid operation

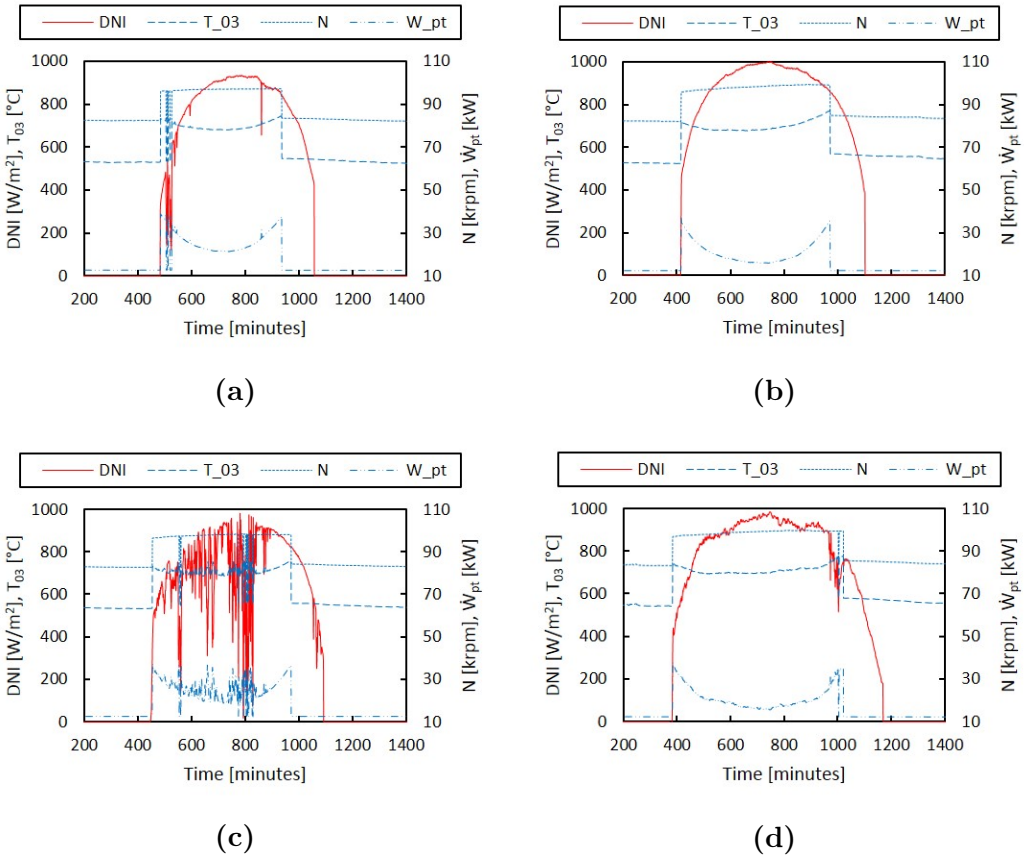

Figure 3.16: DNI, gas-generator TIT and rotational speed and useful work output throughout a; (a) winter day, (b) spring day, (c) autumn day and (d) summer day

on a cloudy autumn day required several increases in fuel mass flow rate, either to maintain the MGT system operating at the determined solar-hybrid MGT system equilibrium running point, or to allow the switch to standard MGT system operation mode.

For the selected control strategy of maintaining the MGT system operating at the determined solar-hybrid equilibrium running point, equilibrium running of the MGT system in solar-hybrid mode could only be achieved for solar share of at least 19 % for both the autumn and spring days, 17 % for the summer day and 15 % for the winter day. The switch to standard MGT system operation mode was therefore executed at solar share below these values, for each respective solar day.

As expected, the predicted gas-generator rotational speed did not vary significantly for each of the four selected solar days, when operating at the determined solar-hybrid equilibrium running point. The standard deviation for the gas-generator rotational speed was 281 rpm for the winter day, corresponding to a rotor over speed of 100.3 %, 480 rpm for the autumn day, corresponding to a rotor over speed of 100.5 %, 843 rpm for the summer day, corresponding

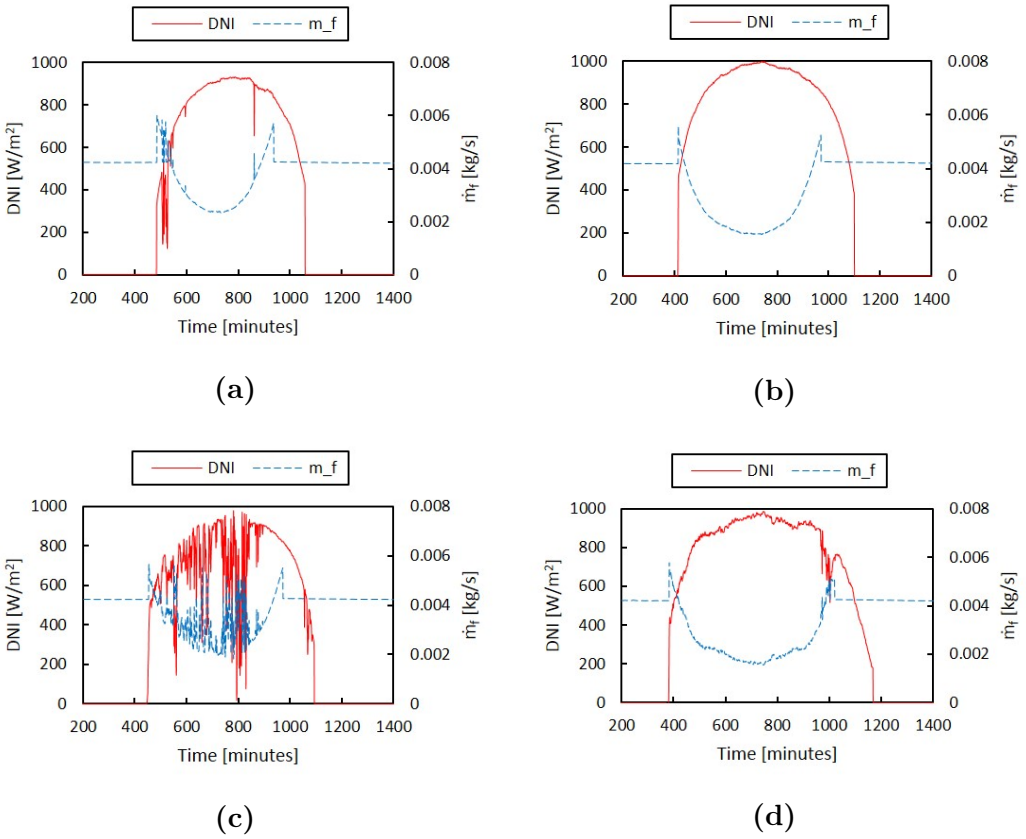

Figure 3.17: DNI and fuel mass flow rate throughout a; (a) winter day, (b) spring day, (c) autumn day and (d) summer day

to a rotor over speed of 100.9 % and 970 rpm for the spring day, corresponding to a rotor over speed of 101.0 %. By maintaining the MGT system operating at the determined solar-hybrid equilibrium point, the predicted gas-generator rotational speed remained below the maximum industry accepted rotor over speed limit of 105 %, for all four selected solar days.

Therefore, operating the MGT system at the determined solar-hybrid equilibrium point during solar-hybrid operation could eliminate the risk of running into compressor surge, albeit with a reduced surge margin.

3.10 Conclusion

The aim of the modeling work was to predict the performance of a MGT system under solar-hybrid operation, in order to determine the possible operating range, and formulate operation and control strategies for the MGT system. The modeling considered both steady-state and transient operation, and used meteorological data for four arbitrarily selected solar days, one for each climatic

season experienced in Southern Africa.

The matching of the individual MGT system components showed that the equilibrium running (operating) point of the MGT system shifted to a region of higher compressor pressure ratio and non-dimensional speed and mass flow rate on the compressor characteristic. The shift of the MGT system equilibrium running point was to counter the system pressure losses introduced by the addition of solar thermal energy into the MGT system, and ensure the compressor work requirement was met by the coupled gas-generator turbine, while also maintaining a useful work output from the power turbine. The shift of the MGT system equilibrium running point resulted in a reduction in the surge margin, from 50 to 21 %, but still within the typical surge margin expected for power and propulsion applications.

A nominal work output of 20 kW, at a SFC of 0.0004 kg/kWh and a cycle thermal efficiency of 8 % was predicted for the MGT system under solar-hybrid operation. With the addition of recuperation, the cycle thermal efficiency could potentially be increased to 20 %. In contrast, a lower nominal work output of 12.5 kW, at a higher SFC of 0.0012 kg/kWh and a lower cycle thermal efficiency of 7 %, was predicted for the MGT system under standard operation, with the cycle thermal efficiency potentially increasing to only 17 %, with the addition of recuperation. Subsequently, better solar-hybrid performance is expected for a MGT system based on more efficient/better performing individual components.

Despite its limitations, as a first iteration, the transient model was able to illustrate the fuel flow alterations necessary to counter sudden changes in solar irradiation, when the proposed control strategy of operating the MGT system at the determined solar-hybrid equilibrium running point was implemented. Furthermore, the gas-generator rotational speed remained below the maximum industry accepted rotor over speed limit, implying that solar-hybrid equilibrium running could potentially eliminate the risk of running into compressor surge, albeit with a reduced surge margin.

Overall, equilibrium running of the MGT system under solar-hybrid mode should be possible for solar share of at least 20 %, for any solar day. For solar share beyond 81 %, for the summer day, and 86 %, for the winter day, the work output of the MGT system under solar-hybrid operation drops below that predicted for the MGT system under standard operation. On the other hand, for solar share beyond 69 %, for the winter day, and 74 %, for the summer day, the MGT system operates at a cycle thermal efficiency below that predicted for the MGT system under standard operation, further limiting the solar share operating range. Therefore, depending on the MGT system design requirements for work output or cycle thermal efficiency, a suitable control system that can maintain solar-hybrid operation within these solar share limits, and completely switch to standard operation otherwise would need to be designed.

Other control measures implemented during the modeling, that should also

be implemented in the physical MGT system include: setting the receiver outlet temperature to never exceed the desired equilibrium running gas-generator TIT, and bypassing the solar receiver during periods of no or insufficient solar irradiation.

3.11 Research contribution

The findings from the earliest modeling work were presented at the 4th Southern African Solar Energy Conference (SASEC), and published in Ssebabi *et al.* (2016), as part of the peer-reviewed conference proceedings. The latest findings from the modeling work, largely as presented in this chapter, were published in Ssebabi *et al.* (2019).

Chapter 4

Design and Experimental Work

The purpose of the experimental work was to design, build, test and characterise the performance of an experimental MGT system, in order to validate its predicted performance. From the determined performance of the MGT system, the technical feasibility of adapting such a system to solar-hybrid operation was also assessed.

This chapter discusses the set up of the experimental MGT system test bench, the experimental procedure followed, the measured parameters – and the performance parameters calculated from these measurements, as well as the uncertainty associated with both the measured and the calculated parameters. In addition, the experimental validation of the developed mathematical model, and the technical feasibility of adapting the developed experimental MGT system to solar-hybrid operation are covered.

4.1 MGT system test bench

The experimental MGT system test bench consists of a gas generator and a power turbine – both based on the commercially available BorgWarner turbochargers considered for the modeling work (see Figure 4.1), as well as an in-house designed and manufactured tubular type combustion chamber. In addition, the test bench is equiped with four differential pressure class meters; two orifices, a flow nozzle and a Venturi tube, all specifically designed and manufactured for this study, except for the flow nozzle that was already available in-house. The design process for the flow meters was in accordance with ASME PTC 19.5 (2004).

The selection of the instrumentation used on the test bench, the location of the measurement points and the methods of measurement followed guidelines given by ASME PTC 22 (2014), but with further reference made to ASME PTC 10 (1997), ASME PTC 19.2 (1987) and ASME PTC 19.3 (2004). Four static pressure taps and four static temperature taps were provided at each corresponding measurement point, except for the fuel supply system – owing

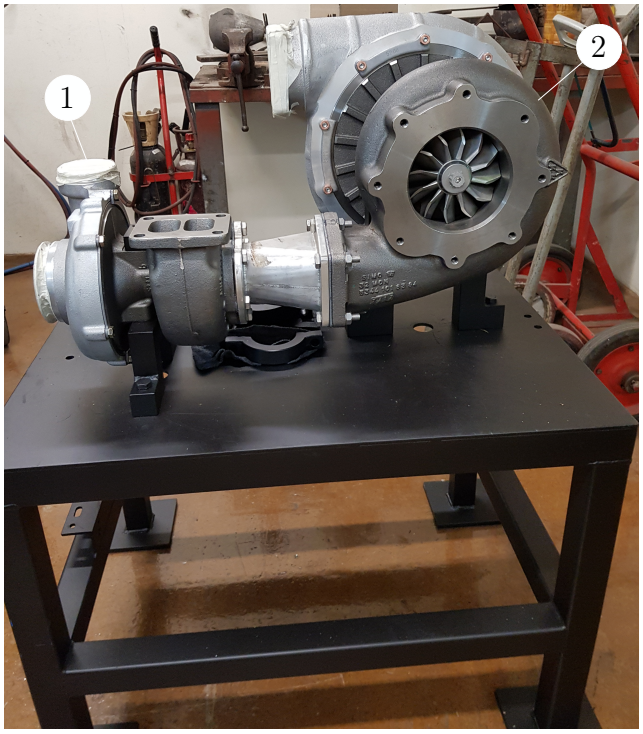

Figure 4.1: Coupling of the turbochargers; 1. K31, 2. K44

to the small size of tubing used (10 mm OD/8 mm ID). The pressure taps were located circumferentially around the piping, and spaced 90° apart, as were the temperature taps, but with the latter placed 45° to the former, to ensure a different line of sight.

A schematic layout of the MGT system test bench, with the location of the measurement points also indicated, is shown in Figure 4.2, while the CAD model of the same test bench is shown in Figure 4.3

On the test bench, a high-pressure turbine drives a high-pressure compressor, and the two act as a gas generator for a low-pressure and mechanically independent power turbine. The power turbine is directly coupled to a low-pressure compressor, with the former loaded through throttling the latter. The useful work output of the power turbine was determined indirectly, as the power absorbed by the driven low-pressure compressor.

The numbers 1 and 2 in the schematic layout denote the gas-generator compressor inlet and outlet stations, 3 and 4 denote the gas-generator turbine inlet and outlet stations, 4 and 5 denote the power turbine inlet and outlet stations and 7 and 8 denote the low-pressure compressor inlet and outlet stations. The numbers 2 and 3 as well denote the combustion chamber inlet and outlet stations. For consistency, the numbering in this schematic layout omits station 6 (solar receiver outlet (see Figure 3.1)), as the experimental MGT system test bench does not include a solar receiver.

The operation of the MGT system is based on the Brayton cycle. Ambient

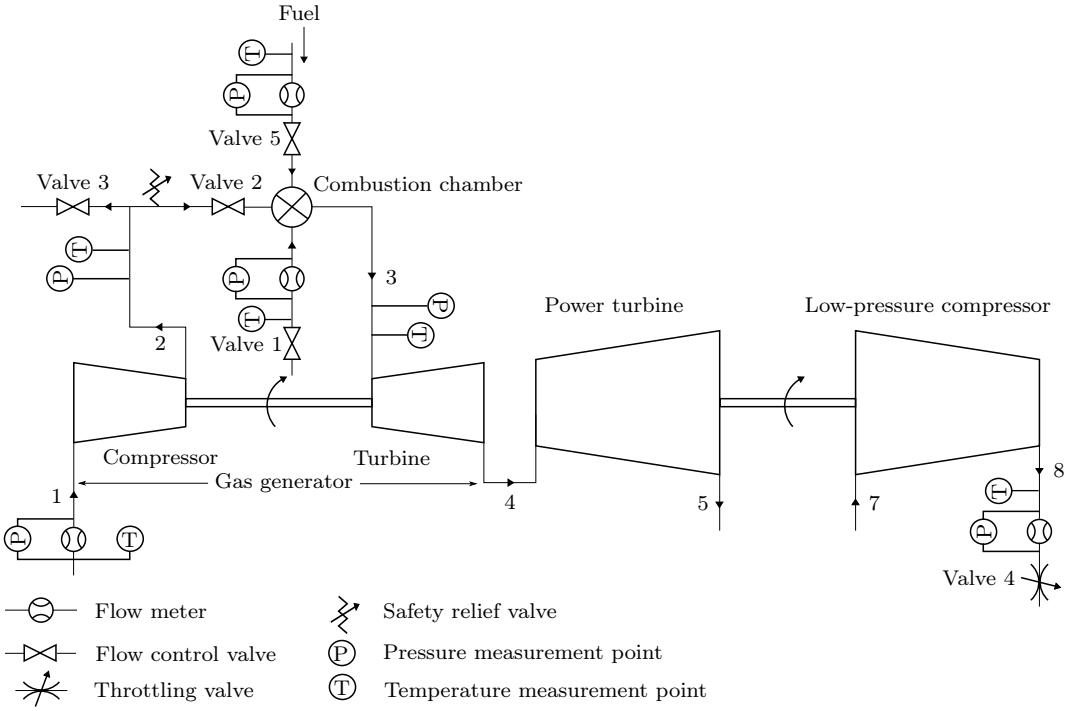

Figure 4.2: Schematic layout of the MGT system test bench

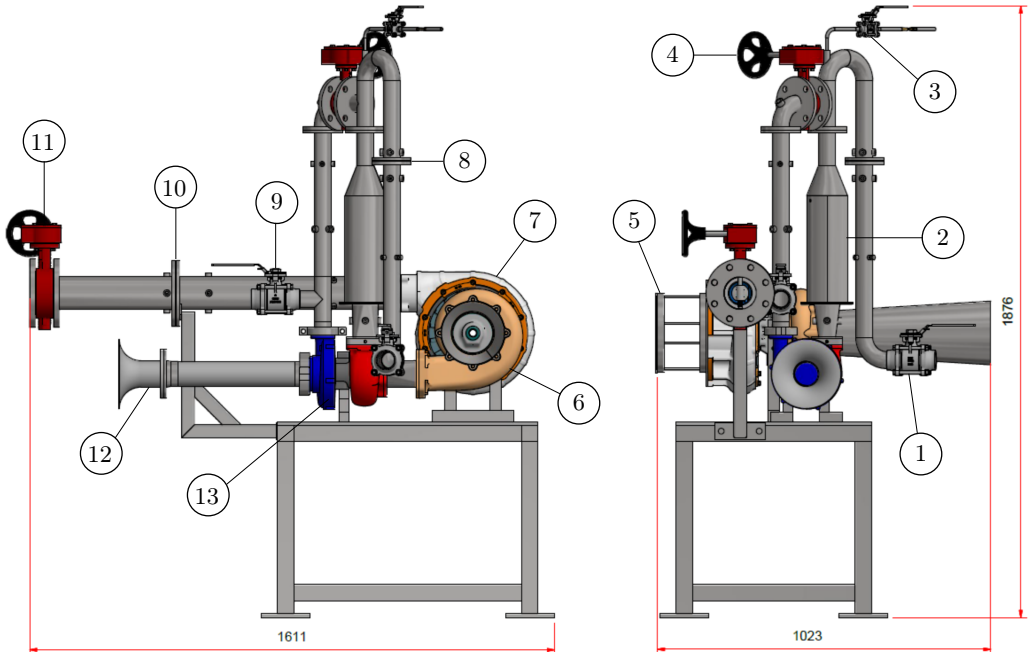

Figure 4.3: CAD model of the MGT system test bench; 1. Valve 1, 2. Combustion chamber, 3. Valve 5, 4. Valve 2, 5. Protective wire mesh grid, 6. Power turbine, 7. Low-pressure compressor, 8. Orifice 1, 9. Valve 3, 10. Orifice 2, 11. Valve 4, 12. Bellmouth, 13. Gas-generator compressor

air is first compressed in the gas-generator compressor. The pressurised air leaving the compressor is then raised to the desired gas-generator turbine inlet temperature, through combusting fuel – in this case propane – in the combustion chamber. The hot gases are then expanded; first in the gas-generator turbine, to meet the compressor work requirement, and thereafter in the power turbine, to generate useful shaft work. The power turbine exhaust gases are then released to the atmosphere. The low-pressure compressor similarly compresses ambient air, before then exhausting it to the atmosphere.

For the piping and ducting, DN50 and DN100 stainless steel grade 304 hygienic tubing, and corresponding 90° bends and equal tee-pieces were used. The ducting at the outlets of both the combustion chamber and the gas-generator turbine consisted of square to round ducts, manufactured from stainless steel grade 304 sheet metal. Care was taken to make these ducts as short as possible, to minimise the pressure drop across them. The duct length was kept at 100 mm, with the dimensions of the round/square sections constrained by those of the components being joined.

The flanges used on the test bench included standard T1000 slip-on stainless steel flanges, as well as in-house manufactured flanges, with the latter used for sections such as the orifice meters and the exhaust ducts. The flanged piping sections were fastened using a combination of standard stainless, electro galvanised and black steel hexagonal head and cup screws and bolts, complete with washers and nuts. For sealing purposes at the flanged piping sections, gaskets cut from either 1.5 mm thick JMP6000 material or reinforced 2 mm thick BAR-302 material were used, the former for the low-temperature (up to 200 °C) piping sections, and the latter for the high-temperature flanged piping sections.

A key feature of solar-hybrid gas turbine systems is the requirement for multiple usage of fast acting flow control and blow-off valves. The flow control valves include air flow control valves, which re-direct the air flow during the switch between solar and non-solar gas turbine operation modes, and fuel control valves, which regulate the fuel supply. The blow-off valves vent the solar heated air during load shedding/emergency shutdowns, to prevent gas turbine rotor over speed. Similarly, the designed MGT system test bench has five electro-pneumatically operated flow control valves (valve 1 to 5). These valves comprise of three CONDOR BV3PS stainless steel ball valves and two SLIM Series 300 butterfly valves. The valves were used to implement the MGT system start-up sequence, regulate the fuel flow, and throttle the low-pressure compressor.

The electro-pneumatic actuation of the valves was achieved using Air Torque AT051U, AT201U and AT301U spring return pneumatic actuators, coupled to Trewfit DT-S11 and Samson 3725 positioners. The pneumatic actuators required compressed air, supplied at a gauge pressure of 6 bar. The air supply pressure was set using a Festo LFR-D-Mini pressure regulator. The positioners required an analog signal input of 4 to 20 mA DC current. This current analog

signal was supplied by both an NI 9265 analog current output module and an NI 9263 analog voltage output module, with the latter wired to an AC/DC Dynamics SIC1V signal converter. This signal converter converts a 0 to 10 V DC voltage signal input to a 4 to 20 mA DC current signal output.

The MGT system was started using compressed air supplied by an existing compressed air line. This air was first passed through the combustion chamber, and then through the gas-generator turbine, which in turn drove the directly coupled gas-generator compressor. The air supply pressure was regulated using an STNC TRY-50 Series pressure regulator fitted to the compressed air line. A Dingli QSL-50 air filter was also fitted to the compressed air line, to trap foreign objects in the supplied air.

The MGT system could have been started using an electric motor driving the gas generator compressor, but this would have introduced the added complexity of having to alter the physical structure of the gas generator, in order to successfully couple it to the starter motor. The use of compressed air had the added advantage that the energy available to the gas-generator compressor could be increased just by adding fuel and initiating combustion in the combustion chamber. The additional energy allowed the gas-generator compressor to draw sufficient air to maintain combustion, during the implementation of the MGT system start-up procedure.

The lubrication of the bearings of the two turbochargers on which the MGT system is based was achieved using an oil lubrication system designed and built by Nieuwoudt (1987). This lubrication system is further described in Subsection 4.1.4.

Safety features fitted to the test bench included a VYC 095 AP brass PN16/25 safety relief valve and an emergency stop push button. The former was fitted downstream of the high-pressure gas-generator compressor, and was configured to open, as soon as the set maximum pressure of 350 kPa was exceeded. The latter was used to perform emergency shutdowns of the MGT system. Pushing the emergency stop button cut off the analog signal to the valve actuators, which in turn switched the valves to their default fail-safe mode. Depending on their status, valves 1 and 2 either remained closed, or immediately closed, to stop air supply to the combustion chamber, valves 3 and 4 either remained open or immediately opened, to release any pressurised air downstream of the compressors, and valve 5 either remained closed or immediately closed, to shut off the fuel supply to the combustion chamber.

Additionally, protective wire mesh grids were fitted to the inlets of both compressors. These safety grids prevented the compressors from sucking foreign objects, which could potentially damage the compressor blades.

4.1.1 Combustion chamber design

The combustion chamber of the MGT system is of a tubular type. A tubular layout was chosen, because it's relatively easy to develop, at low cost (Lefebvre

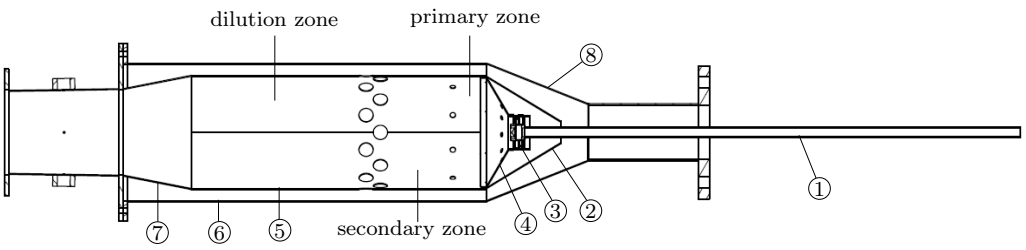

Figure 4.4: Sectioned view of the designed tubular type MGT system combustion chamber

and Ballal, 2010). A tubular type combustion chamber basically consists of a cylindrical liner/flame tube mounted concentrically inside a cylindrical casing.

A sectioned view of the designed tubular type combustion chamber is shown in Figure 4.4, with the main parts comprising of; 1. fuel supply line, 2. snout, 3. swirler, 4. dome, 5. flame tube, 6. casing, 7. nozzle, 8. diffuser.

The combustion chamber design was adapted from Hummel (2014), and the design process similarly followed a simplified approach proposed by Conrado *et al.* (2004), as well as the work of Lefebvre and Ballal (2010). The different combustion chamber components were sized, using a combination of basic geometry, air mass flow ratios and empirical equations found in literature.

The calculation of the design parameters of the combustion chamber was performed in MATLAB 2017a, with the determined design parameters then used as inputs to the development of the CAD model in Autodesk Inventor 2016. The sizing of the different combustion chamber components is discussed as follows:

Casing and flame tube

The cross-sectional area of the cylindrical casing corresponds to the maximum cross-sectional area of the combustion chamber. This cross-sectional area is referred to as the reference area A_{ref}, and was determined using

$$A_{ref} = \left[\frac{R}{2}\left(\frac{\dot{m}_a\sqrt{T_2}}{P_2}\right)^2\left(\frac{\Delta P_{comb}}{q_{ref}}\Big/\frac{\Delta P_{comb}}{P_2}\right)\right]^{0.5} \tag{4.1}$$

where $(^{\Delta P_{comb}}/_{q_{ref}})$ is the pressure loss factor, and is defined as the ratio of the total pressure drop across the combustion chamber to the reference dynamic pressure, while $(^{\Delta P_{comb}}/_{P_2})$ is the ratio of the total pressure drop across the combustion chamber to the inlet total pressure, expressed as a percentage. A typical value of 37 was assumed for the former, while a suitably low value of 4 % was assumed for the latter, both as suggested by Lefebvre and Ballal.

According to Conrado *et al.*, the cross-sectional area of the flame tube A_{ft} can be estimated as 0.7 of A_{ref}, with the casing diameter D_{ref} and the flame tube diameter D_{ft} (see Figure 4.5) then calculated from the corresponding

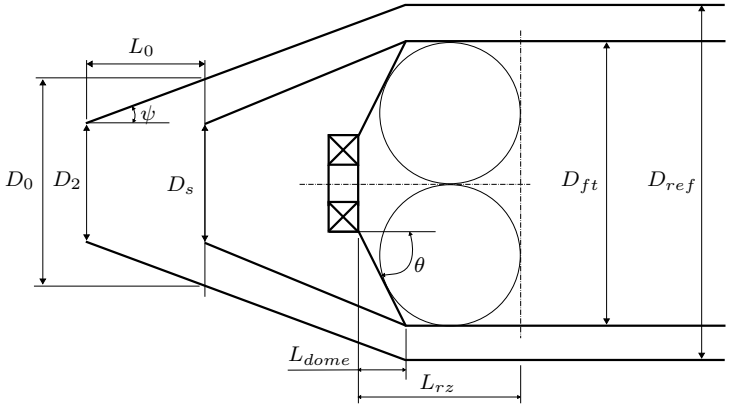

Figure 4.5: Combustion chamber inlet geometry (adapted from Conrado *et al.*, 2004)

cross-sectional area. The cross-sectional area of the annulus between the casing and the flame tube A_{an} was calculated as the difference between the reference area and the cross-sectional area of the flame tube.

Combustion chamber zones

The lengths of the different combustion chamber zones were estimated as fractions of the obtained flame tube diameter, as suggested by Murthy (1988). The length of the primary zone was estimated to be 0.8 of D_{ft}, while that of the secondary zone was estimated to be 0.4 of D_{ft}, and that of the dilution zone was estimated to be 1.4 of D_{ft}. The total length of the flame tube was then determined as the sum of the obtained combustion chamber zone lengths.

To determine the air distribution throughout the different zones of the combustion chamber, the air mass flow rate required for complete combustion in the primary zone had to first be estimated. Assuming a slightly lean fuel/air mixture, with an equivalence ratio ϕ of 0.9, and taking the stoichiometric air/fuel ratio for propane as 15.7, the primary zone air mass flow rate was determined from

$$\dot{m}_{pz} = 15.7\phi\dot{m}_f \tag{4.2}$$

with the air distribution across the secondary zone then determined from the difference between the total air mass flow rate and the primary zone air mass flow rate.

Assuming a constant air velocity, the cross-sectional area at which the air flow is divided between the snout and the annulus A_0 (see Figure 4.5) was calculated using

$$\frac{A_0}{A_{an}} = \frac{\dot{m}_a}{\dot{m}_{an}} \tag{4.3}$$

where the air distribution through the annulus $\dot{m}_{an}$ was calculated as the difference between the total air mass flow rate and the air mass flow rate

admitted through the snout $\dot{m}_s$ – the latter typically assumed to be half of the primary zone air mass flow rate.

Diffuser

The design of the diffuser entailed firstly calculating its divergence angle ψ, using the following expression

$$\frac{\Delta P_{dif}}{P_2} = 1.75R \left[\frac{\dot{m}_a\sqrt{T_2}}{P_2}\right]^2 \frac{(\tan\psi)^{1.22}}{A_2^2} \left[1 - \frac{A_2}{A_0}\right]^2 \tag{4.4}$$

with a typical value of 1 % assumed for the ratio of the diffuser pressure drop to the compressor delivery pressure $^{\Delta P_{dif}}/_{P_2}$. From the known compressor outlet pipe diameter D_2, the casing diameter and the divergence angle of the diffuser, the length of the diffuser was then determined, using basic geometry (see Figure 4.5).

Snout

For the design of the snout, the cross-sectional area of the inlet of the snout was first calculated from the corresponding air mass flow ratio, using

$$\frac{A_s}{A_0} = \frac{\dot{m}_s}{\dot{m}_a} \tag{4.5}$$

with the diameter of the inlet of the snout D_s then calculated from the obtained inlet cross-sectional area. The length of the gap between the inlet of the diffuser and that of the snout was then determined, similarly using basic geometry

$$L_0 = \frac{D_0 - D_s}{2\tan\psi} \tag{4.6}$$

with the length of the snout then calculated as the difference between the length of the diffuser and the length of the determined gap.

Swirler

A swirler was fitted into the dome, around the fuel injector, to create flow re-circulation in the primary zone, in order to improve mixing. The recirculation enables the mixing of part of the hot combustion gases with incoming air and fuel (Lefebvre and Ballal, 2010). The swirler area A_{sw} was calculated from the following expression proposed by Knight and Walker (1957) and cited by Lefebvre and Ballal (2010)

$$\dot{m}_{sw} = \left[\frac{2\rho_3\Delta P_{sw}}{K_{sw}\left[(\sec\beta/A_{sw})^2 - 1/A_{ft}^2\right]}\right]^{0.5} \tag{4.7}$$

where ΔP_{sw} is the pressure drop across the swirler, and was assumed to be 3 % of the compressor delivery pressure. β is the swirl vane angle, and was assumed to be 60°. $\dot{m}_{sw}$ is the mass flow rate through the swirler, and was assumed to be 10 % of the total air mass flow rate. The swirler was designed with flat vanes, mainly because they can easily be manufactured, at low cost (Knight and Walker, 1957; Lefebvre and Ballal, 2010). Flat vanes also promote a more stable flame, and reduce combustion noise. A flat vane concordance factor K_{sw} of 1.3 was further assumed for the swirler. All the above assumed values lie within the range of typical values proposed by Lefebvre and Ballal (2010).

The swirler diameter D_{sw} was determined from the calculated swirler area, using

$$A_{sw} = (\pi/4)\left(D_{sw}^2 - D_{hub}^2\right) - 0.5 n_v t_v \left(D_{sw} - D_{hub}\right) \tag{4.8}$$

where D_{hub} is the fuel injector diameter, n_v is the number of swirler vane blades and and t_v is the blade thickness. The swirler was designed with 8 vane blades, of 0.9 mm thickness – optimum values suggested by Lefebvre and Ballal.

The length of the recirculation zone was then estimated to be twice the determined swirler diameter. Care was also taken to ensure the recirculation zone was shorter than the primary zone.

Dome

The inlet diameter of the dome was determined from the swirler diameter, since the swirler was fitted into the dome. Both the snout and the dome were fitted into the flame tube, and fastened to it using 1 mm diameter stainless steel wire. The snout and dome exhaust diameters were therefore calculated as the difference between the known flame tube diameter and the cumulative sheet metal thickness of the snout and dome fitted inside it. The dome angle was then determined using (Conrado *et al.*, 2004)

$$\theta = acos\left[\frac{-D_{ft}\left(D_{ft} - 2D_{sw}\right) - \left(D_{ft} - 4L_{rz}\right)\sqrt{D_{ft}^2 - 4D_{ft}D_{sw} + 4D_{sw}^2 - 8D_{ft}L_{rz} + 16L_{rz}^2}}{2D_{ft}^2 - 4D_{ft}D_{sw} + 4D_{sw}^2 - 8D_{ft}L_{rz} + 16L_{rz}^2}\right] \tag{4.9}$$

with the length of the dome determined from basic geometry, using

$$L_{dome} = \frac{D_{dome} - D_{sw}}{2\tan\theta} \tag{4.10}$$

Air admission holes

The desired air distribution amongst the different combustion chamber zones is achieved through properly selecting the number, size and type of air admission holes for each zone. For ease of manufacturing, plain round holes were chosen, rather than the more complicated plunged type. Although there are no definitive guidelines for selecting an optimal number of flame tube holes,

Table 4.1: Combustion chamber design parameters

D_{ref} [mm]	D_{ft} [mm]	D_s [mm]	D_0 [mm]	D_{sw} [mm]	D_{hub} [mm]	D_{dome} [mm]	$D_{h,pz}$ [mm]	$D_{h,sz}$ [mm]	$D_{h,dome}$ [mm]	L_0 [mm]	L_{dome} [mm]	θ [°]	ψ [°]
123	103	18	70	31	15	98	5	13	4	25	20	59.5	21.6

a small number of large holes is generally selected, because large holes produce large jets and large-scale flow recirculations, which provide ample time for combustion (Lefebvre and Ballal, 2010). For the primary zone, a single row of 10 holes was laser cut into both the dome and the flame tube, while two rows of 10 holes each were laser cut into the secondary zone.

The total hole area for each combustion chamber zone A_h was determined from the air distribution through that zone, using the following basic equation for flow through a hole

$$\dot{m}_h = CA_h\sqrt{2\rho_2\Delta P_h} \tag{4.11}$$

where C is the coefficient of discharge for each air admission hole. A value of 0.6 was assumed for the hole coefficient of discharge, as experimentally determined for plain round holes by Freeman (1965) and Kaddah (1964). ΔP_h is the pressure drop across the holes. This pressure drop was assumed to be equal to the total pressure drop across the flame tube.

The diameter for each air admission hole was thereafter calculated using

$$D_h = \sqrt{\frac{4A_h}{N_h\pi}} \tag{4.12}$$

where N_h is the total number of holes for each combustion chamber zone.

Fuel injector

The combustion chamber was also fitted with a fuel injector, which basically consists of a fuel nozzle designed and manufactured in-house, and an 8 mm ID stainless steel grade 304 tube. The design of the fuel nozzle was based on typical LPG gas fuel nozzles. Other components of the fuel supply system include an in-house designed and manufactured venturi tube flow meter and a flow control valve. The fuel supply system is further discussed in Subsection 4.1.3.

Nozzle

The final combustion chamber component was the nozzle. The length of the nozzle was assumed to be 0.6 of D_{ft}, as suggested by Murthy (1988). The nozzle's inlet diameter was set to that of the flame tube, while its outlet diameter was set to that of the exhaust duct of the combustion chamber.

The main combustion chamber design parameters are shown in Table 4.1.

Material selection and manufacturing

The combustion chamber was manufactured from 0.9 mm thick stainless steel grade 304 sheet metal. Grade 304 is the most versatile and widely used stainless steel grade, owing to its good corrosion resistance, mechanical properties, weldability and chemical composition (Macsteel VRN, 2009). It's maximum permissible continuous service temperature of 925 °C is also higher than the expected combustion chamber exhaust temperature.

CAD manufacturing drawings for all the individual combustion chamber components were created in Autodesk Inventor Professional 2016. These components were then mainly manufactured through laser cutting. Apart from the dome and snout that were fastened to the flame tube using stainless steel wire, the rest of the combustion chamber components were assembled using gas welding. The use of wire allowed a provision to assemble/disassemble the snout, and the dome and swirler fitted within it, whenever necessary. The use of wire further allowed for thermal expansion within the front section of the combustion chamber during normal operation, which wouldn't be possible with say a welded assembly. Eight stainless steel grade 304 sheet metal strips were bent to the inner diameter of the casing, and welded onto the flame tube. These metal strips ensured the flame tube stayed concentric within the casing.

Figure 4.6a shows the flame tube assembly, while Figure 4.6b shows the assembled flame tube fitted inside the casing. The location of the electrodes, as well as the ignition spark that was produced by the electrodes during the test runs can also be seen. The dome, with the swirler fitted inside it, and the fuel nozzle fitted into the swirler can additionally be seen.

4.1.2 Instrumentation

Differential pressure class meters

The different mass flow rates through the MGT system were measured using differential pressure class meters. The air mass flow rate through the gas-generator compressor was measured using a flow nozzle (bellmouth), while that through the low-pressure compressor and that of the compressed air used to start the MGT system was measured using orifice meters. The fuel mass flow rate was measured using a Venturi tube.

The bellmouth was already available in-house, and only the orifice and the Venturi tube meters needed to be designed and manufactured. Guidelines for the design of these flow meters can be found in ASME PTC 19.5 (2004).

The orifice meters were designed within the pipe size and Reynolds number limits stipulated by the ASME PTC 19.5 Standard. The Venturi tube was designed outside the stipulated throat diameter Reynolds number limits – owing to the low fuel mass flow rates expected – and therefore had to be calibrated. The calibration procedure for the Venturi tube is discussed in Appendix A.3. The calibration procedure for the bellmouth can be found in

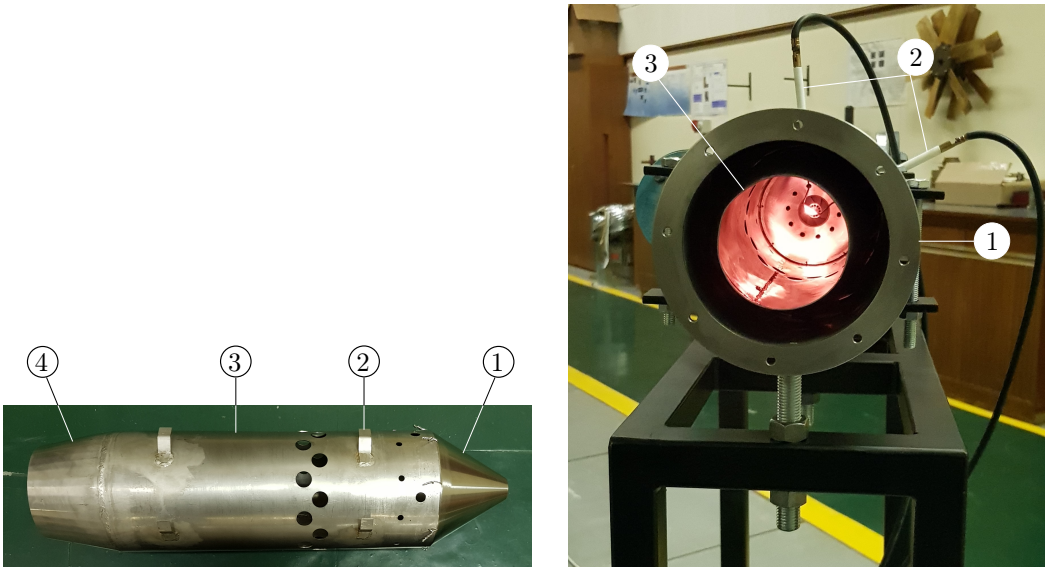

(a) (b)

Figure 4.6: Manufactured combustion chamber; (a) Flame tube assembly; 1. Snout, 2. Metal strip, 3. Flame tube, 4. Nozzle and (b) assembled flame tube fitted inside the casing; 1. Casing, 2. Electrodes, 3. Flame tube

Struwig (2013). From the calibration, the bellmouth coefficient of discharge was found to be asymptotic to 1, as expected. Struwig further generated an exponential correlation between the bellmouth coefficient of discharge C and the throat diameter Reynolds number $Re_{d,bm}$ (see Equation 4.16).

Pressure transducers

The static gauge pressure at the upstream tap of the Venturi tube, the differential pressure across the Venturi tube, as well as the differential pressure across the orifice meter downstream of the low-pressure compressor (orifice 2) were all measured using Endress+Hauser Deltabar M PMD55 differential pressure transducers. The differential pressure across the bellmouth was measured using an Endress+Hauser Deltabar S PMD75 pressure transducer. On the other hand, the static absolute pressure at the gas-generator compressor outlet, the low-pressure compressor outlet, and the combustion chamber outlet, as well as the ambient pressure were all measured using HBM P8AP/10 bar absolute pressure transducers, wired to HBM AE301 Clip amplifiers. These amplifiers were configured for maximum measurement resolution, for the expected pressure measurement range.

All the pressure transducers generated an analog voltage signal, which was converted to a pressure reading by the data logger, using the corresponding correlations generated from the calibration data. The specifications for all the used pressure transducers are summarised in Table 4.2.

Table 4.2: Pressure transducer specifications

Station		Transducer	Span
Venturi tube	diff	E+H K9007321121	5 - 100 mbar
	diff	E+H KC00A021121	0.15 - 3 bar
Orifice 2	diff	E+H K9006B21121	0.05 - 1 bar
	abs	HBM 173710065	0 - 10 bar
Bellmouth	diff	E+H FB00072109D	0.3 - 30 mbar
2	abs	HBM 173710078	0 - 10 bar
3	abs	HBM 143210119	0 - 10 bar
Ambient	abs	HBM 141410077	0 - 10 bar

Each of the pressure transducers was statically calibrated for its expected pressure measurement range. The calibration procedure for the pressure transducers is discussed in Appendix A.

Temperature sensors

The temperature of the air at the gas-generator compressor inlet was measured using four J-type thermocouples fitted to the protective wire mesh grid attached to the bellmouth. This type of thermocouple consists of a positive iron wire and a negative alumel wire. It is popular and inexpensive, and is commonly used in reducing or neutral atmospheres. It has an applicable measuring range of 0 to 760 °C.

The temperature of the air at the outlet of the gas-generator compressor, that of the compressed air used to start up the MGT system and that at the outlet of the low-pressure compressor was measured using T-type thermocouples. This type of thermocouple consists of a positive copper wire and a negative constantan wire. It offers good stability, and is excellent for low temperature applications in the range of −250 to +340 °C.

The temperature of the combustion gases leaving the combustion chamber was measured using four K-type thermocouples. These thermocouples consist of a positive chromel wire and a negative alumel wire. They are well suited to the adverse conditions of combustion chamber testing, and can accurately measure (within ±5 K accuracy) combustion chamber outlet temperatures of up to 1300 K, if special precautions are taken, such as providing an effective thermal shield and bending the thermocouple probes such that they are parallel with and in the direction of the flow (Saravanamuttoo *et al.*, 2009; Beckwith *et al.*, 1993).

All the thermocouples were assumed to measure static temperature. In reality, they were most likely measuring a recovery temperature, which is somewhere between the static and stagnation temperature, assuming no wall heat transfer.

The thermocouples were all calibrated for their expected temperature measurement range, except the high-temperature K-type. The K-type thermocouples could only safely be calibrated to a maximum temperature of 650 °C, owing to limitations with the set-up of the calibrator. The calibration procedure for the thermocouples is discussed in Appendix A.

Similar to the modeling work, relative humidity (or wet bulb temperature) was not considered for the experimental work.

Speed sensors

The rotational speeds of the gas generator and the power turbine were measured using Micro-Epsilon turboSPEED DZ140 speed sensors [model number 4150028, serial numbers 4994 & 4634]. For the gas generator, the speed sensor was mounted in the volute of the gas-generator compressor, while for the power turbine, the speed sensor was mounted in the volute of the low-pressure compressor.

The speed sensors use the eddy-current measuring principle, where a coil housed within a proximity sensor is energized by a high frequency alternating current. The electromagnetic field from the coil generates eddy current in a passing-by turbocharger blade, resulting in the blade generating a pulse. The controller then determines the rotational speed (analog 0 to 5 V), based on the specified number of blades (Micro-Epsilon, 2014).

The mode (speed, sensitivity and test signal) and number of blades can be set on the speed sensors. A mode of 5 (low sensitivity) and a blade number of 14 was set on the controllers of both speed sensors, the latter to guarantee the best immunity to interference, while the former is the number of blades on either compressor impeller. The selected mode also corresponded to a rotational speed measuring range of 200 to 200 000 rpm.

The speed sensors required an input DC voltage of 9 to 30 V (set to 24 V). This voltage was supplied by a Metronix 545B regulated DC power supply.

4.1.3 Fuel supply system

The MGT system runs on propane. The fuel supply system consists of a Venturi tube differential pressure class meter connected in line with an electropneumatically controlled DN10 Condor stainless steel flow control ball valve (valve 5), with the latter downstream of the former (see Figure 4.7), as suggested by the ASME PTC 22 Standard. The Venturi tube was manufactured from brass, and care was taken to smoothly finish it on the inside.

The static pressure of the fuel was measured at the flow meter, on the upstream side of the flow meter, also as suggested by the ASME PTC 22 Standard. Similarly, the static temperature of the fuel was measured upstream of the flow meter, right before the metering run pipe, to avoid disturbing the flow profile.

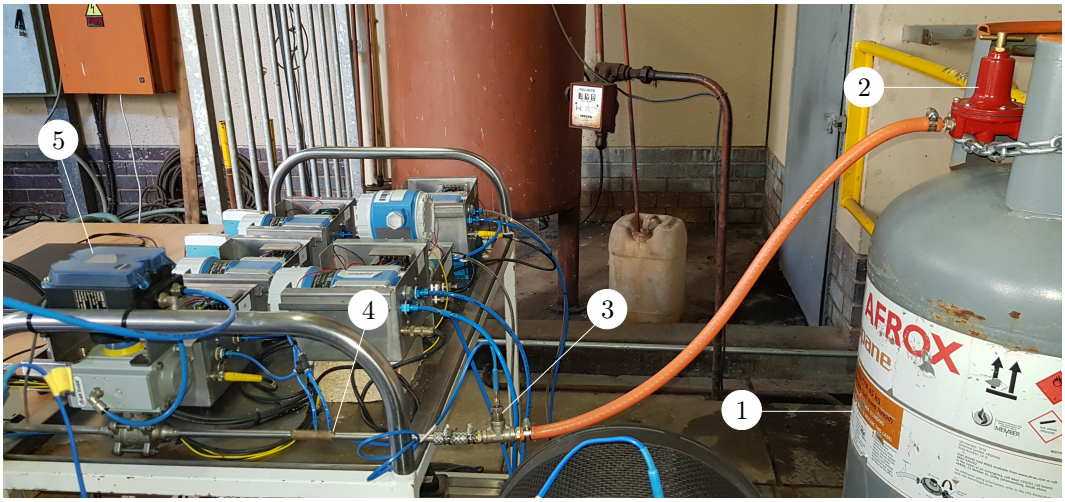

Figure 4.7: Fuel supply system; 1. Fuel, 2. High-pressure regulator, 3. Temperature tap, 4. Flow meter, 5. Valve 5

The fuel was stored in a 45 kg gas cylinder, and the fuel supply pressure was regulated using a CF103 high-pressure regulator fitted to the cylinder. This pressure regulator has a gauge pressure operating range of 0 to 200 kPa.

During the commissioning of the MGT system, it was observed that the fuel flow increased with increasing fuel supply pressure. The fuel supply pressure was therefore set to the maximum possible value of 200 kPa, for all the MGT system test runs.

The ignition of the air/fuel mixture in the combustion chamber was achieved using two 10 mm OD ceramic ignition electrodes, fitted within the combustion chamber primary zone, and positioned 70° circumferentially relative to each other, and with their tips at the centerline of the flame tube (see Figure 4.6b). There is no definitive guideline on the optimum air gap between the electrode tips. From the preliminary testing of the operability of the electrodes, an air gap of 5 mm was found sufficient.

The location of the electrodes within the primary zone was to ensure that the hot kernel of gas created by the ignition spark is returned upstream by the flow recirculation, thus improving mixing and combustion. The electrodes required an input voltage of 240 V, which was supplied by a Fida 26/30 100 % duty cycle ignition transformer.

4.1.4 Lubrication system

A lubrication system designed and built by Nieuwoudt (1987) was employed to lubricate, and cool the bearings of the two turbochargers on which the MGT system is based. Both these turbochargers have a set of twin hydrodynamic journal bearings and end thrust bearings.

The lubrication system consists of a gear pump capable of delivering an oil mass flow rate of 16 l/min, at a rotational speed of 1460 rpm. The pump is driven by a 0.75 kW/5A rated motor. The type of lubrication oil used was 15W40 multigrade diesel engine oil. This oil was stored in a 20 litre tank, fitted with both an oil supply line and an oil return line. A 2 kW low-intensity electric heating element is fitted through the side of the oil tank, to heat the supply oil to a temperature and viscosity suitable for optimal lubrication. The oil supply temperature is manually set using a thermostat. Two T-type thermocouples are fitted into the oil tank, one on the oil supply side and the other on the oil return side. The temperature measurements taken at these two locations are monitored during operation, to ensure a uniform oil temperature throughout the lubrication system. The oil supply pressure is set by throttling a flow control valve, using a knob fitted to the control panel of the lubrication system. The oil supply pressure is displayed using an analog pressure gauge, similarly fitted to the control panel of the lubrication system. The final component on the lubrication system is a bypass valve, which is used to circulate the heated oil through the lubrication system, without passing it through the turbocharger, until the right oil supply temperature is achieved.

Because the lubrication system was designed to lubricate a single turbocharger, it had to be modified, to make it suitable for use with the MGT system. Information on the lubrication requirements for the two turbochargers was obtained from the OEM (see Figure 4.8). The smaller K31 turbocharger has a lower oil volumetric flow rate requirement than the much bigger K44 turbocharger, for the same oil supply temperature and pressure.

Modifications to the lubrication system included adding a second oil supply line, and another oil return line. A throttling valve was also added to the oil supply line of the K31 turbocharger, to ensure a lower oil mass flow rate to it, in comparison to that of the K44 turbocharger. An analog pressure gauge was additionally fitted at the inlet of the bearing housing unit of the K31 turbocharger. A positive pressure reading at this location indicated that the bearing unit of this turbocharger was being lubricated, regardless of the constriction introduced by the throttling valve.

The lubrication system isn't equipped with an oil flow meter. In order to verify that the bearing housing units of the two turbochargers were receiving sufficient oil, at a given oil supply gauge pressure and temperature, rudimentary flow tests were performed. For varying oil supply gauge pressures and temperatures, lubrication oil was pumped to the bearing housing units of the two turbochargers, and then drained into two transparent 5 litre cans.

From the rudimentary tests, it was observed that an oil supply gauge pressure of 240 kPa – which dropped down to about 200 kPa at the inlet of the bearing housing unit of the K31 turbocharger – and an oil supply temperature of 50 °C ensured a steady supply of lubrication oil to both turbochargers. These conditions were therefore maintained throughout the testing of the MGT system.

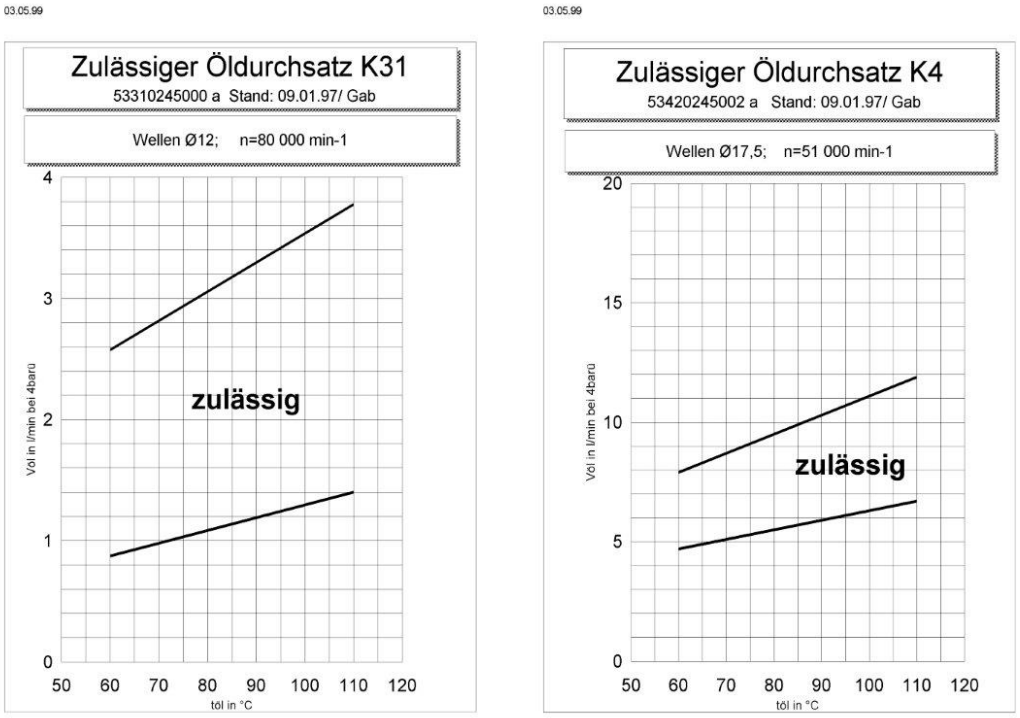

(a) K31 **(b)** K44

Figure 4.8: Lubrication requirements for the turbochargers (Heuer, 2016)

4.1.5 Data acquisition system

The recording of the measurements taken, and the actuation of the flow control valves were achieved using an eight-slot National Instrument CompactDAQ 9172 (NI cDAQ-9172) USB chassis, and seven C Series input/output (I/O) modules inserted in the chassis' slots. The NI cDAQ-9172 chassis has the ability to measure a broad range of analog and digital I/O signals, using a Hi-Speed USB 2.0 interface (National Instruments, 2008).

The measurement sensors and the valve actuators were wired directly to individual channels on the relevant modules. The thermocouples were wired to two NI 9213 analog input (AI) modules with spring-terminal connectors. The NI 9213 is a 24 Bit AI module, with 16 dedicated thermocouple channels. It has a maximum aggregate sampling rate of 75 S/s and an analog voltage signal input range of ± 78 mV. This module can be configured for each type of thermocouple, and it converts the analog voltage signal from the thermocouple into a temperature reading, using built-in polynomial functions. Each determined temperature was then corrected using the linear correlation generated from the calibration of the corresponding thermocouple.

Two of the pressure transducers were wired to an NI 9215 with BNC connectivity AI module, while the other six were wired to an NI 9207E with DSUB

connectivity AI module. The NI 9215 is a 4 channel, 16 Bit AI module, with a maximum simultaneous sampling rate of 100 kS/s, per channel and an analog voltage signal input range of ± 10 V. The NI 9207E is a 16 channel (8 voltage and 8 current), 24 Bit AI module, with an analog voltage and analog current signal input range of ± 10 V and ± 22 mA, respectively. Only the voltage analog input channels of the NI 9207E module were used.

Similar to the pressure transducers, the speed sensors were wired directly to an NI 9215 with screw terminal connectivity AI module. All the AI modules were configured to read 10 samples, at a rate of 1 kHz, while the AO modules were configured to generate 1 sample, on demand.

The host computer was a Lenovo B560 laptop, which was connected to the NI cDAQ-9172 chassis via a USB cable. LabVIEW 2015 and NI-DAQmx software was installed on the laptop. The latter was used to access all the analog I/O channels that were in-use, while the former was used to build a user interface to operate the experimental MGT system, as well as take the required measurements. LabVIEW displays two windows; the front panel and the block diagram. The front panel is the user interface, and it consists of controls and indicators. The block diagram consists of virtual instruments (VI)s and structures that use written code to control the front panel objects.

The AI/O module channels were configured to either acquire or generate analog signals using DAQ Assistant Express VIs on the block diagram. These VIs were also used to convert acquired analog signals from the different sensors to measurements of performance parameters. The MGT system was operated, and the taken measurements were displayed in real-time using front panel containers. Snippets of the built block diagram (see Figure B.1) and the front panel containers (see Figures B.2a to B.2e) can be found in Appendix B.

The experimental MGT system test bench is shown in Figure 4.9.

4.2 Experimental procedure

The experimental procedure initially involved determining a suitable start-up procedure for the MGT system. Thereafter, two test runs were performed, to determine the full operating range of the MGT system. The test runs were performed in succession, and on the same day, in order to minimise variation in the test conditions.

The MGT system was started using compressed air supplied by an existing compressed air line. The start-up procedure involved manipulating the flow control valves; valve 1, to regulate the flow of the compressed air used to start the MGT system, valve 2, to prevent the supplied compressed air from imposing a back pressure on the gas-generator compressor, valve 3, to bleed-off pressurised air from the gas-generator compressor until proper combustion is achieved, and valve 5, to regulate the fuel flow.

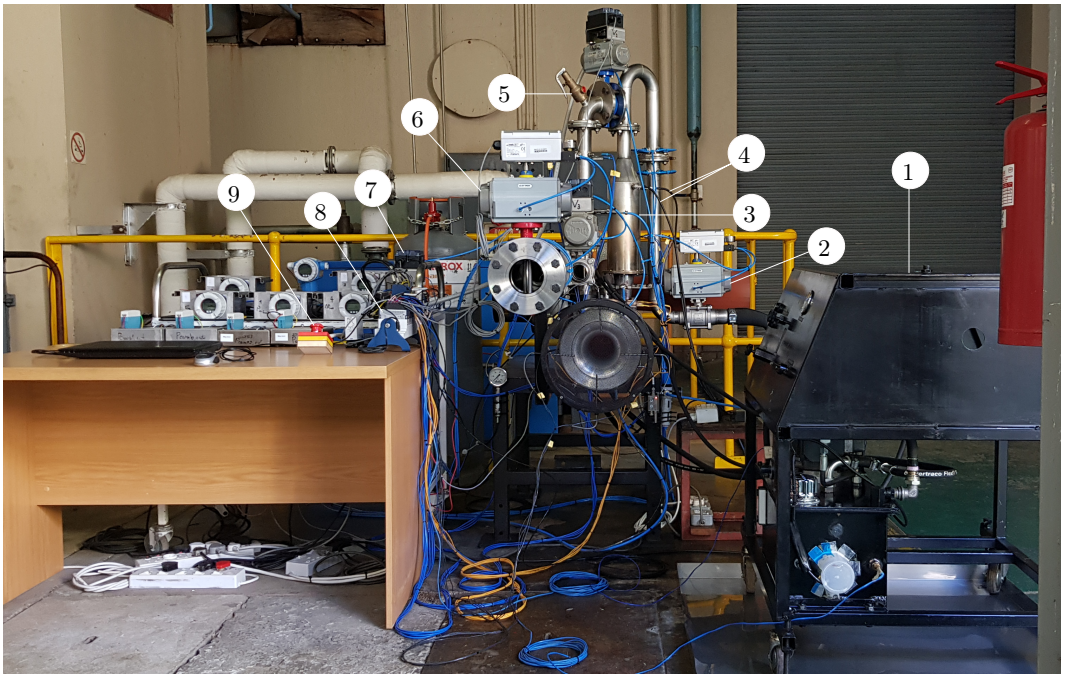

(a) Front view

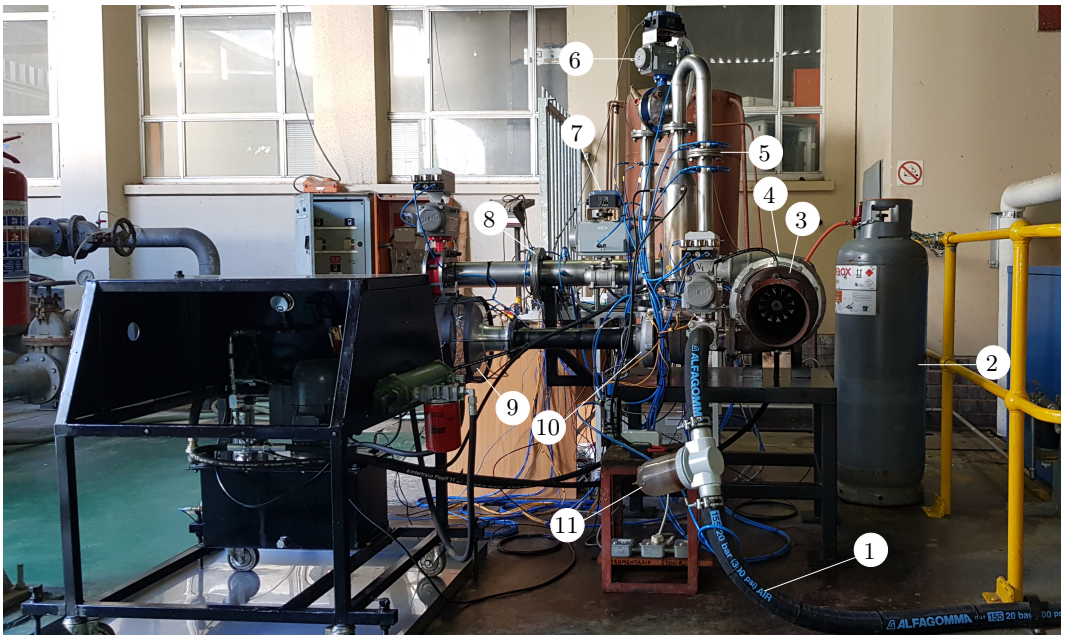

(b) Side view

Figure 4.9: Experimental MGT system test bench; (a) Front view; 1. Lubrication system, 2. Valve 1, 3. Combustion chamber, 4. Electrodes, 5. Safety relief valve, 6. Valve 4, 7. Valve 5, 8. Data logger, 9. Emergency stop push button. (b) Side view; 1. Compressed air supply line, 2. Fuel, 3. Power turbine, 4. Low-pressure compressor, 5. Orifice 1, 6. Valve 2, 7. Valve 3, 8. Orifice 2, 9. Bellmouth, 10. Gas-generator compressor, 11. Air filter

Before the MGT system could be operated, some initial checks had to be performed. These checks included:

- Check that all piping, tubing, fittings and connections are firmly fitted and secure.
- Check that all electrical connections are secure and fully insulated.
- Check that all rotating parts are tightly fastened and fully enclosed by their protective casings.
- Open the labVIEW graphical user interface (GUI), and check that all instrumentation on the test bench is properly functioning.
- Check that all valves are closed, except valves 3 and 4 (see Figures 4.2 and 4.3), which should in this case be fully open. The closed valves include the oil by-pass valve and the compressed air supply main shut-off valve.
- Check that all personal protection equipment (PPE) necessary to perform the experiments is properly worn, and that all the necessary safety signs are in place.

On satisfactory completion of the checks, the proceeding MGT system start-up procedure was followed:

- Switch on the oil pump of the lubrication system, and set the oil supply temperature to 50 °C.
- Once the desired oil supply temperature has been attained, fully open the oil by-pass valve, and set the oil supply gauge pressure to 240 kPa. This ensures the oil circulates through the bearing units of the two turbochargers. Keep monitoring the oil supply and return temperature, as well as the oil supply pressure, and ensure the pre-set values are maintained.
- Set the valve actuation gauge pressure to 6 bar, and fully open valve 1. Open the main shut-off valve on the compressed air line, and gradually increase the mass flow rate of the compressed air until a gas-generator compressor rotational speed of 15 000 rpm is achieved. Keep monitoring the oil supply and return temperature, as well as the oil supply pressure.
- Switch on the power supply to the electrodes, set the fuel supply gauge pressure to 200 kPa, and then gradually open the fuel flow control valve 5, while carefully listening for an indication of successful ignition – generally achieved at a fuel mass flow rate of about 0.002 kg/s
- Quickly close – in increments of about 30 % – valve 3, whilst quickly opening valve 2.

- As soon as valve 3 is fully closed, and valve 2 is fully open, quickly close valve 1. Monitor the combustion, and if necessary add fuel to maintain proper combustion.

Once valves 1 and 3 were fully closed, and valve 2 was fully open, the MGT system was able to run self-sustainably. The MGT system test runs could then be performed.

Performing a test run involved slightly increasing the fuel flow, and after allowing for stabilisation – indicated by the measurement readings displayed on the front panel containers staying constant – recording the taken measurement readings. This process was repeated, varying the degree of opening of the fuel flow control valve each time. The testing range of the MGT system was limited by the maximum allowable turbine inlet temperature stipulated by the turbocharger OEM. The recorded measurements were considered the no-load conditions of the MGT system.

The power turbine was meant to be loaded through gradually throttling the directly coupled low-pressure compressor, using valve 4. For varying degrees of closing of valve 4, the fuel mass flow rate was to be adjusted, until the desired gas-generator no-load speed was attained. Preliminary tests showed that valve 4 would need to be almost closed, to observe a significant change in the gas-generator rotational speed. It was considered un-safe to run the MGT system this way, and therefore the loading of the MGT system was abandoned.

Despite the unsuccessful loading tests, the observed insensitivity of the MGT system to load variation should be advantageous, especially during critical transient situations, such as emergency shutdowns and load shedding. According to Saravanamuttoo *et al.* (2009), the running line for a twin-shaft gas turbine system is independent of the load, and only depends on the swallowing capacity of the power turbine. Owing to its size, the power turbine places minimal flow restriction on the much smaller gas-generator turbine fitted upstream of it, even with the addition of load.

Normal shutdown of the MGT system entailed cutting off the fuel supply by immediately closing Valve 5, quickly opening valve 3, while simultaneously closing valve 2. On completely closing valve 2, and fully opening valve 3, valve 1 was then fully opened, to allow cool air from the compressed air line to cool down the MGT system. The oil supply and return temperature and the oil supply pressure were then monitored, and once the pre-set values were reached, the compressed air was shut-off and the oil lubrication pump was switched off, signalling the end of a test run.

4.3 Measured and calculated parameters

In order to characterise the performance of the MGT system, some primary measurements of physical quantities, such as pressure, temperature and rota-

tional speed had to be taken. Typical MGT system performance parameters, such as the gas-generator TIT, air and fuel mass flow rates, useful work output, specific fuel consumption and cycle thermal efficiency were then calculated from these measurements. Similar to the modeling calculations, ambient stagnation conditions were assumed at the inlet of both the gas-generator compressor and the low-pressure compressor.

The air mass flow rate through the gas-generator compressor was calculated from the measured ambient pressure, the mean air temperature measured at the inlet of the bellmouth, and the measured differential pressure across the bellmouth.

Firstly, the bellmouth throat diameter Reynolds number $Re_{d,bm}$ was calculated, using

$$Re_{d,bm} = \frac{\rho V_{bm} d}{\mu} \tag{4.13}$$

where ρ is the density of the air sucked through the bellmouth, and was calculated from the measured ambient pressure and mean air temperature at the inlet of the bellmouth, using the ideal-gas equation of state. V_{bm} is the air velocity, and was approximated using

$$V_{bm} \approx \left[\frac{2\Delta P}{\rho\left(1-\beta^4\right)}\right]^{0.5} \tag{4.14}$$

where ΔP is the measured differential pressure across the bellmouth and β is the bellmouth throat to pipe diameter ratio d/D, with $D \gg d$.

The term μ in Equation 4.13 is the dynamic viscosity of the air sucked through the bellmouth, and was calculated using the following expression generated from ideal-gas property data for air, found in Cengel and Cimbala (2010)

$$\mu = 7 \times 10^{-15} T^3 - 3 \times 10^{-11} T^2 + 7 \times 10^{-8} T + 3 \times 10^{-7} \tag{4.15}$$

where T is the mean air temperature measured at the inlet of the bellmouth.

The coefficient of discharge C of the bellmouth was then calculated as a function of the bellmouth throat diameter Reynolds number $Re_{d,bm}$, using the following exponential function suggested by Struwig (2013)

$$C = e^{\frac{-1500}{Re_{d,bm}}} \tag{4.16}$$

with the air mass flow rate through the gas-generator then calculated using the general equation for the mass flow rate through a differential pressure class meter

$$\dot{m} = \frac{\pi}{4} d^2 C \epsilon \sqrt{\frac{2\rho\Delta P}{1-\beta^4}} \tag{4.17}$$

where ϵ is the expansion factor, and was assumed to equal to unity (Struwig, 2013).

The fuel mass flow rate was similarly calculated using the general equation for the mass flow rate through a differential pressure class meter (Equation 4.17). From the calibration of the Venturi tube flow meter (see Appendix A.3), the coefficient of discharge was found to be approximately equal to unity. The expansion factor of the Venturi tube flow meter was calculated using (ASME PTC 19.5, 2004)

$$\epsilon = \left[r^{2/\gamma} \left[\frac{\gamma}{\gamma - 1} \right] \left[\frac{1 - r^{(\gamma-1)/\gamma}}{1 - r} \right] \left[\frac{1 - \beta^4}{1 - \beta^4 r^{2/\gamma}} \right] \right]^{0.5} \tag{4.18}$$

where r is the ratio of the static pressure at the downstream tap of the Venturi tube flow meter, to that measured at the upstream tap, with the former calculated as the difference between the latter, and the measured differential pressure across the Venturi tube. β is the venturi tube throat to pipe diameter ratio d/D, with the change in both d and D due to thermal expansion or contraction – resulting from changing flow conditions – considered negligible. γ is the specific heat ratio of propane gas, and was calculated using Equation 3.44, with the mean ideal-gas specific heat at constant pressure of propane (in kJ/kmolK) calculated using the following third-order polynomial approximation suggested by Cengel and Boles (2011)

$$c_p = 31.74 \times 10^{-9} T^3 - 15.72 \times 10^{-5} T^2 + 30.48 \times 10^{-2} T - 4.04 \tag{4.19}$$

where T is the measured supply temperature of the propane.

The density of the propane (in Equation 4.17) was calculated from the static pressure measured at the upstream tap of the Venturi tube and the measured supply temperature of the propane, using the ideal-gas equation of state.

The air mass flow rate through the low-pressure compressor coupled to the power turbine and that of the compressed air used to start the MGT system were measured using D and $D/2$ tap orifice meters. These mass flow rates were similarly calculated using the general equation for the mass flow rate through a differential pressure class meter (Equation 4.17).

The ASME PTC 19.5 Standard suggests the following empirical formulation for calculating the coefficient of discharge for D and $D/2$ tap orifice meters

$$C = 0.5959 + 0.0312\beta^{2.1} - 0.1840\beta^8 + \frac{0.0390\beta^4}{1 - \beta^4} - 0.01584\beta^3 + \frac{91.71\beta^{2.5}}{Re_D^{0.75}} \tag{4.20}$$

Substituting for the ratio of the orifice bore to pipe diameter β, Equation 4.20 reduced to

$$C = 0.6069 + \frac{32.9610}{Re_D^{0.75}} \tag{4.21}$$

for the orifice meter used to measure the air mass flow rate of the compressed air used to start the MGT system (orifice 1), while that for the orifice meter

installed downstream of the low-pressure compressor (orifice 2) reduced to

$$C = 0.6069 + \frac{37.3164}{Re_D^{0.75}} \tag{4.22}$$

where Re_D is the pipe diameter Reynolds number, and was given by

$$Re_D = \frac{4\dot{m}}{\pi D \mu} \tag{4.23}$$

Similarly, the ASME PTC 19.5 Standard suggests the following expression for calculating the expansion factor for orifice meters

$$\epsilon = 1 - \left(0.41 + 0.35\beta^4\right) \frac{\Delta P}{\gamma P} \tag{4.24}$$

Substituting for β, Equation 4.24 reduced to

$$\epsilon = 1 - 0.4781 \frac{\Delta P}{\gamma P} \tag{4.25}$$

for orifice 1, while that for orifice 2 reduced to

$$\epsilon = 1 - 0.4930 \frac{\Delta P}{\gamma P} \tag{4.26}$$

where ΔP is the measured differential pressure across the orifice meter, while P is the static pressure measured at the upstream tap of the orifice meter.

The coefficient of discharge for the orifice meters was obtained iteratively. A value of 0.6 was initially guessed, and a corresponding mass flow rate was calculated (using Equation 4.17). From the calculated mass flow rate, a Reynolds number was then calculated. From the calculated Reynolds number, a new coefficient of discharge was calculated (using Equations 4.21 and 4.22), and compared to the initial guess. This iterative process was repeated, until the difference between successive calculated coefficients of discharge was less than 0.0001, signifying that convergence of the coefficient of discharge, and the corresponding mass flow rate had been achieved.

Code was written in the block diagram, firstly, to convert all the acquired analog signals from the sensors to measurement readings, and then, to perform all the aforementioned calculations (see Figure B.1). The iteration for the coefficient of discharge was achieved using a feedback node loop. Information on all the other measured and calculated parameters was only passed out of the loop, and written to an Excel® *.xlsx* file for post processing, after convergence of the coefficients of discharge for the two orifice meters had been achieved.

The post processing involved averaging the obtained test data, and determining the corresponding standard deviation, for every degree of opening for the fuel flow control valve (valve 5). Each degree of opening for the fuel

flow control valve also corresponded to a test point for the MGT system. The averaged test data was used to determine the equilibrium running point for the experimental MGT system; characterised by parameters such as the gas-generator compressor total-to-total pressure ratio, non-dimensional mass flow rate and speed, and total-to-total isentropic efficiency. From the obtained equilibrium running point, the corresponding MGT system performance parameters such as the gas-generator TIT, specific fuel consumption, useful work output and cycle thermal efficiency were determined.

The gas-generator compressor total-to-total pressure ratio P_{02}/P_{01} was calculated from the absolute static pressure and the mean static temperature measured at the outlet of the gas-generator compressor, in addition to the measured ambient pressure – assuming a negligible non-recoverable pressure loss downstream of the bellmouth. From the absolute static pressure measured at the outlet of the gas-generator compressor P_2, the total pressure at the outlet of the gas-generator compressor P_{02} was calculated using the ideal-gas isentropic relation between pressure and temperature ratios, as given by

$$P_{02} = P_2 \left(\frac{T_{02}}{T_2} \right)^{\gamma_a/(\gamma_a - 1)} \tag{4.27}$$

with the total temperature at the outlet of the gas-generator compressor T_{02} calculated from the mean static air temperature measured at the outlet of the gas-generator compressor T_2, using

$$T_{02} = T_2 + \frac{V_2^2}{2c_{p,a}} \tag{4.28}$$

where V_2 is the air velocity at the outlet of the gas-generator compressor, and was calculated from the one-dimensional, steady-flow mass balance expression

$$V_2 = \frac{4\dot{m}_a R T_2}{P_2 \pi d_2^2} \tag{4.29}$$

where $\dot{m}_a$ is the air mass flow rate through the gas-generator compressor, and d_2 is the pipe diameter at the outlet of the gas-generator compressor.

The non-dimensional mass flow rate of the gas-generator compressor $\dot{m}\sqrt{T_{01}}/P_{01}$ was calculated from the determined air mass flow rate through the gas-generator compressor, and the measured ambient pressure and the mean air temperature at the inlet of the bellmouth.

The gas-generator compressor non-dimensional speed $N/\sqrt{T_{01}}$ was calculated from the measured gas-generator compressor rotational speed and the mean air temperature at the inlet of the bellmouth.

The total-to-total isentropic efficiency of the gas-generator compressor was calculated from the determined gas-generator compressor pressure ratio, the mean air temperature at the inlet of the bellmouth, and the temperature rise in the gas-generator compressor, using Equation 3.29.

The stagnation gas-generator TIT T_{03} was determined from the mean static temperature measured at the outlet of the combustion chamber T_3, using

$$T_{03} = T_3 + \frac{V_3^2}{2c_{p,g}} \tag{4.30}$$

where $c_{p,g}$ is the specific heat at constant pressure of the combustion gases, and was calculated using Equation 3.45. V_3 is the velocity of the combustion gases at the outlet of the combustion chamber, and was calculated from

$$V_3 = \frac{4\left(\dot{m}_a + \dot{m}_f\right) RT_3}{P_3 \pi d_3^2} \tag{4.31}$$

The useful work output of the power turbine was determined indirectly, as the power absorbed by the low-pressure compressor directly coupled to it (see Section C.4). This indirect method was chosen for this study, because the K44 turbocharger on which the power turbine is based was supplied with a compressor. However, this indirect method is less accurate than direct methods, such as, coupling the power turbine to either a dynamometer or a generator, and either directly measuring the torque exerted onto these devices by the power turbine or directly measuring the electrical power at the generator terminals (Brun and Nored, 2009).

The power absorbed by the low-pressure compressor was given by

$$\dot{W}_c = \dot{m}_a c_{p,a} \left(T_{08} - T_{07}\right) \tag{4.32}$$

where T_{08} is the stagnation temperature at the outlet of the low-pressure compressor, and was calculated from the mean static temperature measured at the outlet of the low-pressure compressor, using

$$T_{08} = T_8 + \frac{V_8^2}{2c_{p,a}} \tag{4.33}$$

with the air velocity at the outlet of the low-pressure compressor V_8 calculated using

$$V_8 = \frac{4\dot{m}_a RT_8}{P_8 \pi d_8^2} \tag{4.34}$$

where $\dot{m}_a$ is the air mass flow rate through the low-pressure compressor, and d_8 is the pipe diameter at the outlet of the low-pressure compressor.

T_{07} is the stagnation temperature at the inlet of the low-pressure compressor. This temperature was assumed to be equal to the mean ambient temperature measured at the inlet of the gas-generator compressor. In addition, Equation 4.32 assumes an adiabatic compression process.

The specific fuel consumption of the MGT system was calculated from the determined useful work output of the power turbine, and the calculated fuel mass flow rate, using Equation 3.59.

The total cycle thermal energy input was calculated using Equation 3.55, while the cycle thermal efficiency was calculated using Equation 3.60.

To ensure aerodynamic similarity between the predicted and the experimentally determined performance, the performance parameters of the experimental MGT system were corrected to standard ISO reference conditions of pressure P_{ref} and temperature T_{ref} of 101.325 kPa and 15 °C, respectively (ISO 2314, 2009; Veer *et al.*, 2004). The gas-generator TIT was corrected using

$$T_{03,corr} = T_{03}\sqrt{\frac{T_{ref}}{T_{01}}} \tag{4.35}$$

while the air mass flow rate drawn into the gas-generator compressor was corrected using

$$\dot{m}_{a,corr} = \dot{m}_a \left[\frac{P_{ref}}{P_{01}}\right] \sqrt{\frac{T_{01}}{T_{ref}}} \tag{4.36}$$

and the gas-generator compressor rotational speed was corrected using

$$N_{corr} = N\sqrt{\frac{T_{ref}}{T_{01}}} \tag{4.37}$$

Finally, the work output of the power turbine was corrected using

$$\dot{W}_{pt,corr} = \dot{W}_{pt} \left[\frac{P_{ref}}{P_{01}}\right] \sqrt{\frac{T_{01}}{T_{ref}}} \tag{4.38}$$

Gas turbine performance is typically corrected to specified reference conditions, using both multiplicative and additive correction factors. These correction factors are obtained from site specific correction curves supplied by gas turbine manufacturers. The generation of the correction curves though requires extensive testing of the gas turbine systems, at variable ambient conditions.

4.4 Uncertainty analysis

A key requirement in the planning and execution of experiments is to minimise the measurement error. Uncertainty or error analysis is used to estimate a bound on the measurement error, with a defined level of confidence.

Errors can generally be classified as either systematic or random. Systematic errors, also referred to as bias errors, are consistent for each successive measurement. Their lack of distribution means they cannot be analysed using statistical tools. However, they can be estimated using the knowledge of the rated performance (accuracy, resolution, precision, *et cetera*) of the measuring instruments, and how well the instruments were calibrated. In contrast,

random errors, also referred to as precision errors, vary with each successive measurement, showing a distribution about a mean value. They can therefore be estimated using statistical techniques, if enough measurements are taken (Beckwith *et al.*, 1993).

Before the uncertainty bounds could be estimated, the possible sources of error in the measured or calculated MGT system performance parameters had to be identified. The uncertainty analysis considered measured parameters, such as the gas-generator TIT and rotational speed, and calculated parameters, such as the air and fuel mass flow rates.

The uncertainty analysis only considered MGT system performance parameters that could be experimentally determined with reasonable accuracy. The uncertainty limits for the performance parameters that were found to be greatly deviating from the predicted values were ignored (see Table 4.4).

Gas-generator TIT uncertainty

The static temperature of the combustion gases exiting the combustion chamber was measured using four unshielded K-type thermocouples fitted into a stainless steel rectangular flange, with the flange then fitted between the outlet of the combustion chamber and the inlet of the gas-generator turbine. The static gas-generator TIT was determined as the arithmetic mean of the four individual static temperature measurements taken.

Combustion gases at the outlet of a combustion chamber experience spatial variations, including non-uniform temperature and velocity profiles, and varying flow angle and composition (ASME PTC 22, 2014). These spatial variations were a possible source of bias error in the measured static gas-generator TIT.

Furthermore, when an unshielded thermocouple is used within a fast moving gas stream at elevated temperature, the temperature recorded by the hot junction of the thermocouple usually differs from that of the gas stream, owing to radiation and conduction effects. Radiation of heat from the hot flame to the thermocouple junction, and from the junction to the exhaust duct walls or vice versa results in the thermocouple indicating a temperature different to that of the gas stream. Similarly, conduction of heat from the hot thermocouple junction, along the thermocouple probe and through the connecting fittings results in a temperature reading different to that of the gas stream.

The radiation error is highly dependent on the heat transfer coefficient of the thermocouple probe. According to Saravanamuttoo *et al.* (2009), the use of a completely unshielded thermocouple can result in a radiation error of about 60 K, for a temperature measurement of 1300 K. References, such as Bergman *et al.* (2011) give worked examples of how this error can be estimated.

The presence of a thermocouple in a fast moving gas stream also impedes the flow. The lost kinetic energy is converted to heat, which in turn raises the temperature of the thermocouple junction. The resultant temperature

difference between the thermocouple junction and the gas stream can be as high as 200 °C (Beckwith *et al.*, 1993).

It was also noted earlier that the K-type thermocouples could only safely be calibrated to a maximum temperature of 650 °C. This temperature was below the static temperatures actually measured at the combustion chamber outlet during the tests. Therefore, all the temperature measurements had an inherent bias error, resulting from the use of the thermocouples outside their calibration range. The bias uncertainty in the measured static gas-generator TIT was estimated to be equal to ± 0.75 %, which is the measurement uncertainty limit for K-type thermocouples (Beckwith *et al.*, 1993).

The precision uncertainty in the static gas-generator TIT was determined from the sample measurements of static temperature taken, and the corresponding sample mean and standard deviation. The precision uncertainty was reduced by sampling from four static temperature measurement points located in a plane perpendicular to the flow. According to the ASME PTC 22 Standard, uncertainty in the measured temperature of a high-temperature fast moving gas stream can be minimised either by sampling from at least four, and up to sixteen temperature measurement points located in a plane perpendicular to the flow, or by using advanced calculation methods, such as flow/velocity weighting and flow angle compensation. In addition, the use of chromel-alumel (K-type) thermocouples, with proper thermal shielding, and with about 2 to 3 cm of the thermocouple probes bent parallel with and in the direction of flow can reduce the error due to radiation and conduction effects (Saravanamuttoo *et al.*, 2009; Beckwith *et al.*, 1993). To address stagnation effects, it is recommended to use stagnation temperature probes. They are relatively easy to manufacture, and can easily be shielded from the vast majority of viewing angles of the flame portions of the flow.

Gas-generator rotational speed uncertainty

The rotational speed of the gas generator was measured using a Micro-Epsilon turboSPEED DZ140 speed sensor, with a rated linearity of ± 0.2 % of the full scale output (set to 200 000 rpm) (Micro-Epsilon, 2014). The speed sensor was not calibrated, as there was no suitable standard to calibrate it against. The bias uncertainty in the measured rotational speed was therefore assumed to be equal to the linearity rating of the sensor.

The rotational speed was sampled several times, for each test point, with the recorded sample speeds then averaged and the sample standard deviation also determined. The obtained data was used to estimate the precision uncertainty in the measured rotational speed.

Mass flow rate uncertainty

The air and fuel mass flow rates through the MGT system were calculated using the general equation for the mass flow rate through a differential pressure class meter (Equation 4.17). The total uncertainty in the calculated mass flow rates was determined as the root-sum-square of the uncertainty due to bias and precision error, in both the measured and the assigned independent parameters involved in the mass flow rate equation.

For the calculation of the mass flow rate of the air drawn into the gas-generator compressor, the measured independent parameters included the differential pressure across the bellmouth, ambient pressure, the mean static temperature at the inlet of the bellmouth and the pipe and throat diameters of the bellmouth. Assigned independent parameters included the coefficient of discharge and the expansion factor.

The differential pressure across the bellmouth was measured using an Endress+Hauser Deltabar S PMD75 pressure transducer. The manufacturer specifies a total bias error of ± 0.77 % of the upper range limit (30 mbar) for this transducer (Endress+Hauser, 2014). The pressure at the inlet of the bellmouth was assumed to equal to ambient pressure, which was measured using a 0.3 % accuracy class HBM P8AP/10 bar absolute pressure transducer. The static temperature at the inlet of the bellmouth was measured using four J-type thermocouples with a measurement uncertainty limit of 0.6 °C (Beckwith *et al.*, 1993). The thermocouples were fitted circumferentially around the protective wire mesh grid attached to the inlet of the bellmouth, and spaced 90° apart, as suggested by the ASME PTC 22 Standard. The air temperature at the inlet of the bellmouth was calculated as the arithmetic mean of the four individual temperature measurements taken.

To estimate the precision uncertainty in the calculated air mass flow rate, the ambient pressure, the static temperature at the inlet of the bellmouth, and the differential pressure across the throat of the bellmouth were sampled several times for each test point, with the precision uncertainty then estimated from the determined sample mean and standard deviation.

The bellmouth throat and pipe diameters were measured using a vernier caliper with a linear analog readout scale. The diameters were measured once-off, with the obtained values then used for every subsequent air mass flow rate calculation. Therefore, error in the measurement of the diameters contributed to bias uncertainty in the calculated gas-generator compressor air mass flow rate. This bias uncertainty was assumed to be ± 0.1 mm. The change in the diameters due to thermal expansion or contraction was considered negligible, which could result in precision error in the calculated air mass flow rate.

Similarly, the assigned parameters only contributed to bias uncertainty in the calculated gas-generator compressor air mass flow rate. The bias uncertainty in the calculated discharge coefficient was estimated as ± 1 %, a value suggested by ASME PTC 19.5 (2004) for low β nozzles. The ASME PTC 19.5

Standard similarly suggests determining the bias uncertainty in the calculated expansion factor using $^{4\Delta P}/_{P}$, expressed as a percentage.

For the calculation of the fuel mass flow rate, the measured independent parameters included the differential pressure across the throat of the Venturi tube, static gauge pressure and temperature at the inlet of the Venturi tube and the pipe and throat diameters. Assigned independent parameters included the coefficient of discharge and the expansion factor.

The differential pressure across the throat of the Venturi tube, and the static gauge pressure at the inlet of the Venturi tube were both measured using Endress+Hauser Deltabar M PMD55 differential pressure transducers, with total bias errors ± 0.39 % of the upper range limit (100 mbar) and ± 0.18 % of the upper range limit (3 bar), respectively (Endress+Hauser, 2016). The static temperature at the inlet of the Venturi tube was measured using a single T-type thermocouple, with a measurement uncertainty limit of 0.6 °C (Beckwith *et al.*, 1993).

Similar to the bellmouth, the venturi tube pipe and throat diameters were measured once-off, using a vernier caliper with a linear analog readout scale. Therefore, the bias uncertainty in the measured diameters was assumed to be ± 0.1 mm.

For the assigned parameters, the bias uncertainty in the calculated discharge coefficient was estimated as ± 0.70 %, a value suggested by ASME PTC 19.5 (2004) for an uncalibrated Venturi tube. The bias uncertainty in the calculated expansion factor was similarly given by $^{4\Delta P}/_{P}$, expressed as a percentage.

To estimate the precision uncertainty in the calculated fuel mass flow rate, the static pressure and temperature at the inlet of the Venturi tube, and the differential pressure across the throat of the Venturi tube were sampled several times for each test point, and the precision uncertainty was estimated from the determined sample mean and standard deviation.

The preceeding analysis is implemented in Section C.3. The applied equations were adapted from ASME PTC 19.1 (2006), and are similarly presented in the same Section.

4.5 Experimental results and analysis

4.5.1 Experimental validation

To validate the predicted performance of the MGT system against the experimentally determined performance, the developed standard MGT system model presented in Chapter 3 had to be modified in two aspects; the combustion chamber pressure drop model and the considered ambient conditions. The combustion chamber pressure drop was modeled based on the actual pressure

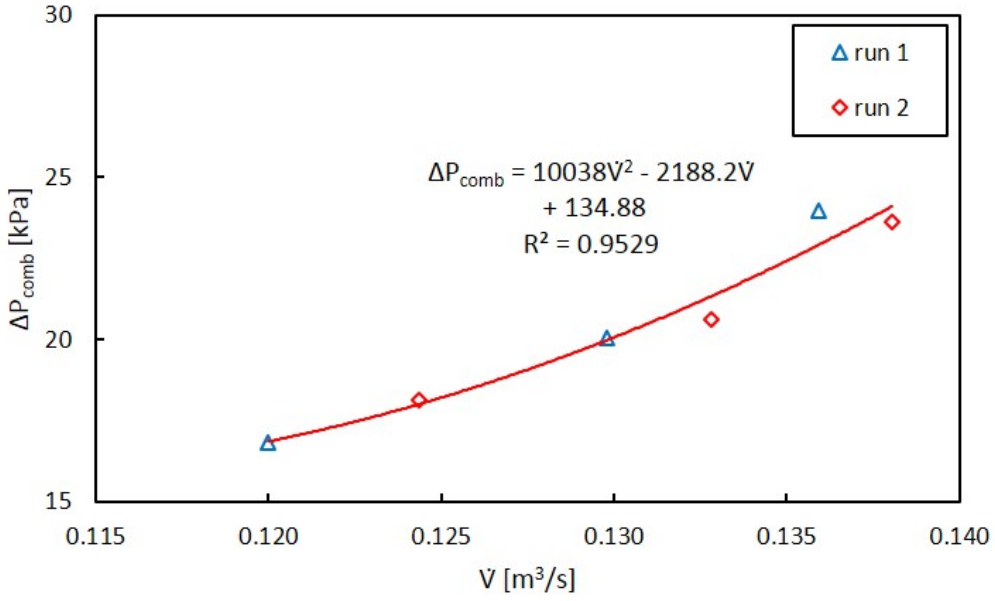

Figure 4.10: Pressure drop across the combustion chamber vs inlet volume flow rate

drop measured across the combustion chamber during the testing of the MGT system.

A second-order polynomial curve was fitted through a plot of the measured pressure drop (in kPa) across the combustion chamber against the corresponding volume flow rate at the inlet of the combustion chamber (see Figure 4.10), with the following function obtained for the curve-fit

$$\Delta P_{comb} = 10038\dot{V}^2 - 2188.2\dot{V} + 134.88 \tag{4.39}$$

This function was used to model the pressure drop across the combustion chamber. It accounts for the hot flow pressure losses, as well as the minor pressure losses caused by components, such as the 90° bend, valve 2 and the equal tee-piece, all fitted between the outlet of the gas-generator compressor and the inlet of the combustion chamber.

In addition, standard ISO reference conditions of ambient pressure and temperature (101.325 kPa and 15 °C) were implemented in the model. This allowed a comparison of performance for the same test conditions.

The predicted equilibrium running point – after implementing the new curve-fit correlation for the combustion chamber pressure drop, and considering standard ISO reference conditions of ambient pressure and temperature – was plotted on the compressor characteristic, as shown in Figure 4.11. In addition, the experimentally determined equilibrium running points for the two performed test runs were plotted on the same figure. These equilibrium

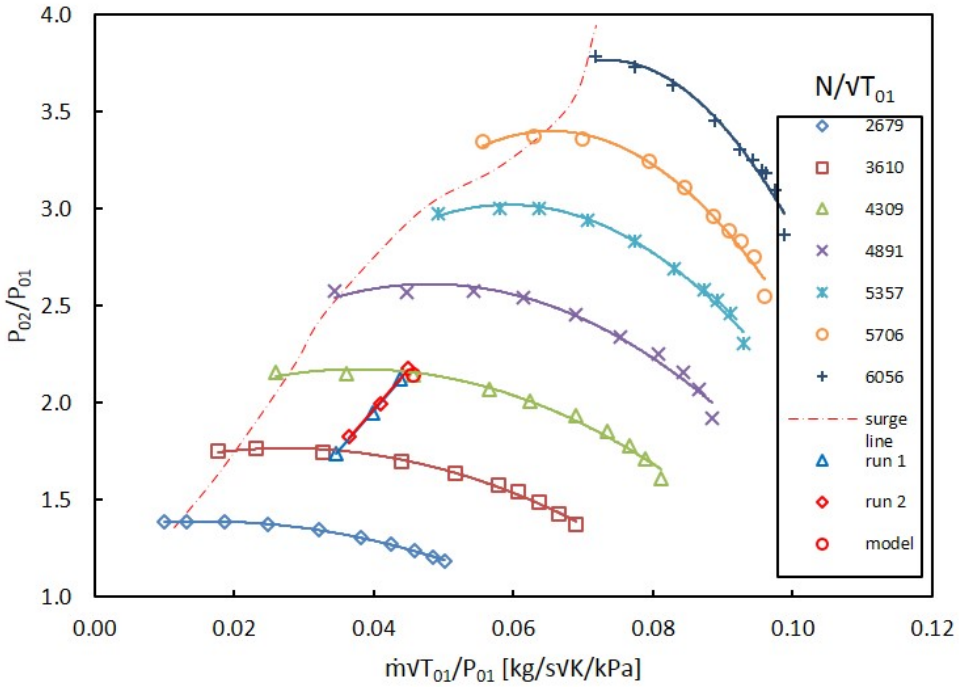

Figure 4.11: Experimental MGT system equilibrium running points

running points were further joined to form equilibrium running lines for either test run.

The generated equilibrium running lines are closely matched, proving the repeatability of the performed tests. The predicted equilibrium running point lies on the 4309 non-dimensional compressor speed line, and closely matches the third, and final equilibrium running point on either equilibrium running line (see Table 4.3). These equilibrium running points correspond to the best MGT system performance, and thus the predicted equilibrium running point can be considered the optimum MGT system operating point. However, the component matching was performed based on discrete points on each speed line on the compressor characteristic. Therefore, the predicted equilibrium running point is only the optimum of these discrete points, and not necessarily the optimum overall.

The shift in the equilibrium running points in Figure 4.11, in comparison to Figure 3.7 is because the equilibrium running points plotted on the former accounted for the physical set up of the experimental MGT system, while those plotted on the latter were obtained from component models and performance characteristics found in literature.

The disparity between the predicted and the actual gas-generator compressor total-to-total isentropic efficiency shown in Table 4.3 results from the assumption of an adiabatic compression process during the modeling, which wasn't the case for the experiments. The lack of insulation around the gas-

Table 4.3: Comparison of MGT system equilibrium running point parameters

Parameter	Value		
	Predicted	Experimental	
		run 1	run 2
P_{02}/P_{01}	2.1	2.1	2.2
$\dot{m}\sqrt{T_{01}}/P_{01}$ [kg/s$\sqrt{\text{K}}$/kPa]	0.0458	0.0437	0.0449
$\eta_{c,t-t}$ [%]	77	73	72
$N/\sqrt{T_{01}}$ [rpm/$\sqrt{K}$]	4309	4302	4378

Table 4.4: Predicted vs experimental performance parameters

Parameter	Value				
	Predicted	Experimental			
		run 1	Deviation [%]	run 2	Deviation [%]
N [rpm]	73144	73027	0.2	74309	2
$\dot{m}_a$ [kg/s]	0.273	0.261	4	0.268	2
$\dot{m}_f$ [kg/s]	0.0042	0.0043	2	0.0045	7
T_{03} [°C]	714	839	18	849	19
$\dot{W}_{pt}$ [kW]	13.6	6.5	52	7.9	42
SFC [kg/kWh]	0.0011	0.0024	118	0.0021	91
η_{th} [%]	7	3	57	4	43

generator compressor volute and the connecting ducts resulted in heat losses to the surroundings, increasing the power absorbed by the gas-generator compressor, and resulting in a lower isentropic efficiency. The lower isentropic efficiency could also have been a result of the dissipated energy ending up in the compressed air stream, as well as mechanical losses due to bearing friction and windage.

The MGT system performance parameters corresponding to the matching predicted and experimental equilibrium running points – with the performance parameters corresponding to the latter corrected to standard ISO reference conditions, wherever applicable – are summarised in Table 4.4. There is a close match between the predicted and the realised rotational speed, and air and fuel mass flow rates. In contrast, discrepancies are observed between the predicted and the realised gas-generator TIT, useful work output, specific fuel consumption and cycle thermal efficiency.

The discrepancy between the predicted and the actual gas-generator TIT is attributed to the use of unshielded thermocouples, which resulted in radiation and conduction error in the measured temperature of the combustion gases leaving the combustion chamber, as discussed in Section 4.4. Measurement error due to spatial variations experienced by the combustion gases at the outlet of the combustion chamber, as well as calibration and stagnation error are other possible sources for the discrepancy between the predicted and the

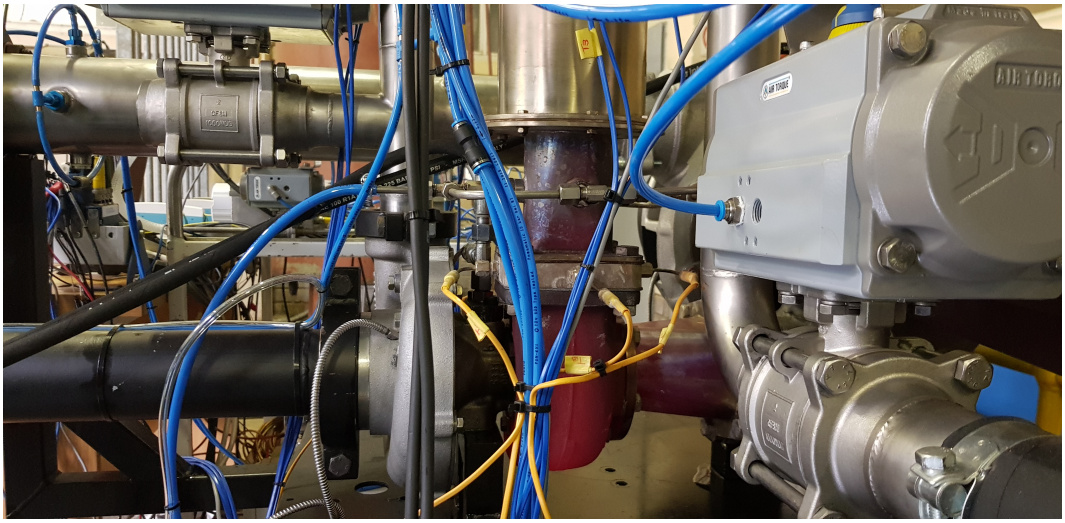

Figure 4.12: An example of an uninsulated section susceptible to heat losses

actual gas-generator TIT.

About half of the predicted work output – and consequently half of the predicted cycle thermal efficiency – was actually realised. The modeling assumed an adiabatic expansion process in both the gas-generator turbine and the power turbine, which wasn't the case for the experiments. The lack of insulation around the 'hot' sections of the MGT system (see Figure 4.12) resulted in radiation, conduction and convection heat losses to the atmosphere. Because of these heat losses, less thermal energy was available for conversion into useful work output in the power turbine. Studies such as Visser *et al.* (2011) and Visser *et al.* (2012) showed that heat losses contribute a significant fraction of the total system losses – with up to 26.4 % observed, in the case of the former – if proper thermal insulation is not implemented in small gas turbine systems of low power. Other minor system losses include mechanical losses due to bearing friction and windage.

The cycle thermal efficiency is directly proportional to the useful work output (see Equation 3.60), and a reduced useful work output results in a lower cycle thermal efficiency.

The realised specific fuel consumption was about twice that predicted, owing to only half of the predicted work output being realised. Specific fuel consumption is inversely proportional to work output (see Equation 3.59), and a reduced work output results in a higher specific fuel consumption.

For completeness, the effect of ambient temperature on the experimentally determined gas-generator TIT was also analysed. Similar to the predicted standard MGT system performance (see Figure 3.8), the experimentally determined gas-generator TIT increased linearly with ambient temperature, as shown in Figure 4.13. This plot covers the full equilibrium running lines, but the linear trend should similarly hold for a single equilibrium running point.

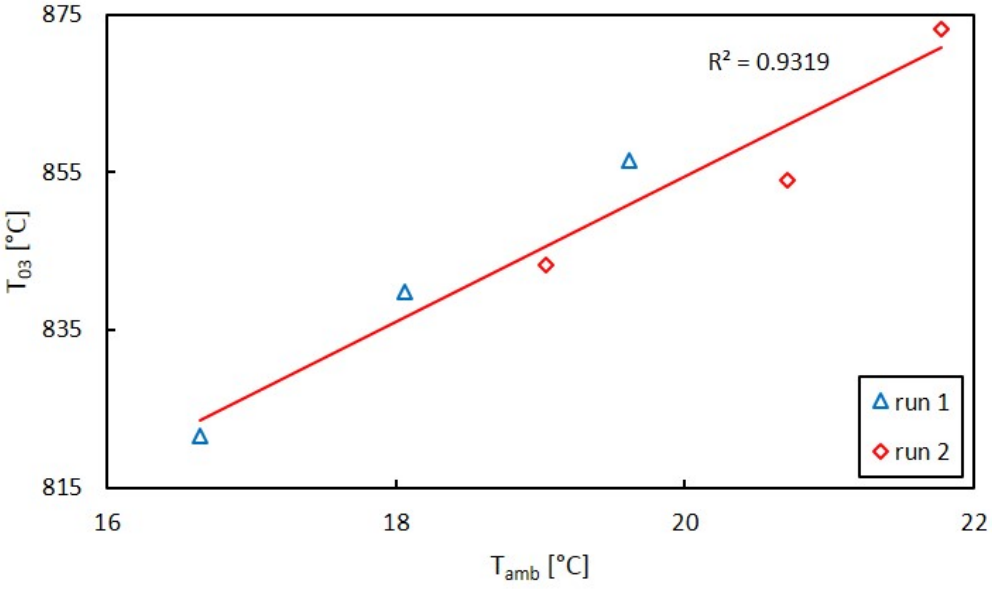

Figure 4.13: Effect of ambient temperature on the experimentally determined gas-generator TIT

It has to be noted though that, the useful work output and cycle thermal efficiency of the standard MGT system, predicted using the combustion chamber pressure drop model developed by Hummel (2014) (Equation 3.1) is of a similar order of magnitude to that predicted using the combustion chamber pressure drop model developed for this study (Equation 4.39), yet the latter additionally accounts for the hot flow and minor pressure losses, and thus predicts a higher combustion chamber pressure drop. Using Hummel's combustion chamber pressure drop model, a pressure loss of 6 % was predicted, corresponding to a nominal useful work output of 12.5 kW and cycle thermal efficiency of 7 %. For the combustion chamber pressure drop model developed in this study, a pressure loss of 11 % was predicted, corresponding to a similar useful work output of 13.6 kW and cycle thermal efficiency of 7 %. This similar performance corresponds to two different equilibrium running points for the standard MGT system (see 'MGT' column in Table 3.1 vs 'Predicted' column in Table 4.3).

The preceding point of note indicates that the theoretical model predicts the most optimum MGT system equilibrium running point, depending on the total system pressure losses, and the need to meet the gas-generator compressor work requirement, while also ensuring a useful work output from the power turbine. But, a very high combustion chamber pressure loss could significantly limit the operating range of the MGT system under solar-hybrid operation, given the solar receiver and the additional air flow path are expected to introduce additional system pressure losses.

Table 4.5: MGT system performance parameters (run 1)

Fuel valve [%]	P_{amb} [kPa]	T_{amb} [°C]	P_{02}/P_{01}	$\dot{m}\sqrt{T_{01}}/P_{01}$ [kg/s$\sqrt{\text{K}}$/kPa]	$\eta_{c,t-t}$ [%]	$N/\sqrt{T_{01}}$ [rpm/$\sqrt{K}$]	$\dot{m}_a$ [kg/s]	$\dot{m}_f$ [kg/s]	ΔP_{comb} [% of P_{02}]	T_{03} [°C]	$\dot{W}_{pt}$ [kW]	SFC [kg/kWh]	η_{th} [%]
53	100.2	17	1.7	0.0346	76	3623	0.204	0.0034	10	822	2.9	0.0043	2
55	100.2	18	1.9	0.0398	74	4002	0.234	0.0039	10	840	4.3	0.0032	3
57	100.2	20	2.1	0.0437	73	4302	0.256	0.0043	12	857	6.4	0.0024	3

Table 4.6: MGT system performance parameters (run 2)

Fuel valve [%]	P_{amb} [kPa]	T_{amb} [°C]	P_{02}/P_{01}	$\dot{m}\sqrt{T_{01}}/P_{01}$ [kg/s$\sqrt{\text{K}}$/kPa]	$\eta_{c,t-t}$ [%]	$N/\sqrt{T_{01}}$ [rpm/$\sqrt{K}$]	$\dot{m}_a$ [kg/s]	$\dot{m}_f$ [kg/s]	ΔP_{comb} [% of P_{02}]	T_{03} [°C]	$\dot{W}_{pt}$ [kW]	SFC [kg/kWh]	η_{th} [%]
54	100.1	19	1.8	0.0365	73	3785	0.214	0.0036	10	843	3.8	0.0034	2
56	100.1	21	2.0	0.0409	72	4085	0.239	0.0040	11	854	5.4	0.0027	3
57	100.1	22	2.2	0.0449	72	4378	0.262	0.0045	11	873	7.7	0.0021	4

A case in point, a surge margin of 37 % was calculated for the equilibrium running point predicted using the combustion chamber pressure drop model developed for this study. This corresponds to a reduction in surge margin of 13 % to that calculated for the equilibrium running point predicted using the combustion chamber pressure drop model developed by Hummel. Although this surge margin is still within typical surge margin limits expected for power and propulsion applications, a further reduction in surge margin is expected for the MGT system under solar-hybrid operation, as was predicted in the theoretical modeling work. The reduction in surge margin will further limit the operating range of the MGT system under solar-hybrid operation.

4.5.2 Experimental performance

The non-corrected performance parameters corresponding to the experimentally determined equilibrium running points are presented in Tables 4.5 and 4.6. The averaged test data obtained from the two performed test runs, for varying degrees of opening of the fuel flow control valve, is presented in Tables C.5 and C.6.

An increase in the fuel mass flow rate resulted in an increase in the useful work output, which in turn corresponded to an increase in both the power turbine rotational speed (see Figure 4.14) and the cycle thermal efficiency, and a subsequent decrease in the specific fuel consumption of the MGT system (see Figure 4.15). However, this improved performance was realised at generally very low cycle thermal efficiencies and high combustion chamber pressure drop.

Insulating the 'hot' sections of the experimental MGT system test bench should reduce the heat losses to the atmosphere, which should increase both the useful work output and the cycle thermal efficiency to levels closer to those predicted. The addition of recuperation should lead to a further increase in the cycle thermal efficiency, as was predicted in the theoretical modeling work.

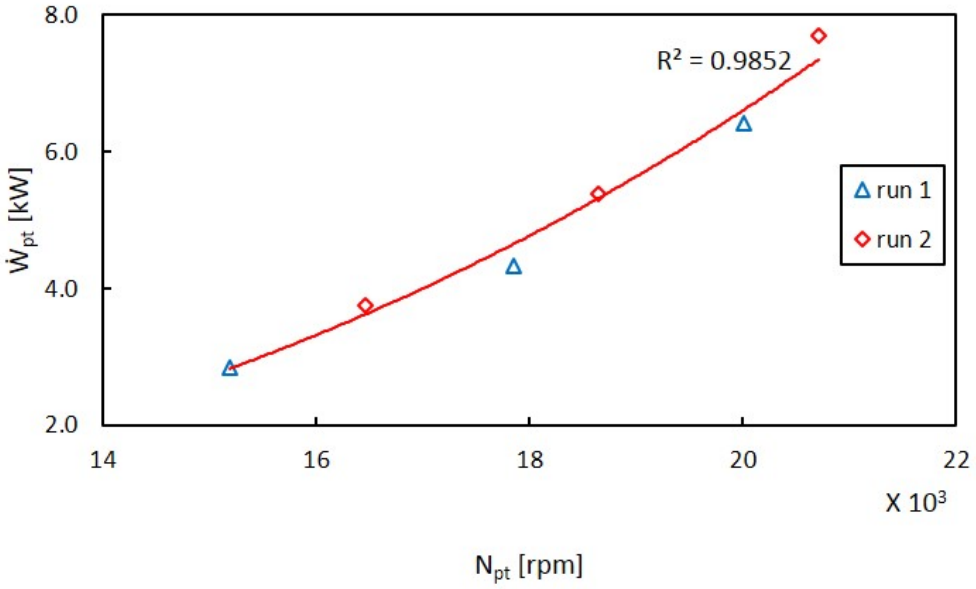

Figure 4.14: Work output vs power turbine rotational speed

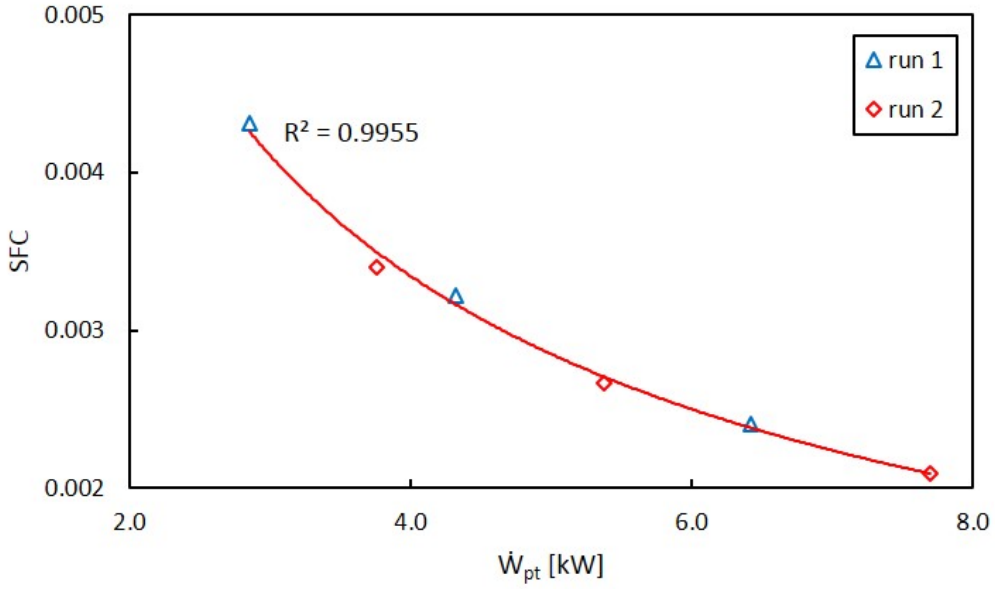

Figure 4.15: *SFC* vs work output

4.6 Adapting the experimental MGT system to solar-hybrid operation

The few demonstrated solar-hybrid gas turbine system projects showed that several operational and control challenges still exist and significant development effort is still required to provide technically proven units. Some of the challenges encountered in adapting gas turbines to solar operation included integrating the solar receiver and the externally heated air into the gas turbine systems and implementing a control system to switch gas turbine operation modes. Other issues experienced included unsuccessful emergency shutdowns and unsatisfactory combustion during micro gas turbine start-up.

4.6.1 System configuration

The experimental MGT system is based on off-the-shelf turbocharger technology. The use of turbocharger technology allowed for easy coupling of the individual MGT system components, such as the gas generator, the combustion chamber and the power turbine. If required, some of the components can specially be designed for solar-hybrid operation. Integrating a solar receiver and an additional flow path for the externally heated air should also be achievable with minimal complications.

The twin-shaft configuration of the MGT system allows for flexibility in operation, which is advantageous, given the variable nature of the solar resource. The twin-shaft arrangement has the added advantage of ease of starting, as only the gas-generator needs to be turned over. Due to the large swallowing capacity, the use of a much bigger power turbine also places minimal flow restriction on the much smaller gas-generator turbine fitted upstream of it, even with the addition of load. The insensitivity to load variation should be advantageous during critical transient situations, such as load shedding and emergency shutdowns, for the MGT system under solar-hybrid operation.

The current air flow path, from the gas-generator compressor to the combustion chamber and then to the gas-generator turbine should be maintained for standard operation, but with the compressed air additionally passing through a suitably sized recuperator, in order to recover the energy contained in the exhaust gases leaving the power turbine. For solar-hybrid operation, an extra air flow path is required; that is, from the gas-generator compressor to the solar receiver – via a recuperator – and then to the combustion chamber. For solar-only operation, an additional route by-passing the combustion chamber, and leading straight to the gas-generator turbine would be required.

For this study, the development of the experimental MGT system involved no modifications to the turbocharger units. However, for solar-hybrid distributed electricity generation applications, the low-pressure compressor has to be replaced with an electric generator, and possibly a reduction gearbox.

Suitable highly efficient high-speed electric generators are lately readily accessible, at relatively affordable prices.

Most importantly, thermal insulation has to be added to the sections of the MGT system that are susceptible to heat losses, in order to increase both the work output and the cycle thermal efficiency. In addition, the design of the combustion chamber has to be optimised for minimum pressure loss, in order to counter the reduction in surge margin. Adding recuperation should further increase the cycle thermal efficiency, as was predicted in the theoretical modeling work.

4.6.2 System operation and control

To successfully operate and control the MGT system under solar-hybrid operation, firstly, an optimum equilibrium running point for the MGT system needs to be determined. The levels of solar share at which solar-hybrid operation is not possible or suitable, to dictate when to switch from solar to non-solar gas turbine operation mode also have to be specified.

The developed mathematical model can be used to determine an optimum equilibrium running point for the MGT system, for any given solar resource and ambient conditions. The developed mathematical model can further be used to predict the solar share limits beyond which, either solar-hybrid operation is not possible, or the performance of the MGT system drops below standard operation levels. A suitable control system that can maintain solar-hybrid operation within these solar share limits, or completely switch to standard operation otherwise would then need to be designed.

This study developed a suitable start-up procedure for the MGT system, which employed several flow control valves to regulate the air and fuel mass flow until the MGT system could run self-sustainably. The same start-up procedure can be adopted for solar-hybrid operation, with the compressed air supplied by a suitably sized air compressor unit or electric fan.

Furthermore, suitable shutdown procedures were developed for the MGT system, for both normal and emergency situations. With modifications, these shutdown procedures can be adopted for solar-hybrid operation.

The developed data acquisition system GUI can be modified, to include control loops for the several flow control valves. The developed GUI can further be modified to automatically implement the MGT system start-up and shutdown procedures, and also switch MGT system operation modes.

A schematic layout for the adapted experimental solar-hybrid MGT system is shown in Figure 4.16. The main difference between this layout, and that for the current experimental MGT system (Figure 4.2) is the replacement of the low-pressure compressor with an electric generator, and the addition of a recuperator and two more flow control valves (only the labels for the valves serving the same purpose on either layout are indicated in Figure 4.16). The

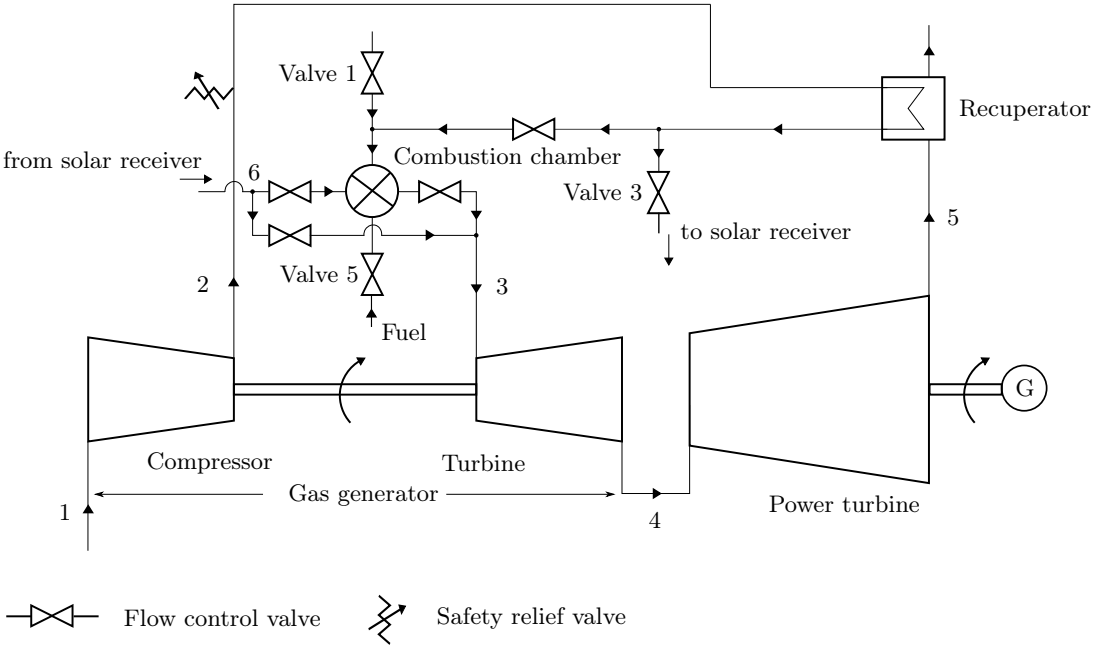

Figure 4.16: Schematic layout for the adapted experimental solar-hybrid MGT system

flow meters, as well as the static pressure and temperature measurement points are also omitted.

Chapter 5

Conclusion and Recommendations

Through both a theoretical and an experimental approach, this study aimed to develop a MGT system for central receiver CSP distributed electricity generation applications in Southern Africa. The theoretical modeling work involved modeling the performance of a MGT system under solar-hybrid operation, in order to predict the possible operating range, and develop suitable operational and control strategies for the MGT system. The design and experimental work involved designing, building, testing and characterising the performance of an experimental MGT system, and then using the obtained test data to validate the predicted performance, as well as assess the technical feasibility of adapting such a system to solar-hybrid operation.

5.1 Theoretical modeling findings

5.1.1 Component matching

From the component matching, the equilibrium running point of the MGT system shifted on the compressor characteristic, to a region of higher compressor pressure ratio and non-dimensional speed and mass flow rate. The shift of the equilibrium running point was to counter the system pressure losses introduced by the addition of solar thermal energy into the MGT system, and ensure the compressor work requirement was met by the coupled gas-generator turbine, while also maintaining a useful work output from the power turbine. However, the shift of the equilibrium running point resulted in a reduction in the surge margin, but still within the typical surge margin expected for power and propulsion applications.

5.1.2 Solar-hybrid operating range

The models showed that solar-hybrid operation was only possible for solar share of at least 20 %, for any solar day. For solar share beyond 81 %, for the summer day, and 86 %, for the winter day, the work output of the MGT

system under solar-hybrid operation drops below standard operation levels. Similarly, for solar share beyond 69 %, for the winter day, and 74 %, for the summer day, the MGT system operates at a cycle thermal efficiency below standard operation levels, further limiting the solar share operating range. Therefore, a suitable control system that can maintain solar-hybrid operation within these solar share limits, and completely switch to standard operation otherwise would need to be designed.

In contrast to standard operation, a higher nominal work output of 20 kW, at a lower specific fuel consumption of 0.0004 kg/kWh and a higher cycle thermal efficiency of 8 % was predicted for the MGT system under solar-hybrid operation, the latter potentially increasing to 20 % with the addition of recuperation. Better solar-hybrid performance is expected with the use of more efficient/better performing individual MGT system components.

5.1.3 Solar-hybrid transient performance

The simplified approach adopted for the transient modeling showed that a sudden change in solar irradiation was corrected by altering the fuel flow, when the proposed control strategy of operating the MGT system at the determined solar-hybrid equilibrium running point was implemented. In addition, the gas-generator rotational speed remained below the maximum industry accepted rotor over speed. Therefore, solar-hybrid equilibrium running could potentially eliminate the risk of running into compressor surge, albeit with a reduced surge margin.

5.2 Design and experimental findings

5.2.1 Model validation

The predicted MGT system equilibrium running point closely matched the experimentally determined equilibrium running points that corresponded to the best MGT system performance. In addition, similar standard MGT system performance was predicted for varying levels of system pressure losses – the latter obtained using different combustion chamber pressure drop models – and different equilibrium running points. Similar to the findings from the modeling work, the MGT system equilibrium point shifted on the compressor characteristic, in order to counter the high combustion chamber pressure losses, and ensure the work requirement for the gas-generator compressor was met, while also maintaining a useful work output from the power turbine. The shift of the MGT system equilibrium point similarly resulted in a reduction in the surge margin.

5.2.2 Feasibility of adapting the MGT System to solar-hybrid operation

The MGT system is based on off-the-shelf turbocharger technology, which should allow for easy coupling of the individual MGT system components, some of which could be specially designed for solar-hybrid operation. Therefore, the integration of the solar receiver and the externally heated air into the gas turbine systems should be achievable with minimal complications.

The twin-shaft configuration of the MGT system allows for flexibility in operation, with the added advantage of ease of starting. The large swallowing capacity of the much bigger power turbine should ensure that the MGT system is insensitive to load variation, which should be advantageous during critical transient situations, such as load shedding and emergency shutdowns.

The developed start-up and shutdown procedures for the MGT system can be adopted for solar-hybrid operation. The developed data acquisition system GUI can be modified, to implement the MGT system start-up and shutdown procedures, and switch MGT system operation modes.

5.3 On-site implementation

The developed experimental MGT system is still some way short of being ready for solar-hybrid operation. Nevertheless, through both the modeling and experimental work, this study has made significant steps towards achieving this.

The advantages of using off-the-shelf turbocharger components, in a twin-shaft configuration were highlighted. The addition of thermal insulation should address the heat losses, and the subsequent low work output and cycle thermal efficiency, while the use of a combustion chamber redesigned for minimum pressure loss should correct the drop in surge margin, and subsequently widen the possible operating range of the MGT system under solar-hybrid operation. Adding a suitably sized recuperator to the MGT system should further increase the cycle thermal efficiency.

Most importantly, a suitable control system will have to be developed, to perform the operation and control of the MGT system. The development process can build upon the experience gained from developing the data acquisition system GUI.

5.4 Recommendations

Future modeling work should involve performing a thorough analysis of the transient behaviour of the MGT system under solar-hybrid operation. The transient analysis should investigate the dynamic effects of additional thermal inertia and pressurised air volume in the MGT system components dur-

ing critical transient situations, such as abrupt load shedding and emergency shutdowns. The transient analysis should culminate into the development of a suitable control system for the MGT system under solar-hybrid operation.

Further modeling work should investigate the potential for improving the performance of the MGT system, through using more efficient/better performing individual MGT system components. The combustion chamber should be modeled based on an optimised design, while the gas generator and power turbine should be modeled based on more efficient off-the-shelf turbocharger units.

Future experimental work should entail adding a solar receiver and a flow path for the pressurised air flowing to/from the solar receiver, in addition to a suitably sized recuperator. The receiver can be simulated using an electric heating duct. The geometry of the recuperator and the heating duct, and the size and length of the piping used for the additional air flow path will be useful inputs to the transient analysis.

The experimental MGT system test bench should also be improved. In addition to redesigning the combustion chamber, and adding thermal insulation to all sections of the test bench that are susceptible to heat losses, further improvements should include: replacing the low-pressure compressor with a suitable high-speed electric generator and replacing the low-temperature flow control valves and rubber tubing and hoses with suitable high-temperature substitutes. The addition of an electric generator should allow for proper loading of the MGT system, which should in turn allow a proper investigation of the sensitivity of the MGT system to load variation.

Finally, more appropriate/accurate instrumentation and measurement techniques should be adopted for parameters such as the gas-generator TIT and the fuel mass flow rate, in order to reduce their associated measurement uncertainty to the recommended levels.

Appendices

Appendix A

Instrumentation Calibration

A.1 Calibration of the pressure transducers

The low-pressure ($\leq$10 kPa) pressure transducers were statically calibrated against a Betz 5000 Micromanometer [serial number 12453]. Each of the pressure transducers was calibrated for its expected pressure measurement range.

The calibration procedure involved setting a gauge pressure on the Betz 5000 Micromanometer, and then recording the corresponding analog voltage signal generated by the pressure transducer. The set gauge pressure was then plotted against the corresponding generated analog voltage signal, and linear correlations were generated from the plotted data, as shown in Table A.1. The data logger was then configured to convert the input analog voltage signal from the pressure transducers to a pressure reading, using the generated correlations.

The high-pressure pressure transducers were statically calibrated against a Fluke 700G31 pressure gauge [serial number 3142086]. The calibration procedure was similar to that followed for the low-pressure pressure transducers. The linear correlations obtained from the plotted calibration data are similarly given in Table A.1.

Table A.1: Correlations obtained from the calibration of the pressure transducers

Station		Transducer	Equation	R^2
Venturi tube	diff	E+H K9007321121	$1.248V - 2.484$ [kPa]	1.0000
	diff	E+H KC00A021121	$74.589V - 74.289$ [kPa]	0.9999
Orifice 2	diff	E+H K9006B21121	$12.473V - 25.421$ [kPa]	0.9998
	abs	HBM 173710065	$75.139V + 18.091$ [kPa]	1.0000
Bellmouth	diff	E+H FB00072109D	$374.87V - 753.06$ [Pa]	1.0000
2	abs	HBM 173710078	$43.926V - 3.833$ [kPa]	1.0000
3	abs	HBM 143210119	$65.004V - 20.055$ [kPa]	1.0000
Ambient	abs	HBM 141410077	$18.351V - 2.701$ [kPa]	1.0000

Table A.2: Correlations obtained from the calibration of the thermocouples

Station		Equation	R^2
8	T-type	$T_{6,corr} = 1.0170T_{meas} + 0.2262$ [°C]	1.0000
		$T_{7,corr} = 1.0211T_{meas} + 0.1096$ [°C]	1.0000
		$T_{8,corr} = 1.0066T_{meas} + 0.2982$ [°C]	1.0000
		$T_{9,corr} = 1.0136T_{meas} + 0.0637$ [°C]	1.0000
2	T-type	$T_{10,corr} = 1.0131T_{meas} + 0.0081$ [°C]	1.0000
		$T_{11,corr} = 1.0147T_{meas} - 0.0274$ [°C]	1.0000
		$T_{5,corr} = 1.0124T_{meas} + 0.3297$ [°C]	1.0000
		$T_{13,corr} = 1.0132T_{meas} + 0.0736$ [°C]	1.0000
3	K-type	$T_{14,corr} = 1.0130T_{meas} - 2.8064$ [°C]	1.0000
		$T_{15,corr} = 1.0081T_{meas} - 2.1460$ [°C]	1.0000
		$T_{16,corr} = 1.0058T_{meas} - 3.1310$ [°C]	1.0000
		$T_{17,corr} = 1.0078T_{meas} - 3.0346$ [°C]	1.0000
Bellmouth	J-type	$T_{18,corr} = 1.0068T_{meas} + 0.0693$ [°C]	1.0000
		$T_{19,corr} = 1.0048T_{meas} + 0.0880$ [°C]	1.0000
		$T_{20,corr} = 1.0054T_{meas} + 0.1427$ [°C]	1.0000
		$T_{21,corr} = 1.0053T_{meas} + 0.1430$ [°C]	1.0000
Fuel supply	T-type	$T_{fuel,corr} = 1.0225T_{meas} - 0.8934$ [°C]	1.0000

A.2 Calibration of the thermocouples

The low-temperature thermocouples (T-type and J-type) were calibrated against an Isotech platinum resistance thermometer [model number 935-14-72, serial number 191069 and calibrated on 7/01/2019], using a Fluke 9142 Field Metrology Well thermocouple calibrator [serial number B29291]. For the expected temperature measurement range, a temperature was set on the thermocouple calibrator, and the corresponding reference temperature measured by the thermometer T_{ref} and that measured by the thermocouple T_{meas} was recorded. The temperatures measured by the thermocouples were then plotted against the corresponding reference temperatures, and linear correlations were obtained from the plotted data, as shown in Table A.2. The data logger was then configured to correct the temperature measured by each of the thermocouples using the corresponding linear correlation.

The high-temperature K-type thermocouples were calibrated using a Fluke 9150 portable furnace [serial number 853479]. The calibration procedure was similar to that followed for the low-temperature thermocouples, with the only difference being that there was no reference thermometer to calibrate the thermocouples against. Rather, a reference temperature was set on the thermocouple calibrator, and the corresponding temperatures measured by the thermocouples were recorded. The set reference temperature was then plotted against that measured by the thermocouples, and linear correlations were generated from the plotted data (see Table A.2). The data logger was then configured to correct the temperature measured by each of the thermocouples using the

corresponding linear correlation.

A.3 Calibration of the fuel flow meter

The Venturi tube fuel flow meter was calibrated against 2 Festo SFE1-LF series air flow sensors [Serial numbers 537875 W972 and 537877 W472] connected parallel to each other, but with both in line with, and upstream of the Venturi tube. The use of two flow sensors allowed the calibration to cover the full fuel mass flow rate measurement range. The flow sensors were factory calibrated at standard conditions (0 °C and 1.01325 bar absolute), and each has a volumetric flow rate measuring range of 10 to 200 l/min. The air mass flow rate through either sensor is calculated from the product of the measured volumetric flow rate and the air density corresponding to the standard conditions (Festo, 2007).

The Venturi tube was calibrated for the expected fuel mass flow rate measurement range, using compressed air. The calibration set up consisted of the whole fuel supply system shown in Figure 4.7, but with the gas cylinder replaced by a pressurised air line. The air pressure was regulated using a Festo LFR-D-Mini pressure regulator, with an operating range of 0 to 16 bar.

The calibration procedure involved setting the supply pressure, and then gradually opening the flow control valve, and varying the flow through the Venturi tube. For each degree of opening of the flow control valve, the total air mass flow rate measured by the flow sensors, the static pressure measured at the up stream tap, the differential pressure across the Venturi tube throat, and the static temperature measured upstream of the venturi tube were recorded.

Two calibration test runs were performed, and the obtained test data was averaged, and its standard deviation determined. The averaged test data was then used to calculate the coefficient of discharge and the throat Reynolds number.

To ensure that the determined coefficient of discharge satisfied mechanical flow similarity, when the designed flow meter was used with propane, the calculated coefficient of discharge C was plotted against the throat diameter Reynolds number Re_d (see Figure A.1). As expected, a logarithmic trend was observed, with the coefficient of discharge in the order of 1.0 (Fluid Meters, 1959; ASME PTC 19.5, 2004).

However, wide discrepancies were observed for the calculated coefficient of discharge, at higher Reynolds number. This was attributed to the reduced accuracy of the Festo flow meters, when operating at higher air mass flow rates, and subsequently higher Reynolds number. Therefore, a coefficient of discharge of unity was adopted for the calculation of the fuel mass flow rate.

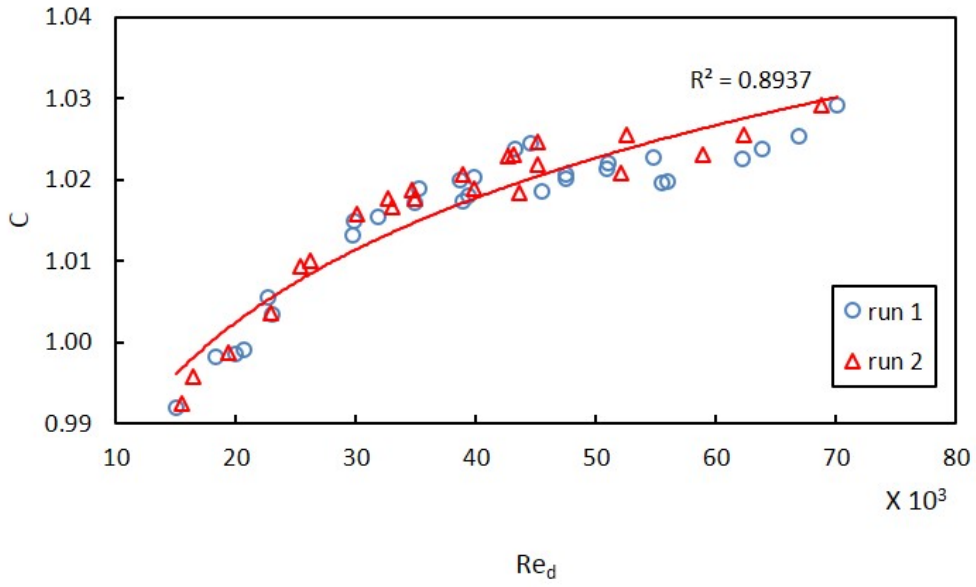

Figure A.1: Venturi tube coefficient of discharge vs throat diameter Reynolds number

Appendix B

Data Acquisition System GUI

B.1 Block diagram

Figure B.1 shows a snippet of the built block diagram. The block diagram consists of DAQ Assistant VIs, which either acquire analog signal from the measurement sensors, and convert this signal to measurement readings, or generate analog signal to control the valve actuators. Code was written in the block diagram, to convert the acquired signal to measurement readings and also perform calculations of the different MGT system performance parameters.

B.2 Front panel

The front panel is the user interface, and it consists of controls and indicators. The MGT system was operated, and the taken measurements and calculated parameters were displayed in real-time using several front panel containers.

The flow valves were controlled using the front panel container shown in Figure B.2a. The temperature measurements were displayed using the front panel container shown in Figure B.2b, while the rotational speed measurements were displayed using the front panel container shown in Figure B.2c, and the pressure measurements were displayed using the front panel container shown in Figure B.2d. Finally, the calculated air and fuel mass flow rates, and the corresponding independent parameters, were displayed using the front panel container shown in Figure B.2e.

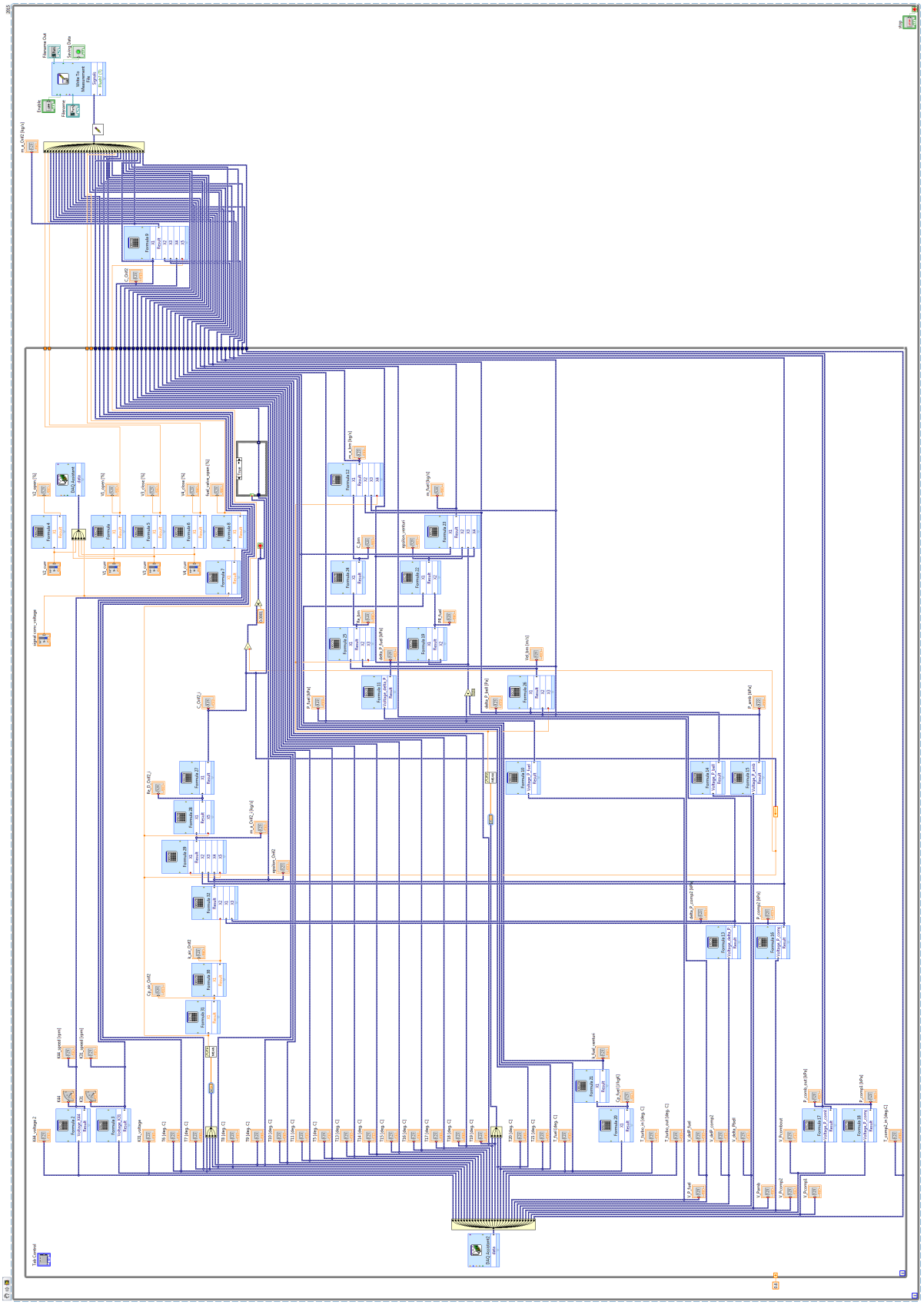

Figure B.1: Block diagram

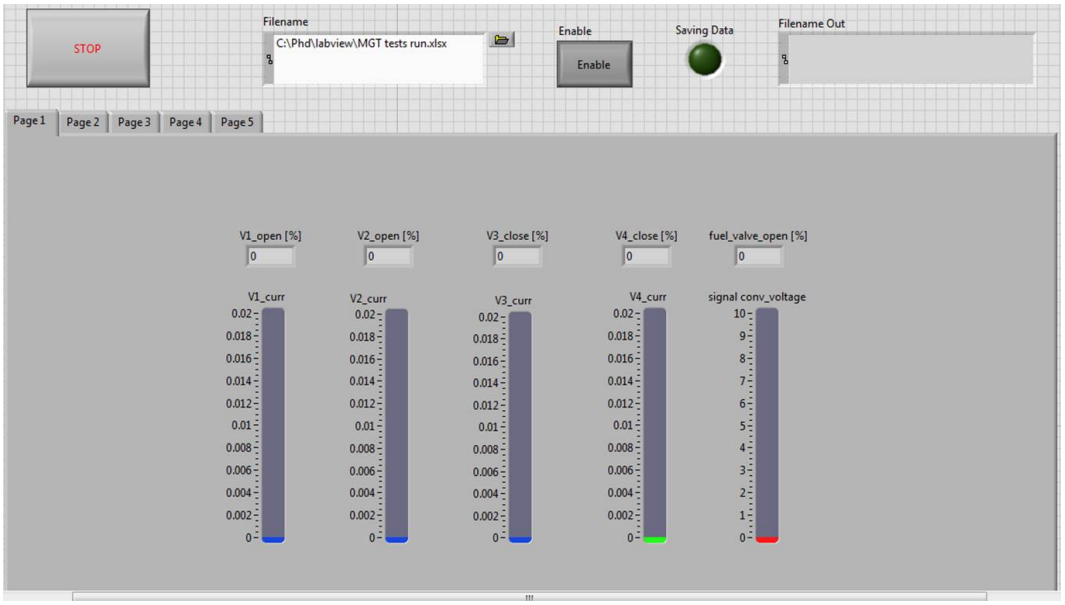

(a) Control of flow valves

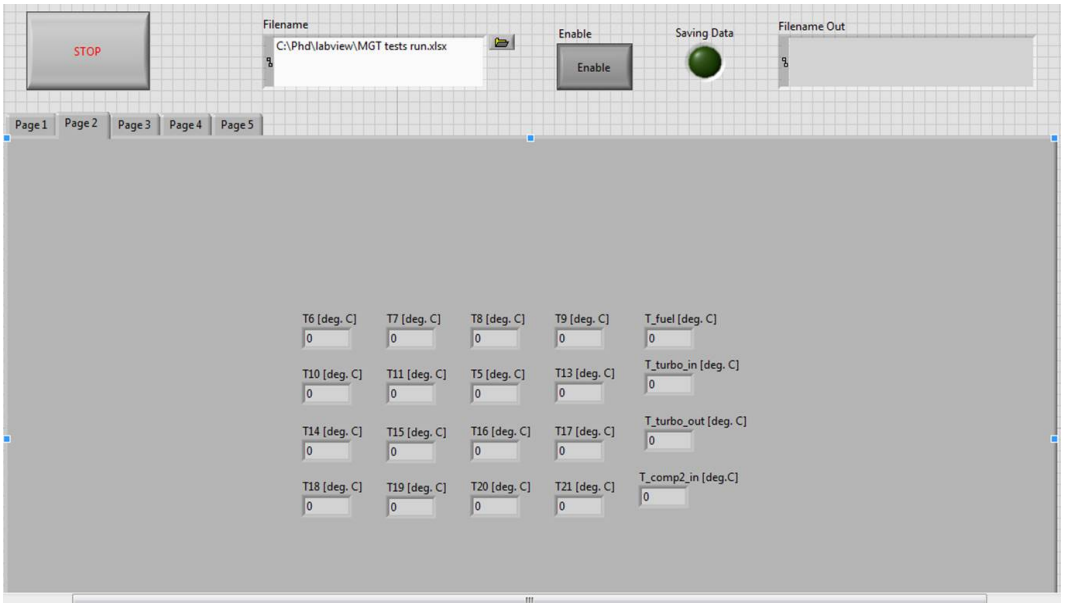

(b) Temperature measurements

Figure B.2: Front panel containers

(c) Rotational speed gauges

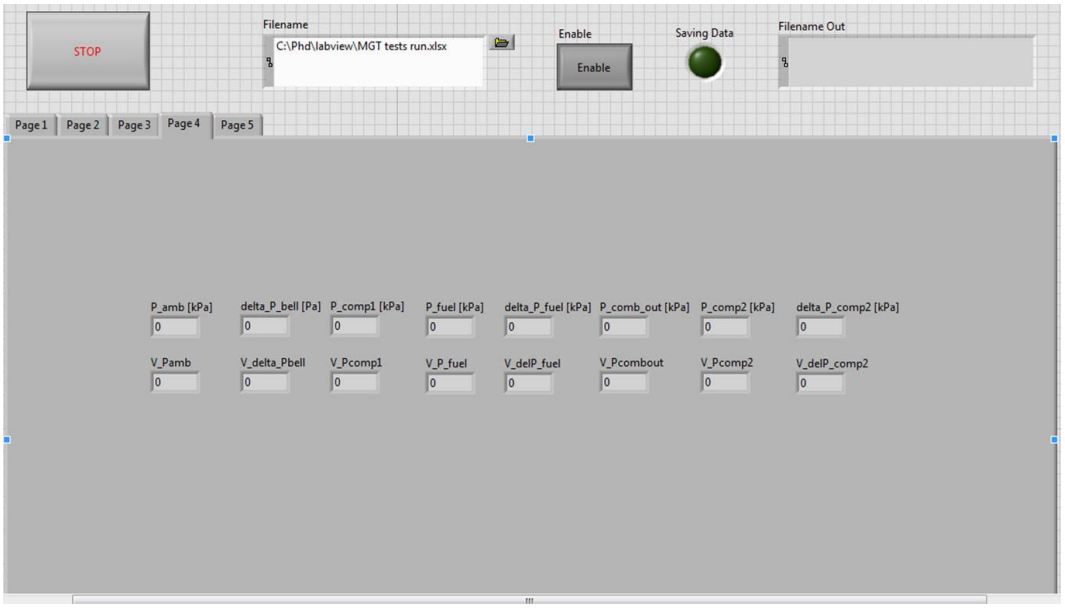

(d) Pressure measurements

Figure B.2: Front panel containers (cont'd)

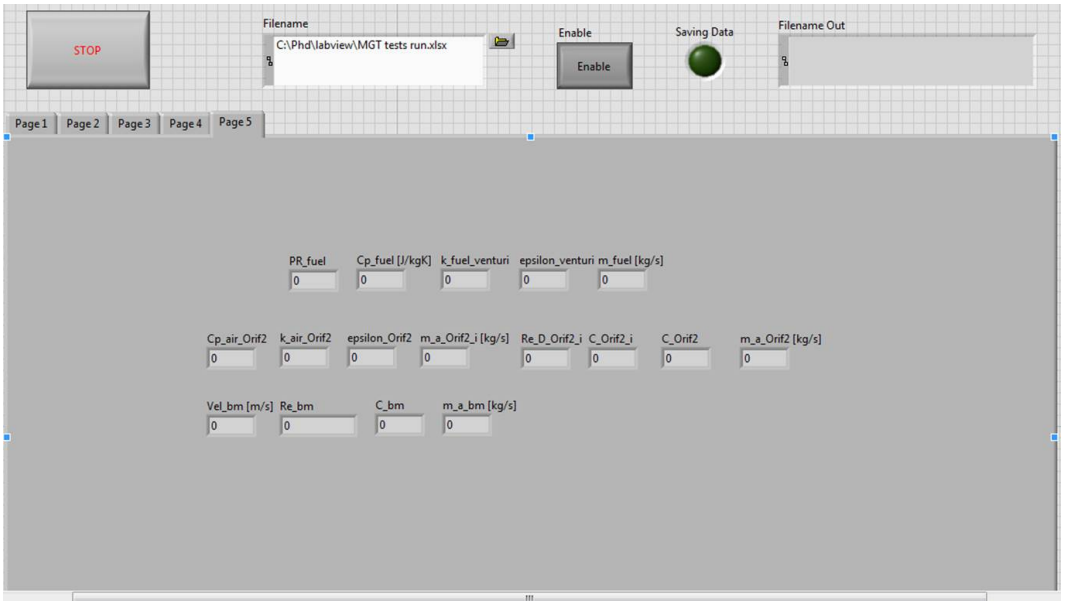

(e) Calculated mass flow rates

Figure B.2: Front panel containers (cont'd)

Appendix C

Data and Sample Calculation

C.1 Modeling data

Tables C.1 and C.2 show the predicted steady-state performance parameters for the MGT system under solar-hybrid operation, while Tables C.3 and C.4 show the predicted steady-state performance parameters for the MGT system under standard operation, for a winter day (04 August, 2016), and a summer day (04 January, 2017), respectively.

Table C.1: Performance parameters for the MGT system under solar-hybrid operation (winter day)

Time [hours: minutes]	$\dot{m}_a$ [kg/s]	$\dot{m}_f$ [kg/s]	T_{06} [°C]	ΔP_{rec} [% of P_{02}]	ΔP_{comb} [% of P_{02}]	T_{03} [°C]	Solar share [%]	$\dot{W}_{pt}$ [kW]	SFC [kg/kWh]	η_{th} [%]	$\eta_{th,R}$ [%]
09:00	0.477	0.005	289	2	7	727	21	36.3	0.0005	12	28
10:00	0.476	0.003	425	2	11	696	47	26.5	0.0005	9	22
11:00	0.474	0.003	471	2	12	686	56	23.0	0.0004	8	20
12:00	0.473	0.002	487	2	12	683	60	21.7	0.0004	8	19
13:00	0.473	0.003	481	2	12	685	58	22.2	0.0004	8	20
14:00	0.472	0.003	447	2	11	698	50	25.1	0.0004	9	22
15:00	0.471	0.004	363	2	9	724	33	31.8	0.0005	11	25

Table C.2: Performance parameters for the MGT system under solar-hybrid operation (summer day)

Time [hours: minutes]	$\dot{m}_a$ [kg/s]	$\dot{m}_f$ [kg/s]	T_{06} [°C]	ΔP_{rec} [% of P_{02}]	ΔP_{comb} [% of P_{02}]	T_{03} [°C]	Solar share [%]	$\dot{W}_{pt}$ [kW]	SFC [kg/kWh]	η_{th} [%]	$\eta_{th,R}$ [%]
07:00	0.467	0.006	286	2	7	744	19	36.7	0.0005	12	28
08:00	0.464	0.003	446	2	11	707	49	25.1	0.0005	9	22
09:00	0.463	0.002	504	2	13	694	61	20.5	0.0004	8	19
10:00	0.460	0.002	523	2	13	696	64	19.2	0.0004	7	18
11:00	0.457	0.002	548	2	14	696	69	17.2	0.0004	7	16
12:00	0.456	0.002	558	2	14	696	71	16.4	0.0004	6	16
13:00	0.454	0.002	560	2	14	701	70	16.5	0.0004	6	16
14:00	0.453	0.002	549	2	14	711	67	18.0	0.0004	7	17
15:00	0.452	0.002	530	2	13	721	62	20.0	0.0004	8	18
16:00	0.453	0.003	484	2	12	735	52	24.0	0.0005	9	21
17:00	0.453	0.005	351	2	8	776	26	34.5	0.0005	11	27

Table C.3: Performance parameters for the MGT system under standard operation (winter day)

Time [hours: minutes]	P_{amb} [kPa]	T_{amb} [°C]	$\dot{m}_a$ [kg/s]	$\dot{m}_f$ [kg/s]	ΔP_{comb} [% of P_{02}]	T_{03} [°C]	$\dot{W}_{pt}$ [kW]	SFC [kg/kWh]	η_{th} [%]	$\eta_{th,R}$ [%]
00:00	101.3	11	0.415	0.0043	6	532	12.5	0.0012	7	17
01:00	101.3	11	0.415	0.0043	6	531	12.5	0.0012	7	17
02:00	101.2	12	0.414	0.0043	6	534	12.5	0.0012	7	17
03:00	101.2	11	0.414	0.0043	6	533	12.5	0.0012	7	17
04:00	101.2	10	0.414	0.0043	6	531	12.5	0.0012	7	17
05:00	101.2	9	0.415	0.0042	6	529	12.5	0.0012	7	17
06:00	101.2	9	0.415	0.0042	6	528	12.5	0.0012	7	17
07:00	101.2	10	0.415	0.0042	6	529	12.5	0.0012	7	17
08:00	101.2	10	0.415	0.0042	6	529	12.5	0.0012	7	17
09:00	101.2	11	0.414	0.0043	6	533	12.5	0.0012	7	17
10:00	101.3	13	0.413	0.0043	6	538	12.5	0.0012	7	17
11:00	101.2	15	0.411	0.0043	6	542	12.5	0.0012	7	17
12:00	101.2	16	0.411	0.0043	6	544	12.5	0.0012	7	17
13:00	101.1	16	0.410	0.0043	6	544	12.5	0.0012	7	17
14:00	101.0	16	0.409	0.0043	6	545	12.5	0.0012	7	17
15:00	100.9	17	0.409	0.0043	6	545	12.4	0.0012	7	17
16:00	100.9	17	0.409	0.0043	6	546	12.4	0.0012	7	17
17:00	100.8	17	0.408	0.0043	6	545	12.4	0.0012	7	17
18:00	100.8	16	0.409	0.0043	6	543	12.4	0.0012	7	17
19:00	100.8	14	0.410	0.0042	6	539	12.4	0.0012	7	17
20:00	100.8	12	0.411	0.0042	6	535	12.4	0.0012	7	17
21:00	100.8	11	0.412	0.0042	6	532	12.4	0.0012	7	17
22:00	100.8	10	0.413	0.0042	6	528	12.4	0.0012	7	17
23:00	100.9	8	0.415	0.0042	6	526	12.4	0.0012	7	17

Table C.4: Performance parameters for the MGT system under standard operation (summer day)

Time [hours: minutes]	P_{amb} [kPa]	T_{amb} [°C]	$\dot{m}_a$ [kg/s]	$\dot{m}_f$ [kg/s]	ΔP_{comb} [% of P_{02}]	T_{03} [°C]	$\dot{W}_{pt}$ [kW]	SFC [kg/kWh]	η_{th} [%]	$\eta_{th,R}$ [%]
00:00	100.1	19	0.404	0.0042	6	551	12.3	0.0012	7	17
01:00	100.0	19	0.403	0.0042	6	551	12.3	0.0012	6	17
02:00	100.0	19	0.404	0.0042	6	549	12.3	0.0012	6	17
03:00	99.9	19	0.403	0.0042	6	551	12.2	0.0012	6	17
04:00	99.9	18	0.404	0.0042	6	548	12.2	0.0012	6	17
05:00	99.8	16	0.405	0.0042	6	544	12.2	0.0012	7	17
06:00	99.8	15	0.405	0.0042	6	541	12.2	0.0012	7	17
07:00	99.9	16	0.405	0.0042	6	544	12.2	0.0012	6	17
08:00	99.9	19	0.403	0.0042	6	551	12.3	0.0012	6	17
09:00	99.9	22	0.401	0.0042	6	556	12.3	0.0012	6	17
10:00	99.9	24	0.399	0.0043	6	563	12.3	0.0012	6	17
11:00	99.8	28	0.397	0.0043	6	570	12.3	0.0012	6	17
12:00	99.8	29	0.396	0.0043	6	573	12.3	0.0013	6	17
13:00	99.7	31	0.394	0.0043	6	578	12.3	0.0013	6	16
14:00	99.6	32	0.393	0.0043	6	581	12.3	0.0013	6	16
15:00	99.5	33	0.392	0.0043	6	582	12.2	0.0013	6	16
16:00	99.4	32	0.393	0.0043	6	578	12.2	0.0013	6	16
17:00	99.3	31	0.393	0.0043	6	578	12.2	0.0013	6	16
18:00	99.2	31	0.392	0.0042	6	577	12.2	0.0013	6	16
19:00	99.2	30	0.393	0.0042	6	575	12.2	0.0013	6	16
20:00	99.2	28	0.394	0.0042	6	571	12.2	0.0013	6	16
21:00	99.2	26	0.396	0.0042	6	566	12.1	0.0013	6	16
22:00	99.2	23	0.397	0.0042	6	560	12.1	0.0013	6	17
23:00	99.2	22	0.398	0.0042	6	556	12.1	0.0012	6	17

C.2 Test data

The averaged test data obtained from the two performed test runs is presented in Tables C.5 and C.6. As previously noted, the test runs were performed in succession, and on the same day, to ensure similar test conditions. The obtained test data was used to determine the MGT system performance parameters.

Table C.5: Averaged test data (run 1)

Fuel valve [%]	P_{amb} [kPa]	T_{amb} [°C]	ΔP_{bm} [Pa]	$\dot{m}_{a,comp1}$ [kg/s]	P_2 [kPa]	T_2 [°C]	N_{comp1} [rpm]	T_f [°C]	P_f [kPa]	ΔP_{vent} [kPa]	$\dot{m}_f$ [kg/s]	P_3 [kPa]	T_3 [°C]	T_8 [°C]	P_8 [kPa]	ΔP_{orif2} [kPa]	C_{orif2}	$m_{a,comp2}$ [kg/s]	N_{comp2} [rpm]
53	100.2	17	793	0.204	171.4	79	61 675	14	163.9	2.2	0.0034	154.6	818	24	105.1	8.2	0.6103	0.358	15 199
55	100.2	18	1050	0.234	191.6	97	68 299	15	155.6	2.9	0.0039	171.6	836	27	107.4	11.5	0.6099	0.424	17 852
57	100.2	20	1265	0.256	208.4	112	73 611	15	151.4	3.7	0.0043	184.4	853	32	109.4	14.6	0.6097	0.473	20 015

Table C.6: Averaged test data (run 2)

Fuel valve [%]	P_{amb} [kPa]	T_{amb} [°C]	ΔP_{bm} [Pa]	$\dot{m}_{a,comp1}$ [kg/s]	P_2 [kPa]	T_2 [°C]	N_{comp1} [rpm]	T_f [°C]	P_f [kPa]	ΔP_{vent} [kPa]	$\dot{m}_f$ [kg/s]	P_3 [kPa]	T_3 [°C]	T_8 [°C]	P_8 [kPa]	ΔP_{orif2} [kPa]	C_{orif2}	$\dot{m}_{a,comp2}$ [kg/s]	N_{comp2} [rpm]
54	100.1	19	884	0.214	179.8	91	64 692	15	162.7	2.4	0.0036	161.6	843	28	106.0	9.8	0.6101	0.390	16 465
56	100.1	21	1109	0.239	195.7	106	70 018	15	155.8	3.1	0.0040	175.1	854	32	107.9	12.7	0.6098	0.440	18 648
57	100.1	22	1331	0.262	213.4	119	75 177	16	156.7	4.0	0.0045	189.7	873	36	110.0	15.8	0.6096	0.488	20 711

C.3 Uncertainty in the measured and calculated parameters

The uncertainty analysis presented in Section 4.4 was implemented as described below, with the applied equations adapted from the ASME PTC 19.1 Standard.

The combined uncertainty in a measured parameter X, or a calculated parameter R, was determined as the root-sum-square of the bias and precision uncertainty components of either the measured or the calculated parameter, using the general form

$$u_X = \left[(b_X)^2 + (p_X)^2\right]^{1/2} \tag{C.1}$$

for the measured parameter, and

$$u_R = \left[(b_R)^2 + (p_R)^2\right]^{1/2} \tag{C.2}$$

for the calculated parameter, where b_X and b_R are the bias uncertainty components and p_X and p_R are the precision uncertainty components.

For the measured parameters, the bias uncertainty was calculated as the root-sum-square of the individual bias uncertainties for all possible sources of bias error in a measured parameter, using

$$b_X = \left[\sum_{k=1}^{K} (b_{X_k})^2\right]^{1/2} \tag{C.3}$$

where b_{X_k} is the estimated bias uncertainty of the k^{th} source of bias error and K is the total number of bias error sources in the measured parameter.

To determine the precision uncertainty in each measured parameter, the mean $\overline{X}$ of the N sample measurements taken for each test point was first calculated, using

$$\overline{X} = \frac{\sum_{j=1}^{N} X_j}{N} \tag{C.4}$$

where X_j is the value of each individual measurement in the sample. The sample standard deviation was calculated using

$$s_X = \sqrt{\sum_{j=1}^{N} \frac{\left(X_j - \overline{X}\right)^2}{N-1}} \tag{C.5}$$

with the precision uncertainty of the sample mean then given by

$$p_X = \frac{s_X}{\sqrt{N}} \tag{C.6}$$

For the calculated parameters, the bias and precision uncertainty components were expressed as either absolute or relative. If a calculated parameter was determined from measured and averaged, and/or assigned values of independent parameters (X_i), that is $R = f(X_1, X_2, ..., X_I)$, where I is the total number of independent parameters involved in R, then, the absolute bias uncertainty in the calculated parameter was determined using

$$b_R = \left[\sum_{i=1}^{I} (\theta_i b_{X_i})^2\right]^{1/2} \tag{C.7}$$

where θ_i and b_{X_i} are the sensitivity coefficient and bias uncertainty of the i^{th} independent parameter, respectively. The relative bias uncertainty in a calculated parameter was given by

$$\frac{b_R}{R} = \left[\sum_{i=1}^{I} \left(\theta_i \frac{b_{X_i}}{X_i}\right)^2\right]^{1/2} \tag{C.8}$$

The absolute precision uncertainty in a calculated parameter was given by

$$p_R = \left[\sum_{i=1}^{I} (\theta_i p_{X_i})^2\right]^{1/2} \tag{C.9}$$

while the relative precision uncertainty in a calculated parameter was given by

$$\frac{p_R}{R} = \left[\sum_{i=1}^{I} \left(\theta_i \frac{p_{X_i}}{X_i}\right)^2\right]^{1/2} \tag{C.10}$$

where p_{X_i} is the precision uncertainty in each averaged independent parameter X_i.

Finally, for a 95 % confidence interval, the total uncertainty in a measured parameter was given by

$$U_X = 2u_X \tag{C.11}$$

while that in a calculated parameter was given by

$$U_R = 2u_R \tag{C.12}$$

As discussed in Section 4.4, uncertainty analysis was performed for MGT system performance parameters that could be determined with some level of accuracy, such as the measured gas-generator TIT and rotational speed, and

Table C.7: Bias uncertainty in the calculated fuel mass flow rate

Parameter	Parameter bias uncertainty $\frac{b_{X_i}}{X_i}$ [%]	Sensitivity coefficient, θ_i	$\frac{b_{X_i}}{X_i}\theta_i$
Discharge coefficient, C	$\frac{b_C}{C} = 0.70$	1.00	0.70
Expansion factor, ϵ	$\frac{b_\epsilon}{\epsilon} = \frac{4\Delta P}{P} = \frac{4(3.7)}{151.4} = 0.098$ %	1.00	0.098
Pipe diameter, D [mm]	$\frac{b_D}{D} = \frac{0.1}{8} = 1.25$ %	$\frac{2\beta^4}{1-\beta^4} = \frac{2(0.65)^4}{1-(0.65)^4} = 0.43$	0.54
Throat diameter, d [mm]	$\frac{b_d}{d} = \frac{0.1}{5.2} = 1.92$ %	$\frac{2}{1-\beta^4} = \frac{2}{1-(0.65)^4} = 2.43$	4.67
Differential pressure, ΔP [mbar]	$\frac{b_{\Delta P}}{\Delta P} = \frac{0.39}{37} = 1.05$ %	0.50	0.53
Density, $\rho = f(P,T)$ [kg/m^3]	$\frac{b_P}{P} = \pm 0.18$, $\frac{b_T}{T} = \frac{0.6}{15} = 4.00$ % $\frac{b_\rho}{\rho} = \left[\left(\frac{b_P}{P}\right)^2 + \left(\frac{b_T}{T}\right)^2\right]^{1/2} = 4.00$ %	0.50	2.00
Total bias uncertainty, $\frac{b_{\dot{m}_f}}{\dot{m}_f}$	...	...	5.18 %

Table C.8: Precision uncertainty in the calculated fuel mass flow rate

Parameter	Nominal value, X_i	s_{X_i}	N_i	$p_{X_i} = \frac{S_{X_i}}{\sqrt{N_i}}$	Parameter precision uncertainty $\frac{p_{X_i}}{X_i}$ [%]	Sensitivity coefficient, θ_i	$\frac{p_{X_i}}{X_i}\theta_i$
Discharge coefficient, C	...	...	...	...	...	1.00	0.00
Expansion factor, ϵ	...	...	...	...	...	1.00	0.00
Pipe diameter, D [mm]	8.0	...	...	...	...	$\frac{2\beta^4}{1-\beta^4} = \frac{2(0.65)^4}{1-(0.65)^4} = 0.43$	0.00
Throat diameter, d [mm]	5.2	...	...	...	...	$\frac{2}{1-\beta^4} = \frac{2}{1-(0.65)^4} = 2.43$	0.00
Differential pressure, ΔP [kPa]	3.7	0.03	140	0.0025	0.068 %	0.50	0.034
Density, $\rho = f(P,T)$ [kg/m^3]	...	...	...	...	0.080 %	0.50	0.040
Total precision uncertainty, $\frac{p_{\dot{m}_f}}{\dot{m}_f}$	...	...	...	...	...	...	0.052 %

Table C.9: Bias uncertainty in the calculated air mass flow rate

Parameter	Parameter bias uncertainty $\frac{b_{X_i}}{X_i}$ [%]	Sensitivity coefficient, θ_i	$\frac{b_{X_i}}{X_i}\theta_i$
Discharge coefficient, C	$\frac{b_C}{C} = 1.00$	1.00	1.00
Expansion factor, ϵ	$\frac{b_\epsilon}{\epsilon} = \frac{4\Delta P}{P} = \frac{4(1.265)}{100.2} = 0.050$ %	1.00	0.050
Pipe diameter, D [mm]	$\frac{b_D}{D} = \frac{0.1}{213.7} = 0.047$ %	$\frac{2\beta^4}{1-\beta^4} = \frac{2(0.4)^4}{1-(0.4)^4} = 0.05$	0.0024
Throat diameter, d [mm]	$\frac{b_d}{d} = \frac{0.1}{77.3} = 0.13$ %	$\frac{2}{1-\beta^4} = \frac{2}{1-(0.4)^4} = 2.05$	0.27
Differential pressure, ΔP [Pa]	$\frac{b_{\Delta P}}{\Delta P} = \frac{23.1}{1265} = 1.83$ %	0.50	0.92
Density, $\rho = f(P,T)$ [kg/m^3]	$\frac{b_P}{P} = \pm 0.3$, $\frac{b_T}{T} = \frac{0.6}{20} = 3.00$ % $\frac{b_\rho}{\rho} = \left[\left(\frac{b_P}{P}\right)^2 + \left(\frac{b_T}{T}\right)^2\right]^{1/2} = 3.01$ %	0.50	1.51
Total bias uncertainty, $\frac{b_{\dot{m}_a}}{\dot{m}_a}$	...	...	2.05 %

the calculated gas-generator air and fuel mass flow rates. The uncertainty analysis only considered test data from the third test point of test run 1 (see third row of Table C.5). The same analysis is applicable to all the other obtained test points.

The propagation of uncertainty in the calculated gas-generator fuel mass flow rate is presented in Tables C.7 and C.8, while that for the calculated gas-generator air mass flow rate is presented in Tables C.9 and C.10.

The air and fuel mass flow rates through the MGT system were calculated using the general equation for the mass flow rate through a differential pressure

Table C.10: Precision uncertainty in the calculated air mass flow rate

					Parameter precision uncertainty		
Parameter	Nominal value, X_i	s_{X_i}	N_i	$p_{X_i} = \frac{S_{X_i}}{\sqrt{N_i}}$	$\frac{p_{X_i}}{X_i}$ [%]	Sensitivity coefficient, θ_i	$\frac{p_{X_i}}{X_i}\theta_i$
Discharge coefficient, C	...	...	...	...	...	1.00	0.00
Expansion factor, ϵ	...	...	...	...	...	1.00	0.00
Pipe diameter, D [mm]	213.7	...	...	...	...	$\frac{2\beta^4}{1-\beta^4} = \frac{2(0.4)^4}{1-(0.4)^4} = 0.05$	0.00
Throat diameter, d [mm]	77.3	...	...	...	...	$\frac{2}{1-\beta^4} = \frac{2}{1-(0.4)^4} = 2.05$	0.00
Differential pressure, ΔP [Pa]	1265	11	140	0.93	0.074 %	0.50	0.037
Density, $\rho = f(P,T)$ [kg/m^3]	...	...	...	...	0.21 %	0.50	0.11
Total precision uncertainty, $\frac{p_{\dot{m}_a}}{\dot{m}_a}$	...	...	...	...	...	...	0.12 %

class meter (Equation 4.17). The propagation of uncertainty in the calculated mass flow rates was determined using the following expression (ASME PTC 19.5, 2004)

$$\frac{u_{\dot{m}}}{\dot{m}} = \left[\left(\frac{u_C}{C}\right)^2 + \left(\frac{u_\epsilon}{\epsilon}\right)^2 + \left(\frac{2\beta^4}{1-\beta^4}\right)^2\left(\frac{u_D}{D}\right)^2 + \left(\frac{2}{1-\beta^4}\right)^2\left(\frac{u_d}{d}\right)^2 + \left(\frac{u_{\Delta P}}{2\Delta P}\right)^2 + \left(\frac{u_\rho}{2\rho}\right)^2\right]^{1/2} \tag{C.13}$$

where u_X is either bias or precision uncertainty in parameter X, and the square root of the coefficient of each term in Equation C.13 is the sensitivity coefficient θ of that term.

The total uncertainty in the calculated mass flow rates was determined as the root-sum-square of the estimated total bias and precision uncertainty components shown in Tables C.7 to C.10. For a 95 % confidence interval, a total uncertainty of ± 10 % was estimated in the calculated fuel mass flow rate, corresponding to a range of $\dot{m}_f = 0.0043 \pm 0.0004$ kg/s. For the same confidence level, a total uncertainty of ± 4 % was estimated in the calculated air mass flow rate, corresponding to a range of $\dot{m}_a = 0.256 \pm 0.010$ kg/s.

For both calculated mass flow rates, bias error contributed the largest uncertainty. The uncertainty due to bias error can be reduced by using measurement instrumentation with a higher performance rating. Care should also be taken to properly calibrate this instrumentation.

The uncertainty in the measured gas-generator TIT is presented in Table C.11. For a 95 % confidence interval, a total uncertainty of ± 2 % was estimated in the measured gas-generator TIT. This uncertainty corresponded to a gas-generator TIT measurement range of 853 $\pm$ 17 °C. This uncertainty level is higher than the comparable maximum allowable gas turbine exhaust temperature measurement uncertainty of 6 °C, recommended by the ASME PTC 22 Standard. In addition, this estimated uncertainty doesn't account for the measurement error introduced by factors, such as radiation, conduction and stagnation effects.

The uncertainty in the measured gas-generator rotational speed is presented in Table C.12. For a 95 % confidence interval, a total uncertainty of ± 828 rpm (± 1 %) was estimated in the measured gas-generator rotational speed. This uncertainty corresponded to a gas-generator rotational speed measurement range of 73 611 $\pm$ 828 rpm. The estimated uncertainty level is 10

Table C.11: Uncertainty in the measured gas-generator TIT

Parameter	Nominal value, X_i	s_{X_i}	N_i	$p_{X_i} = \frac{S_{X_i}}{\sqrt{N_i}}$	$\frac{p_{X_i}}{X_i}$ [%]	$\frac{b_{X_i}}{X_i}$ [%]	Total uncertainty $\frac{U_{X_i}}{X_i} = 2\left(\frac{u_{X_i}}{X_i}\right)$
Gas-generator TIT, T_3 [°C]	853	48	560	2.03	0.24 %	0.75	2 %

Table C.12: Uncertainty in the measured gas-generator rotational speed

Parameter	Nominal value, X_i	s_{X_i}	N_i	$p_{X_i} = \frac{S_{X_i}}{\sqrt{N_i}}$	b_{X_i}	Total uncertainty $U_{X_i} = 2\,(u_{X_i})$
Gas-generator rotational speed, N [rpm]	73 611	1251	140	106	400	828 rpm

times higher than the maximum allowable rotational speed measurement uncertainty of 0.1 % recommended by the ASME PTC 22 Standard. Bias error contributes the largest uncertainty, and can be reduced by, firstly, increasing the sensitivity of the speed sensors, and then taking care to properly calibrate them against an accurate standard, if possible.

C.4 Sample calculation

This sample calculation illustrates the approach taken in calculating the MGT system performance parameters presented in Tables 4.5 and 4.6. Only the performance parameters corresponding to the experimentally determined optimum equilibrium running point (third row of Table 4.5) were considered. The performance parameters were calculated using averaged test data for the third test point of run 1 (third row of Table C.5).

Assumptions: Steady, one-dimensional flow. Stagnation conditions at both compressor inlets. Negligible inlet and exhaust duct pressure losses. Both air and propane behave as ideal gases. There is complete combustion of propane in dry air, and the combustion products behave as ideal gases.

Fluid properties:

$R = 0.287$ kJ/kgK
$H = 46.34$ MJ/kg

Dimensions:

$d_2 = 49.0$ mm
$d_3 = 77.3$ mm
$d_8 = 98.6$ mm

The MGT system equilibrium running point is characterised by parameters such as the gas-generator compressor non-dimensional mass flow rate and rotational speed and total-to-total pressure ratio and isentropic efficiency. The gas-generator compressor non-dimensional mass flow rate was calculated from

the air mass flow rate through the gas-generator compressor, and the measured ambient absolute pressure and mean static temperature at the inlet of the gas-generator compressor, using

$$\begin{aligned}
&\frac{\dot{m}\sqrt{T_{01}}}{P_{01}} \\
&= \frac{0.256 \times \sqrt{(20 + 273.15)}}{100.2} \\
&= 0.0437
\end{aligned}$$

while the gas-generator compressor non-dimensional rotational speed was calculated from the measured gas-generator compressor rotational speed and inlet ambient static temperature, using

$$\begin{aligned}
&\frac{N}{\sqrt{T_{01}}} \\
&= \frac{73\,611}{\sqrt{20 + 273.15}} \\
&= 4299
\end{aligned}$$

To calculate the gas-generator compressor total-to-total pressure ratio, the stagnation pressure of the compressed air at the outlet of the gas-generator compressor had to first be determined. The stagnation pressure was in turn calculated from the stagnation temperature of the compressed air at the gas-generator compressor outlet. This stagnation temperature was calculated from the mean static temperature of the compressed air at the outlet of the gas-generator compressor, and the corresponding mean ideal-gas specific heat at constant pressure and velocity. Firstly, the velocity of the air stream was calculated using Equation 4.29

$$\begin{aligned}
V_2 &= \frac{4\dot{m}_a R T_2}{P_2 \pi d_2^2} \\
&= \frac{4 \times 0.256 \times 0.287 \times (112 + 273.15)}{208.4 \times \pi \times \left(\frac{49}{1000}\right)^2} \\
&= 72 \text{ m/s}
\end{aligned}$$

then, the corresponding mean ideal-gas specific heat at constant pressure of the air stream was calculated using Equation 3.20

$$\begin{aligned} c_{p,a(T_2)} &= -1.966 \times 10^{-9} T_2^3 + 0.4802 \times 10^{-5} T_2^2 + 0.1967 \times 10^{-2} T_2 + 28.11 \\ &= -1.966 \times 10^{-9} \left(112 + 273.15\right)^3 + 0.4802 \times 10^{-5} \left(112 + 273.15\right)^2 \\ &+ 0.1967 \times 10^{-2} \left(112 + 273.15\right) + 28.11 \\ &= 29.462 \text{ KJ/kmolK} \\ &= 1017 \text{ J/kgK} \end{aligned}$$

and, the stagnation temperature of the air stream at the outlet of the gas-generator compressor was then calculated using Equation 4.28

$$\begin{aligned} T_{02} &= T_2 + \frac{V_2^2}{2c_{p,a(T_2)}} \\ &= (112 + 273.15) + \frac{72^2}{2 \times 1017} \\ &= 387.70 \text{ K} \end{aligned}$$

From the determined stagnation temperature, and the measured static temperature and absolute pressure of the compressed air at the gas-generator compressor outlet, the corresponding stagnation pressure was calculated using Equation 4.27

$$\begin{aligned} P_{02} &= P_2 \left(\frac{T_{02}}{T_2}\right)^{\gamma_a/(\gamma_a - 1)} \\ &= 208.4 \left(\frac{387.70}{112 + 273.15}\right)^{1.4/(1.4-1)} \\ &= 213.3 \text{ kPa} \end{aligned}$$

with γ_a calculated using Equation 3.44, for the known $c_{p,a(T_2)} = 1017$ J/kgK. The gas-generator compressor total-to-total pressure ratio was then calculated from the ratio of the determined stagnation pressure of the compressed air at the outlet of the gas-generator compressor and the measured ambient pressure

$$\begin{aligned} &\frac{P_{02}}{P_{01}} \\ &= \frac{213.3}{100.2} \\ &= 2.1 \end{aligned}$$

The gas-generator compressor total-to-total isentropic efficiency was calculated from the determined gas-generator compressor total-to-total pressure ratio and the stagnation temperature of the air stream at the outlet of the gas-generator compressor, using Equation 3.29

$$\begin{aligned}\eta_{c,t-t} &= \frac{T_{01}}{\Delta T_{012}}\left[\left(\frac{P_{02}}{P_{01}}\right)^{(\gamma_a-1)/\gamma_a} - 1\right] \\ &= \frac{20+273.15}{387.70-(20+273.15)}\left[(2.1)^{(1.4-1)/1.4} - 1\right] \\ &= 73\ \%\end{aligned}$$

For the MGT system performance parameters, the stagnation gas-generator TIT was calculated from the mean static temperature of the combustion gases at the outlet of the combustion chamber, and the corresponding mean ideal-gas specific heat at constant pressure and velocity. The velocity of the combustion gases was calculated using Equation 4.31

$$\begin{aligned}V_3 &= \frac{4\left(\dot{m}_a+\dot{m}_f\right)RT_3}{P_3\pi d_3^2} \\ &= \frac{4\times(0.256+0.0043)\times 0.287\times(853+273.15)}{184.4\times\pi\times\left(\frac{77.3}{1000}\right)^2} \\ &= 97\ \text{m/s}\end{aligned}$$

while the corresponding mean ideal-gas specific heat at constant pressure of the combustion gases was calculated from the mean ideal-gas specific heat at constant pressure of air at the same mean temperature, the fuel/air ratio and the carbon and hydrogen theta functions for mean ideal-gas specific heat at constant pressure. The mean ideal-gas specific heat at constant pressure of air was calculated using Equation 3.20

$$\begin{aligned}c_{p,a(T_3)} &= -1.966\times10^{-9}T_3^3 + 0.4802\times10^{-5}T_3^2 + 0.1967\times10^{-2}T_3 + 28.11 \\ &= -1.966\times10^{-9}\left(853+273.15\right)^3 + 0.4802\times10^{-5}\left(853+273.15\right)^2 \\ &\quad + 0.1967\times10^{-2}\left(853+273.15\right) + 28.11 \\ &= 33.607\ \text{kJ/kmolK} \\ &= 1160\ \text{J/kgK}\end{aligned}$$

The fuel/air ratio was calculated using Equation 3.43

$$\begin{aligned} f &= \frac{\dot{m}_f}{\dot{m}_a} \\ &= \frac{0.0043}{0.256} \\ &= 0.017 \end{aligned}$$

The carbon and hydrogen theta functions were calculated from the mean ideal-gas specific heat at constant pressure of air, carbon dioxide, oxygen and water vapor, which were in turn calculated using third-order polynomial approximations suggested by Cengel and Boles (2011). The mean ideal-gas mean specific heat at constant pressure of carbon dioxide was calculated using

$$\begin{aligned} c_{p,CO_2(T_3)} &= 7.469 \times 10^{-9} T_3^3 - 3.501 \times 10^{-5} T_3^2 + 5.981 \times 10^{-2} T_3 + 22.26 \\ &= 7.469 \times 10^{-9} \left(853 + 273.15\right)^3 - 3.501 \times 10^{-5} \left(853 + 273.15\right)^2 \\ &+ 5.981 \times 10^{-2} \left(853 + 273.15\right) + 22.26 \\ &= 55.882 \text{ kJ/kmolK} \\ &= 1270 \text{ J/kgK} \end{aligned}$$

while the mean ideal-gas specific heat at constant pressure of oxygen was calculated using

$$\begin{aligned} c_{p,O_2(T_3)} &= 1.312 \times 10^{-9} T_3^3 - 0.7155 \times 10^{-5} T_3^2 + 1.520 \times 10^{-2} T_3 + 25.48 \\ &= 1.312 \times 10^{-9} \left(853 + 273.15\right)^3 - 0.7155 \times 10^{-5} \left(853 + 273.15\right)^2 \\ &+ 1.520 \times 10^{-2} \left(853 + 273.15\right) + 25.48 \\ &= 35.397 \text{ kJ/kmolK} \\ &= 1106 \text{ J/kgK} \end{aligned}$$

and the mean ideal-gas specific heat at constant pressure of water vapor was calculated using

$$\begin{aligned} c_{p,H_2O(T_3)} &= -3.595 \times 10^{-9} T_3^3 + 1.055 \times 10^{-5} T_3^2 + 0.1923 \times 10^{-2} T_3 + 32.24 \\ &= -3.595 \times 10^{-9} \left(853 + 273.15\right)^3 + 1.055 \times 10^{-5} \left(853 + 273.15\right)^2 \\ &+ 0.1923 \times 10^{-2} \left(853 + 273.15\right) + 32.24 \\ &= 42.651 \text{ kJ/kmolK} \\ &= 2368 \text{ J/kgK} \end{aligned}$$

The carbon theta function for mean ideal-gas specific heat at constant pressure was calculated using Equation 3.46

$$\begin{aligned}\theta_C &= 3.6645c_{p,CO_2(T_3)} - 2.6645c_{p,O_2(T_3)} - c_{p,a(T_3)} \\ &= 3.6645 \times 1270 - 2.6645 \times 1106 - 1160 \\ &= 547 \text{ J/kgK}\end{aligned}$$

while the hydrogen theta function for mean ideal-gas specific heat at constant pressure was calculated using Equation 3.47

$$\begin{aligned}\theta_H &= 8.9365c_{p,H_2O(T_3)} - 7.9365c_{p,O_2(T_3)} - c_{p,a(T_3)} \\ &= 8.9365 \times 2368 - 7.9365 \times 1106 - 1160 \\ &= 11\,224 \text{ J/kgK}\end{aligned}$$

and the mean ideal-gas specific heat at constant pressure of the combustion gases was then calculated using Equation 3.45

$$\begin{aligned}c_{p,g(T_3)} &= c_{p,a(T_3)} + \frac{f}{1+f}\left(\overline{C}_f\theta_C + \overline{H}_f\theta_H\right) \\ &= 1160 + \frac{0.017}{1+0.017}\left(\frac{36.0321}{44.09562} \times 547 + \frac{8.06352}{44.09562} \times 11\ 224\right) \\ &= 1202 \text{ J/kgK}\end{aligned}$$

From the mean static temperature of the combustion gases at the outlet of the combustion chamber and the corresponding mean ideal-gas specific heat at constant pressure and velocity, the stagnation gas-generator TIT was calculated, using Equation 4.30

$$\begin{aligned}T_{03} &= T_3 + \frac{V_3^2}{2c_{p,g(T_3)}} \\ &= (853 + 273.15) + \frac{97^2}{2 \times 1202} \\ &= 1130.06 \text{ K}(857\,^\circ\text{C})\end{aligned}$$

The useful work output of the power turbine was determined indirectly; as the power absorbed by the low-pressure compressor directly coupled to it. The absorbed power was calculated from the air mass flow rate through the low-pressure compressor, the stagnation temperature at both the inlet and outlet of the low-pressure compressor and the overall mean ideal-gas specific heat at constant pressure of the compressed air passing through the low-pressure compressor. The stagnation temperature at the inlet of the low-pressure compressor was assumed to be equal to the mean ambient temperature measured at

the inlet of the gas-generator compressor. The stagnation temperature at the outlet of the low-pressure compressor was calculated from the corresponding mean static temperature, the mean ideal-gas specific heat at constant pressure and velocity. Firstly, the velocity of the air stream was calculated using Equation 4.34

$$\begin{aligned} V_8 &= \frac{4\dot{m}_a R T_8}{P_8 \pi d_8^2} \\ &= \frac{4 \times 0.473 \times 0.287 \times (32 + 273.15)}{109.4 \times \pi \times \left(\frac{98.6}{1000}\right)^2} \\ &= 50 \text{ m/s} \end{aligned}$$

then, the mean ideal-gas specific heat at constant pressure of the compressed air was calculated using Equation 3.20

$$\begin{aligned} c_{p,a(T_8)} &= -1.966 \times 10^{-9} T_8^3 + 0.4802 \times 10^{-5} T_8^2 + 0.1967 \times 10^{-2} T_8 + 28.11 \\ &= -1.966 \times 10^{-9} (32 + 273.15)^3 + 0.4802 \times 10^{-5} (32 + 273.15)^2 \\ &+ 0.1967 \times 10^{-2} (32 + 273.15) + 28.11 \\ &= 29.102 \text{ kJ/kmolK} \\ &= 1005 \text{ J/kgK} \end{aligned}$$

and, the stagnation temperature of the compressed air at the outlet of the low-pressure compressor was then calculated, using Equation 4.33

$$\begin{aligned} T_{08} &= T_8 + \frac{V_8^2}{2 c_{p,a(T_8)}} \\ &= (32 + 273.15) + \frac{50^2}{2 \times 1005} \\ &= 306.39 \text{ K} \end{aligned}$$

The overall mean ideal-gas specific heat at constant pressure of the compressed air passing through the low-pressure compressor was calculated using Equa-

tion 3.20

$$
\begin{aligned}
c_{p,a\left(\frac{T_{08}+T_{07}}{2}\right)} &= -1.966\times10^{-9}\left(\frac{T_{08}+T_{07}}{2}\right)^3 + 0.4802\times10^{-5}\left(\frac{T_{08}+T_{07}}{2}\right)^2 \\
&\quad + 0.1967\times10^{-2}\left(\frac{T_{08}+T_{07}}{2}\right) + 28.11 \\
&= -1.966\times10^{-9}\left(\frac{306.39+293.15}{2}\right)^3 \\
&\quad + 0.4802\times10^{-5}\left(\frac{306.39+293.15}{2}\right)^2 \\
&\quad + 0.1967\times10^{-2}\left(\frac{306.39+293.15}{2}\right) + 28.11 \\
&= 29.078 \text{ kJ/kmolK} \\
&= 1004 \text{ J/kgK}
\end{aligned}
$$

From the air mass flow rate through the low-pressure compressor, the stagnation temperature at both the inlet and outlet of the low-pressure compressor and the mean ideal-gas specific heat at constant pressure of the compressed air passing through the low-pressure compressor, the power absorbed by the low-pressure compressor was then calculated using Equation 4.32

$$
\begin{aligned}
\dot{W}_{pt} = \dot{W}_c &= \dot{m}_a c_{p,a\left(\frac{T_{08}+T_{07}}{2}\right)}\left(T_{08}-T_{07}\right) \\
&= 0.473\times1004\times(306.39-293.15) \\
&= 6288 \text{ W} \\
&= 6.3 \text{ kW}
\end{aligned}
$$

From the determined useful work output of the power turbine, the MGT system specific fuel consumption was calculated using Equation 3.59

$$
\begin{aligned}
SFC &= \frac{3600\dot{m}_f}{\dot{W}_{pt}} \\
&= \frac{3600\times0.0043}{6288} \\
&= 0.0025 \text{ kg/kWh}
\end{aligned}
$$

The cycle thermal efficiency was calculated from the determined power turbine useful work output and the total cycle thermal energy input. The total cycle thermal energy input was calculated from the effective calorific value of propane at the determined stagnation gas-generator TIT, which was

in turn calculated from the carbon and hydrogen theta functions for effective calorific value. The carbon theta function for effective calorific value at the determined stagnation gas-generator TIT was calculated using Equation 3.53

$$\begin{aligned}\theta_C &= 3.6645\overline{h}_{CO_2(T_{03})} - 2.6645\overline{h}_{O_2(T_{03})} - \overline{h}_{a(T_{03})} \\ &= 3.6645 \times 1\,134\,511 - 2.6645 \times 1\,123\,851 - 1\,196\,000 \\ &= -33\,085 \text{ J/kg}\end{aligned}$$

while the hydrogen theta function for effective calorific value at the determined stagnation gas-generator TIT was calculated using Equation 3.54

$$\begin{aligned}\theta_H &= 8.9365\overline{h}_{H_2O(T_{03})} - 7.9365\overline{h}_{O_2(T_{03})} - \overline{h}_{a(T_{03})} \\ &= 8.9365 \times 2\,295\,535 - 7.9365 \times 1\,123\,851 - 1\,196\,000 \\ &= 10\,398\,605 \text{ J/kg}\end{aligned}$$

with the enthalpy values for air, carbon dioxide, oxygen and water vapor interpolated from ideal-gas property tables provided by Cengel and Boles (2011). The effective calorific value of propane at the determined stagnation gas-generator TIT was calculated using Equation 3.51

$$\begin{aligned}E.C.V_T &= H - \left[\overline{h}_a\right]_{298.15\text{ K}}^{T_{03}} - \overline{C}_f\theta_C - \overline{H}_f\theta_H \\ &= 46\,340\,000 - [1\,196\,000 - 298\,180] - \frac{36.0321}{44.09562} \times -33\,085 \\ &\quad - \frac{8.06352}{44.09562} \times 10\,398\,605 \\ &= 43\,567\,680 \text{ J/kg}\end{aligned}$$

The total cycle thermal energy input for the MGT under standard operation was calculated from the determined effective calorific value of propane at the determined stagnation gas-generator TIT and the measured fuel mass flow rate, using Equation 3.55

$$\begin{aligned}\dot{Q}_{th} &= \dot{m}_f E.C.V_T \\ &= 0.0043 \times 43\,567\,680 \\ &= 187\,341 \text{ W} \\ &= 187.3 \text{ kW}\end{aligned}$$

Finally, the cycle thermal efficiency was calculated using Equation 3.60

$$\begin{aligned}\eta_{th} &= \frac{\dot{W}_{pt}}{\dot{Q}_{th}} \\ &= \frac{6.3}{187.3} \\ &= 3.4\ \%\end{aligned}$$

Analysis:

The results obtained from the sample calculation closely match those calculated and tabulated in the third row of Table 4.5. The minor discrepancies observed are due to round-off error.

List of References

Aichmayer, L., Spelling, J., Laumert, B. and Fransson, T. (2013). Micro Gas-Turbine Design for Small-Scale Hybrid Solar Power Plants. *Journal of Engineering for Gas Turbines and Power*, vol. 135, no. 11, p. 113001. ISSN 0742-4795.

Allen, K.G. (2014). *Rock Bed Thermal Storage for Concentrating Solar Power Plants*. Ph.D. thesis, Stellenbosch University.

AORA Solar (2015). Product.
Available at: `http://aora-solar.com/`

ASME PTC 10 (1997). Performance Test Code on Compressors and Exhausters.

ASME PTC 19.1 (2006). Test Uncertainty.

ASME PTC 19.2 (1987). Pressure Measurement. Instruments and Apparatus.

ASME PTC 19.3 (2004). Temperature Measurement. Instruments and Apparatus.

ASME PTC 19.5 (2004). Flow Measurement.

ASME PTC 22 (2014). Gas Turbines.

Augusto, F. (2018). Personal communication. Capstone Turbine Corporation.

Balje, O. (1981). *Turbomachines: A Guide to Design, Selection and Theory*. John Wiley & Sons Inc., New York.

Beckwith, T., Marangoni, R. and Lienhard V, J. (1993). *Mechanical Measurements*. 5th edn. Addison-Wesley. ISBN 0-201-56947-7.

Bergman, T.L., Lavine, A.S., Incropera, F.P. and Dewitt, D.P. (2011). *Fundamentals of Heat and Mass Transfer*. 7th edn. John Wiley & Sons, Inc. ISBN 978-0470-50197-9.

BorgWarner (2017). Performance Turbochargers - Catalog.

Boyce, M.P. (2012). *Gas Turbine Engineering Handbook*. 4th edn. Butterworth-Heinemann, Oxford. ISBN 0884157326.

Brun, K. and Nored, M.G. (2009). Guideline for Field Testing of Gas Turbine and Centrifugal Compressor Performance. Tech. Rep. August, Gas Machinery Research Council.

Buck, R., Giuliano, S. and Uhlig, R. (2016). Central Tower Systems using the Brayton Cycle. In: Blanco, M. and Santigosa, L.R. (eds.), *Advances in Concentrating Solar Thermal Research and Technology*, 1st edn, chap. 16, pp. 353–382. Woodhead Publishing. ISBN 9780081005170.

Cengel, Y.A. and Boles, M.A. (2011). *Thermodynamics: An Engineering Approach*. 7th edn. McGraw-Hill. ISBN 978-007-131111-3.

Cengel, Y.A. and Cimbala, J.M. (2010). *Fluid Mechanics: Fundamentals and Applications*. 2nd edn. McGraw-Hill, Singapore. ISBN 978-007-128421-9.

City University of London (2018). OMSOP Report Summary. Tech. Rep., European Union.

Conrado, A.C., Lacava, P.T., Filho, A.C.P. and Sanches, M.d.S. (2004). Basic Design Principles for Gas Turbine Combustor. In: *Proceedings of the 10th Brazillian Congress of Thermal Sciences and Engineering*.

Coogan, S., Brun, K. and Teraji, D. (2013). Micromix combustor for high temperature hybrid gas turbine concentrated solar power systems. *Energy Procedia*, vol. 49, pp. 1298–1307. ISSN 18766102.

Córdova, J.L., Walton II, J.F. and Heshmat, H. (2015). High Effectiveness, Low Pressure Drop Recuperator for High Speed and Power Oil-Free Turbogenerator. In: *Proceedings of ASME Turbo Expo 2015: Turbine Technical Conference and Exposition GT2015*, pp. 1–10. Montréal, Canada.

Dixon, S.L. and Hall, C.A. (2010). *Fluid Mechanics and Thermodynamics of Turbomachinery*. Sixth edn. Butterworth-Heinemann. ISBN 9781856177931.

Endress+Hauser (2014). Technical information Deltabar S PMD75, FMD77, FMD78.

Endress+Hauser (2016). Technical information Deltabar M PMD55.

European Commission (2005). SOLGATE (Solar hybrid gas turbine electric power system) Project report. Tech. Rep..

European Commission (2011). SOLHYCO (Solar-Hybrid Power and Cogeneration Plants) Final Public Report. Tech. Rep..

Felsmann, C., Gampe, U. and Freimark, M. (2015). Dynamic behavior of a solar hybrid gas turbine system. *Asme*, vol. 3, p. 9.

Felsmann, C., Gampe, U., Heide, S. and Freimark, M. (2014). Modeling and Simulation of the Dynamic Operating Behavior of a High Solar Share Gas Turbine System. *Journal of Engineering for Gas Turbines and Power*, vol. 137, no. 3, p. 031601. ISSN 0742-4795.

Festo (2007). Flow sensor type SFE1-LF.

Fielding, D. and Topps, J.E.C. (1959). Thermodynamic Data for the Calculation of Gas Turbine Performance. Tech. Rep., Aeronautical Research Council.

Fisher, U., Sugarmen, C., Ring, A. and Sinai, J. (2004). Gas Turbine "Solarization" - Modifications for Solar/Fuel Hybrid Operation. *Journal of Solar Energy Engineering*, vol. 126, no. 3, p. 872. ISSN 01996231.

Fluid Meters (1959). *Their Theory and Application*. 5th edn. ASME.

Freeman, B.C. (1965). *Discharge Coefficients of Combustion Chamber Dilution Holes*. Masters thesis, Cranfield University.

Gallup, D.R. and Kesseli, J.B. (1994). A Solarized Brayton Engine Based on Turbo-Charger Technology and the DLR Receiver. *29th Intersociety Energy Conversion Engineering Conference, Pts 1-4*, pp. 1719–1724. ISSN 0146955X.

Gauché, P., Brent, A.C. and von Backström, T.W. (2014). Concentrating solar power: Improving electricity cost and security of supply, and other economic benefits. *Development Southern Africa*, vol. 31, no. 5, pp. 692–710. ISSN 0376-835X.

Gauché, P., Pfenninger, S., Meyer, A.J., von Backström, T.W. and Brent, A.C. (2012). Modeling Dispatchability Potential of CSP in South Africa. In: *Southern African Solar Energy Conference (SASEC)*, vol. 1, pp. 1–11.

GeoModel Solar (2017). SolarGIS DNI Solar Map.
Available at: `http://solargis.com/assets/graphic/free-map/DNI/Solargis-Africa-and-Middle-East-DNI-solar-resource-map-en.png`

Grobbelaar, S., Gauché, P. and Brent, A. (2014). Developing a competitive concentrating solar power industry in South Africa: Current gaps and recommended next steps. *Development Southern Africa*, vol. 31, no. 3, pp. 475–493. ISSN 0376-835X.

Helio100 (2017). Helio100.
Available at: `http://helio100.sun.ac.za/`

Heller, L. (2017). *Development of a Dual-Pressure Air Receiver System for the SUNDISC Cycle*. Ph.D. thesis, Stellenbosch University.

Heller, L., Allen, K.G., Lubkoll, M., Pitot de la Beaujardiere, J.-f.P. and Gauché, P. (2017). The SUNDISC cycle : A direct storage-charging dual-pressure air receiver cycle. vol. 153, pp. 435–444.

Heller, P., Pfänder, M., Denk, T., Tellez, F., Valverde, A., Fernandez, J. and Ring, A. (2006). Test and evaluation of a solar powered gas turbine system. *Solar Energy*, vol. 80, no. 10, pp. 1225–1230. ISSN 0038092X.

Heuer, T. (2016). Personal communication. BorgWarner Turbo Systems Engineering GmbH.

Homann, C. (2015). *Effects of the Solar Hybridization on the Performance of a Gas Turbine*. Masters thesis, Stellenbosch University.

Hummel, S. (2014). *Berechnung und Konstruktion einer Brennkammer für eine Mikrogasturbine*. Final year project, University of Stuttgart.

IEA (2010). Technology Roadmap: Concentrating Solar Power. Tech. Rep., International Energy Agency.

IRENA (2012). Renewable Energy Technologies: Cost Analysis Series. Tech. Rep. Power Sector Issue 2/5 Concentrating Solar Power, International Renewable Energy Agency.

IRENA (2013*a*). Renewable Power Generation Costs in 2012 : An Overview. Tech. Rep., International Renewable Energy Agency.

IRENA (2013*b*). Southern African Power Pool: Planning and Prospects for Renewable Energy. Tech. Rep., International Renewable Energy Agency.

ISO 2314 (2009). Gas Turbines - Acceptance Tests.

Kaddah, K.S. (1964). *Discharge Coefficients and Jet Deflection Angles for Combustor Liner Air Entry Holes*. Masters thesis, Cranfield University.

Kathirgamanathan, D. and Axelsson, L.-u. (2018). Rotor Over-Speed Analysis of a Hybrid Solar Gas Turbine. In: *Proceedings of ASME Turbo Expo 2018 Turbomachinery Technical Conference and Exposition*, pp. 1–11.

Kesseli, J.B. and Wells, A. (1989). Cost competitive 30 kw gas turbine/generator demonstration for cogeneration or solar-electric applications. pp. 1903–1908.

Knight, H.A. and Walker, R.B. (1957). The Component Pressure Losses in Combustion Chambers. Tech. Rep., Aeronautical Research Council.

Kolb, G.J., Ho, C.K., Mancini, T.R. and Gary, J.A. (2011). Power Tower Technology Roadmap and cost reduction plan. Tech. Rep. April, Sandia National Laboratories, Albuquerque, New Mexico.

Korzynietz, R., Brioso, J.A., Del Río, A., Quero, M., Gallas, M., Uhlig, R., Ebert, M., Buck, R. and Teraji, D. (2016). Solugas - Comprehensive analysis of the solar hybrid Brayton plant. *Solar Energy*, vol. 135. ISSN 0038092X.

Korzynietz, R., Quero, M. and Uhlig, R. (2012). SOLUGAS - Future Solar Hybrid Technology. *SolarPACES Conference*.

Kotze, J.P. (2014). *Thermal Energy Storage in Metallic Phase Change Materials*. Ph.D. thesis, Stellenbosch University.

Kröger, D.G. (2012). SUNSPOT. The Stellenbosch University Solar Power Thermodynamic Cycle. Tech. Rep., Stellenbosch University, Stellenbosch.

Landman, W.A. (2017). *Optical Performance of the Reflective Surface Profile of a Heliostat*. Ph.D. thesis, Stellenbosch University.

le Roux, W.G., Bello-Ochende, T. and Meyer, J.P. (2011*a*). Operating conditions of an open and direct solar thermal Brayton cycle with optimised cavity receiver and recuperator. *Energy*, vol. 36, no. 10, pp. 6027–6036. ISSN 03605442.

le Roux, W.G., Bello-Ochende, T. and Meyer, J.P. (2011*b*). Thermodynamic optimisation of the integrated design of a small-scale solar thermal Brayton cycle. *International journal of energy research*, vol. 36, pp. 135–147. ISSN 0363907X.

le Roux, W.G., Bello-Ochende, T. and Meyer, J.P. (2012). Optimum performance of the small-scale open and direct solar thermal Brayton cycle at various environmental conditions and constraints. *Energy*, vol. 46, no. 1, pp. 42–50. ISSN 03605442.

le Roux, W.G. and Meyer, J.P. (2016). Modeling the small-scale dish-mounted solar thermal Brayton cycle. *AIP Conference Proceedings*, vol. 1734. ISSN 15517616.

Lefebvre, A. and Ballal, D. (2010). *Gas Turbine Combustion - Alternative Fuels and Emissions*. 3rd edn. CRC Press. ISBN 9781420086058.

Lilley, D.G. (1977). Swirl Flows in Combustion: A Review. *AIAA Journal*, vol. 15, no. 8, pp. 1063–1078. ISSN 0001-1452.

Louw, F.G. (2015). *Investigation of the Flow Field in the Vicinity of an Axial Flow Fan During Low Flow Rates*. Ph.D. thesis, Stellenbosch University.

Lubkoll, M. (2017). *Performance Characteristics of the Spiky Central Receiver Air Pre-heater (SCRAP)*. Ph.D. thesis, Stellenbosch University.

Luiten, R.V. (2015). *Performance Improvement of the Rover 1S/60 Gas Turbine Compressor*. Masters thesis, Stellenbosch University.

Macsteel VRN (2009). Stainless Steel and Aluminium Catalogue.

Marsh, D.A. (2019). *Conversion of a Kerosene-Fuelled Gas Turbine to Run on Propane*. Masters thesis, Stellenbosch University.

Mellor, A.M. (1990). *Design of Modern Turbine Combustors*. ACADEMIC PRESS, San Diego, Califonia. ISBN 0-12-490055-0.

Merven, B., Hughes, A. and Davis, S. (2010). An analysis of energy consumption for a selection of countries in the Southern African Development Community. *Journal of Energy in Southern Africa*, vol. 21, no. 1, pp. 11–24. ISSN 1021447X.

Micro-Epsilon (2014). Instruction Manual turboSPEED DZ140.

Murthy, J.N. (1988). *Gas Turbine Combustor Modelling for Design*. Ph.D. thesis, Cranfield Institute of Technology.

National Instruments (2008). USER GUIDE AND SPECIFICATIONS NI cDAQ-9172.

Nieuwoudt, A. (1987). *Turboaanjaertoetsbank*. Final year project, Stellenbosch University.

NREL (2017). Concentrating Solar Power Projects.

Owen, M.T.F. (2013). *Air-cooled Condenser Steam Flow Distribution and Related Dephlegmator Design Considerations*. Ph.D. thesis, Stellenbosch University.

Quero, M., Korzynietz, R., Ebert, M., Jiménez, A.A., Del Río, A. and Brioso, J.A. (2013). Solugas - Operation experience of the first solar hybrid gas turbine system at MW scale. *Energy Procedia*, vol. 49, pp. 1820–1830. ISSN 18766102.

Ring, A., Sugarmen, C., Sinai, J., Buck, R., Schwarzbözl, P., Heller, P., Denk, T., Fernandez-Reche, J. and Tellez-Sufrategui, F.M. (2004). Solar Powered Gas Turbine Prototype - Technology Development and Test Results. In: *PowerGen Europe*, pp. 1–20. Barcelona.

Roberts, P.B. (1979). Application of the Centaur Industrial Gas Turbine to the Central Receiver Concept for Solar Electric Power. In: *Proceedings of the ASME 1979 International Gas Turbine Conference and Exhibit and Solar Energy Conference*, pp. 1–8. San Diego, Califonia.

Rover Gas Turbines Limited (1967). Maintenance Manual. Engines Type 1S/60 and 1S/90.

SADC (2010). Southern African Development Community SADC Regional Energy Access Strategy and Action Plan. , no. March.

Saravanamuttoo, H.I.H., Rogers, G.F.C., Cohen, H. and Straznicky, P.V. (2009). *Gas Turbine Theory*. sixth edn. Pearson Education Limited, Essex, England. ISBN 978-0-13-222437-6.

Schommarz, T.M. (2019). *Analysis , Design and Manufacture of a Solarised Gas Turbine Compressor*. Masters thesis, Stellenbosch University.

Sinai, J., Sugarmen, C. and Fisher, U. (2005). Adaptation and Modification of Gas Turbines for Solar Energy Applications. In: *Proceedings of GT2005 ASME Turbo Expo 2005: Power for Land, Sea and Air June 6-9, 2005, Reno-Tahoe, Nevada, USA*, pp. 1–8. Nevada, USA. ISBN 9728943377.

Sonbesie Weather Station (2017). Download Weather Data.
Available at: `http://weather.sun.ac.za/downloadList.php`

Spelling, J., Laumert, B. and Fransson, T. (2012). Optimal Gas-Turbine Design for Hybrid Solar Power Plant Operation. *Journal of Engineering for Gas Turbines and Power*, vol. 134, no. 9, p. 092301. ISSN 07424795.

Ssebabi, B., Dinter, F. and van der Spuy, J. (2016). Modeling a Solar-Hybrid Micro Gas Turbine. In: *4th Southern African Solar Energy Conference*. Stellenbosch.

Ssebabi, B., Dinter, F., van der Spuy, J. and Schatz, M. (2019). Predicting the performance of a micro gas turbine under solar-hybrid operation. *Energy*, vol. 177, pp. 121–135. ISSN 03605442.

Stine, W.B. and Geyer, M. (2001). *Power from the sun*. ISBN 0036-8075. Available at: `http://www.powerfromthesun.net/book.htm`

Struwig, D.J. (2013). *The Development and verification of a Centrifugal Compressor Test Bench*. Masters thesis, Stellenbosch University.

Veer, T., Haglerod, K.K. and Bolland, O. (2004). Measured Data Correction for Improved Fouling and Degradation Analysis of Offshore Gas Turbines. In: *ASME/GTI TURBOEXPO Conference 2004*, pp. 1–8. Vienna, Austria.

Visser, W.P.J., Shakariyants, S.a., de Later, M., Haj Ayed, A. and Kusterer, K. (2012). Performance optimisation of a 3 kW microturbine for CHP applications. In: *Proceedings of ASME Turbo Expo 2012*, pp. 1–10. Copenhagen, Denmark.

Visser, W.P.J., Shakariyants, S.a. and Oostveen, M. (2011). Development of a 3 kW Microturbine for CHP Applications. *Journal of Engineering for Gas Turbines and Power*, vol. 133, no. 4, p. 042301. ISSN 07424795.

Walsh, P.P. and Fletcher, P. (2004). *Gas Turbine Performance*. 2nd edn. Blackwell Publishing company. ISBN 0471360937.

Whitfield, A. and Baines, N. (1990). *Design of Radial Turbomachines*. 1st edn. Longman Scientific & Technical, Essex CM20 2JE, England. ISBN 0-582-49501-6.

Zhang, Y. (2016). *Pre-Study for conversion of a gas turbine from liquid to gaseous fuel*. Masters thesis, Stellenbosch University.